Master's thesis

NTNU
Norwegian University of Science and Technology
Faculty of Information Technology and Electrical Engineering
Department of Engineering Cybernetics

Ernst Torsgård

Modeling, analysis and control of wireless inductive power transfer system with constant voltage load designed for large variations in the magnetic coupling conditions

Master's thesis in Cybernetics and Robotics
Supervisor: Jon Are Wold Suul
July 2019

NTNU
Norwegian University of
Science and Technology

Ernst Torsgård

Modeling, analysis and control of wireless inductive power transfer system with constant voltage load designed for large variations in the magnetic coupling conditions

Master's thesis in Cybernetics and Robotics
Supervisor: Jon Are Wold Suul
July 2019

Norwegian University of Science and Technology
Faculty of Information Technology and Electrical Engineering
Department of Engineering Cybernetics

NTNU
Norwegian University of
Science and Technology

Abstract

The concept of inductive power transfer (IPT) has become an essential technology in numerous applications, varying from low-power transcutaneous charging of biomedical implants to high-power wireless charging of electric vehicles (EVs). In recent years, the emerging interest for EVs has resulted in significant progress in the field of wireless battery charging for high-power application.

This work will present a nonlinear state-space representation of a series-series (SS) compensated IPT-system with constant voltage load (CVL). This model is expressed by direct-quadrature (dq)-axis variables in a synchronous reference frame (SRF) and is linearizable at any feasible steady-state operating point, allowing for small-signal analysis for assessing stability and sensitivity properties in a variety of operating conditions. The small-signal investigation has been performed considering resonant as well as off-resonant operation, thus revealing how the system dynamics and stability properties change during the whole expected range of varying operating conditions. From this analysis, markedly slower dynamics is observed in the case with low magnetic coupling compared to high.

A simulation framework for the IPT-circuit, the nonlinear state-space model and the small-signal state-space model has been developed in the MATLAB/Simulink/Simscape environment, enabling for model verification by time-domain simulation. It is seen that the presented state-space models accurately represent the amplitudes and phase angles of the first harmonic voltages and currents of the IPT-system in numerous operating conditions. The simulations have also shown that the current waveforms get increasingly distorted as the coupling factor and off-resonant conditions increases, making the fundamental frequency approximation less accurate and thus causing some slight deviation. In addition, it is seen that the state-space models are relatively sensitive to changes in the operating frequency.

Reduced-order modeling is investigated and a lower-order model is developed and validated by time-domain simulations, which confirms that the obtained model preserves important dynamics of the system. Furthermore, small-signal analysis has been utilized to develop control loops based solely on sending side power feedback. Subsequently, frequency responses are examined to support the design of a simple PI-controller ensuring robust closed-loop response over the whole expected operating range. The resulting closed-loop performance shows that the controller response coincides with the results obtained in the steady-state analysis.

Sammendrag

Konseptet *induktiv kraftoverføring* har blitt en verdifull teknologi i mange applikasjoner, alt fra fra laveffekts transkutan ladning av biomedisinske implantater til høyeffekts trådløs lading av elektriske fremkomstmidler. I de senere år har den fremvoksende interessen for elektriske kjøretøy resultert i betydelige framskritt innen trådløs batteriladning for høyeffektsapplikasjoner.

I denne oppgaven presenteres en ulineær tilstandsrommodell av et serie-serie-kompensert induktivt kraftoverføringssystem med konstant lastspenning. Denne modellen er uttrykt med direkte-kvadratur-aksevariabler i en synkron referanseramme og er lineariserbar ved alle mulige praktiske driftspunkt, noe som muliggjør småsignalanalyse for å kunne vurdere stabilitet- og sensitivitetsegenskaper ved en rekke ulike driftsforhold. Denne småsignalanalysen har blitt utført både med tanke på drift i resonans så vel som utenfor resonans, og har avslørt hvordan dynamikken og stabilitetsegenskapene i systemet endrer seg gjennom hele det forventede driftsområdet. Fra denne analysen observeres markant tregere dynamikk i tilfellet med lav magnetisk kobling sammenlignet med høy.

Et simuleringsrammeverk for kretsen, den ulineære tilstandsrommodellen og småsignaltilstandsrommodellen er implementert i MATLAB/Simulink/Simscape, noe som legger til rette for modellverifisering ved tidssimuleringer. Det ses at de presenterte tilstandsrommodellene nøyaktig representerer amplituden og fasevinkelen av de førsteharmoniske strømmene og spenningene i det induktive kraftoverføringssystemet i flerfoldige driftspunkt. Simuleringene har også vist at bølgeformen på strømmene blir stadig mer forvrengt ettersom koblingsfaktoren øker og driftsfrekvensen beveger seg lenger fort fra resonans, noe som gjør grunnfrekvensentilnærmingen mindre nøyaktig og dermed forårsaker noen små avvik. I tillegg ses det at tilstandsrommodellene er relativt sensitive for endringer i driftsfrekvensen.

Redusert orden-modellering er undersøkt, og en lavere ordens modell er blitt utviklet og deretter validert ved tidssimuleringer, noe som bekrefter at den bevarer viktig systemdynamikk. Videre har småsignalanalyse blitt brukt til å utarbeide reguleringssløyfer basert på tilbakekobling fra sendesiden. Deretter er frekvensresponser undersøkt for å kunne designe en enkel PI-regulator for å garantere robust lukket-sløyfe-respons over hele det forventede driftsområdet. Lukket-sløyfe-ytelsen viser at regulatorresponsen sammenfaller med resultatene oppnådd i den stasjonære analysen.

Preface

This thesis was written during the spring semester of 2019 and concluded my 5-year integrated Master of Science degree at the Norwegian University of Science and Technology, Department of Engineering Cybernetics.

The work in this dissertation is mainly accomplished with numerical computing and simulation environments such as Maple and MATLAB/Simulink/Simscape, and I have independently developed and implemented all Maple and MATLAB code as well as all Simulink diagrams.

The general nonlinear state-space model used in this thesis was developed by G. Guidi and J. A. Suul in ”Modelling techniques for designing high-performance on-road dynamic charging systems for electric vehicles”. In this article, the nonlinear model was linearized assuming a system tuned for a single resonance frequency. Herein I have generalized and adapted the small-signal state-space model to any feasible operating conditions. Furthermore, the procedure outlined in Chapter 3 is based on work done in ”Minimizing converter requirements of inductive power transfer systems with constant voltage load and variable coupling conditions”, also written by G. Guidi and J. A. Suul. However, I have derived the state-space models and the steady-state expressions utilized throughout this thesis on my own.

In my specialization project carried out during the Autumn semester of 2018, which this treatise is a continuation of, stability and controllability properties of the small-signal state-space model intended solely for resonant operation was studied. Some of the introductory text, background theory and results presented in the project are included here, as I believe this material is essential for the reader to perceive. However, they only coincide to a minor extent, as they are modified, generalized and expanded in this work.

A paper based on some of the results achieved in this thesis was submitted to the 20th IEEE Workshop on Control and Modeling of Power Electronics, IEEE COMPEL 2019, held in Toronto, Canada from June 17th to June 20th, 2019. This workshop brought together researchers, engineers, and students from academia and industry all over the world for interactive discussions on the latest advances in modeling, analysis, and control of power electronic systems. I attended this conference and presented the paper, which is titled ”Small-Signal State Space Analysis of Inductive Battery Charging System in Off-Resonant Operation.” The paper is attached in Appendix E.

Acknowledgement

My preliminary knowledge about wireless power transfer systems and related topics and modeling approaches in the field of power electronics were limited. My first encounter with inductive power transfer technology was with my specialization project carried out during the Autumn semester of 2018. I would, therefore, like to thank my supervisor at SINTEF, Jon A. W. Suul, for allowing me to work on this topic and for accurately evaluating my level and introducing new and advanced concepts at an appropriate pace. Furthermore, thanks for all guidance, literature advice, and discussions during my last year at NTNU. Thanks are also due to my co-supervisor at SINTEF, Giuseppe Guidi, for his assistance when I experienced some numerical issues with mathematical software. Their contributions have been of vital importance, and without them, this work certainly would not have been possible for me to accomplish.

Ernst Torsgård
8.7.2019
Trondheim

Table of Contents

List of Tables

List of Figures

List of Abbreviations

dq direct-quadrature. 45–47, 49–51, 53, 58, 61, 83, 114, 129, 137

CRL constant resistive load. 5, 12, 26, 27, 30, 37, 38, 43, 45, 58, 60, 61, 71–73, 80, 87–89, 111, 136, 137

CVL constant voltage load. 4, 5, 10, 12, 26–30, 32, 37, 38, 43, 45, 50, 58, 60, 61, 71, 72, 80, 87, 88, 111, 129, 136, 137, 145

EV electrical vehicle. 1–3, 9, 10

IPT inductive power transfer. 1–5, 7–10, 12, 25–27, 32, 34, 36, 37, 43, 45, 47, 53, 61, 63, 65, 66, 72, 80, 121, 129, 130, 139, 145

KVL Kirchoff's voltage law. 11, 13, 46

SRF synchronous reference frame. 45, 48, 129

SS series-series. 4, 5, 10, 43, 45, 61, 129

Nomenclature

$\boldsymbol{A}$	State matrix
$\boldsymbol{B}$	Input matrix
$\boldsymbol{C}$	Output matrix
$\boldsymbol{D}$	Feedthrough matrix
$\boldsymbol{l}_k^i$	Left eigenvector
$\boldsymbol{r}_k^i$	Right eigenvector
$\boldsymbol{u}^p$	Operating input vector
$\boldsymbol{W}_c$	Controllability Gramian
$\boldsymbol{W}_o$	Observability Gramian
$\boldsymbol{x}^p$	Steady-state vector
$\hat{I}_1$	Sending side current phasor
$\hat{I}_2$	Receiving side current phasor
$\hat{V}_1$	Sending side voltage phasor
$\hat{V}_2$	Receiving side voltage phasor
ω	Operating frequency
ω_0	Nominal operating frequency
$\vec{i}_1$	Stationary frame sending current

$\vec{i}_2$	Stationary frame receiving side current
$\vec{v}_1$	Stationary frame sending side voltage
$\vec{v}_2$	Stationary frame receiving side voltage
$\vec{v}_{C1}$	Stationary frame sending side capacitor voltage
$\vec{v}_{C2}$	Stationary frame receiving side capacitor voltage
C_1	Sending side capacitance
C_2	Receiving side capacitance
I_1	Sending side current amplitude
i_1	Time-periodic sending side current
I_2	Receiving side current amplitude
i_2	Time-periodic receiving side current
$i_{1,d,0}$	Steady-state sending side d-axis current
$i_{1,dq}$	Sending side dq-axis current
$i_{1,d}$	Sending side d-axis current
$i_{1,q,0}$	Steady-state sending side q-axis current
$i_{1,q}$	Sending side q-axis current
$i_{2,d,0}$	Steady-state receiving side d-axis current
$i_{2,dq}$	Receiving side dq-axis current
$i_{2,d}$	Receiving side d-axis current
$i_{2,q,0}$	Steady-state receiving side q-axis current
$i_{2,q}$	Receiving side q-axis current
k	Coupling factor
K_p	Controller gain
k_{nom}	Nominal coupling factor
L_1	Sending side self-inductance
L_2	Receiving side self-inductance
$L_{\alpha 1}$	Sending side leakage inductance

$L_{\alpha 2}$	Receiving side leakage inductance
M	Mutual inductance
P_{ideal}	Lossless output power
P_{in}	Input power
p_{ki}	Participation factor
P_{out}	Output power
Q_1	Sending side quality factor
Q_2	Receiving side quality factor
R_1	Sending side resistance
R_2	Receiving side q-axis current component
$s_{i,k}$	Parametric sensitivity
T_f	Filter time constant
T_i	Controller integral time
V_1	Sending side voltage amplitude
v_1	Time-periodic sending side voltage
V_2	Receiving side voltage amplitude
v_2	Time-periodic receiving side voltage
$V_{1,0}$	Sending side steady-state voltage amplitude
$v_{1,d,0}$	Sending side d-axis operating voltage
$v_{1,dq}$	Sending side dq-axis voltage
$V_{1,nom}$	Sending side nominal voltage amplitude
$v_{1,q,0,}$	Sending side q-axis operating voltage
$V_{2,0}$	Receiving side steady-state voltage amplitude
$v_{2,dq}$	Receiving side dq-axis voltage
$V_{2,nom}$	Receiving side nominal voltage amplitude
$v_{C1,d,0}$	Steady-state sending side d-axis capacitor voltage
$v_{C1,dq}$	Sending side dq-axis capacitor voltage

$v_{C1,d}$	Sending side d-axis capacitor voltage
$v_{C1,q,0}$	Steady-state sending side q-axis capacitor voltage
$v_{C1,q}$	Sending side q-axis capacitor voltage
$v_{C2,d,0}$	Steady-state receiving side d-axis capacitor voltage
$v_{C2,dq}$	Receiving side dq-axis capacitor voltage
$v_{C2,d}$	Receiving side d-axis capacitor voltage
$v_{C2,q,0}$	Steady-state receiving side q-axis capacitor voltage
$v_{C2,q}$	Receiving side q-axis capacitor voltage
$V_{dc,out,0}$	Operating load voltage
$V_{dc,out}$	Load voltage
x_c	Detuning factor
x_u	Unbalance factor
Z_{send}	Equivalent sending side impedance

Chapter 1

Introduction and Motivation

The concept of inductive power transfer (IPT) has been subject to significant enhancement in recent years. IPT is a technology which transfers electrical energy from a power source to an electrical device without any wires or other kinds of conductors as a physical link and is being increasingly utilized in a variety of applications, such as consumer electronics, industrial automation, charging of electrical vehicles (EVs) and in the field of medicine. Considerable progress is currently being made regarding dynamic IPT, which is a promising idea that could offer significant benefits regarding electric mobility in the years to come[1][2].

EVs are becoming more popular for every day that passes, and the interest for electric mobility is not likely to fall anytime soon. Some obvious reasons for this are technological advances such as the development of electrical energy storage systems with high energy and power densities, which reduces limitations in aspects surrounding driving range per recharge, and the fact that EVs are getting more high-technological and advanced[3]. The gap between EVs and fossil-fueled cars in terms of driving comfort and safety is decreasing, and the rising media attention for climate changes and global warming makes people more environmentally conscious. Electricity-based transportation has an environmental advantage on cars with engines fueled by gasoline or diesel, which contributes significantly to greenhouse gasses. Especially since there is much ongoing work in the field of renewable energy sources. Moreover, advancements in technology reduce the production costs of EVs, and they are therefore more accessible to the general public[1][2]. As well as being economical to drive due to electricity being less expensive than fossil-fuel, several governments propose incentives such as exemption from road taxes, reduced yearly fees and free public charging stations[4], thus making EVs more attractive. Today's EVs are on the same level as vehicles with internal combustion engines in almost all aspects, such as, e.g., driving comfort and acceleration. They are even more efficient, more accurate, and have faster torque response[3]. Another advantage of EVs is their low noise output, both in idle as well as in motion. However, this emission-free transportation method has some limitations that need to be addressed. The need for an expensive and large energy storage system onboard the vehicle in order to increase the mileage range per recharge is one of those drawbacks.

IPT is a battery charging concept that could significantly reduce barriers, such as limited driving range. This technology could mitigate the need for large energy storage systems onboard, which would make the EVs lighter and even more efficient. To transfer wireless power from a charging system integrated into the road surface to a receiver mounted underneath the EV, thus charging the onboard batteries without any physical contact, considerably simplifies the charging process and reduces safety issues, such as handling of the charging equipment[3]. The overall recharging process gets, in addition, more comfortable and more convenient due to its automated capabilities. IPT-technology could make it possible to transfer power and to charge EVs even while they are in motion. Likewise, for marine applications, transferring wireless power from a dock-mounted inductive coupler to a marine vessel could provide many of the same advantages[5]. Also, IPT is clean and unaffected by dirt and other external influences like chemicals and weather, making the charging process more robust and tolerant in rough environments[1]. However, there are still numerous improvements required in order to reduce and eliminate challenges that prevent this technology from a large and worldwide application.

1.1 Historical background

The idea of wireless power transfer as a possible alternative of the standard transmission line-based power distribution started in the late 19th century with J. C. Maxwell and H. R. Hertz. Maxwell proposed in ”Treatise on Electricity and Magnetism,” published in 1873, that there indeed exist possibilities of transferring power from one point to another in the free space by electromagnetic waves. Hertz later validated Maxwell's proposition through his experiments performed between the period of 1885-1889. N. Tesla undertook the job of developing wireless power transfer further between 1899 and 1910 and did several experiments using resonant inductive coupling, i.e., where the receiving side inductor-capacitor circuit is tuned to resonance with the sending side inductor-capacitor circuit. This resonant transformer is more familiar known as the renowned ”Tesla coil.” Despite Tesla's efforts to commercialize wireless power transfer, he ran out of funding and the research on wireless power transfer went dry. However, all these attempts of making wireless power transfer systems led to significant breakthroughs in communication systems[6]. Although Tesla may arguably be the most famous name in the field of wireless power transfer, the concept of dynamic-powered EVs came first from M. Hutin and M. Leblanc in 1894 with their patent on transformer systems for electric railways[7].

More recently, a helicopter flight powered by microwaves was experimented at the Spencer Laboratory of the Raytheon Company in 1964 and was internationally broadcasted. Resonant wireless power transfer was also successfully experimented in biomedical applications in the 1960s[8]. Inductive roadway power was proposed by D. V. Otto and J. G. Bolger in the 70s. In 1972, Otto proposed a vehicle that was powered inductively at 10 kHz by a force commutated sinusoidal silicon controlled rectifier inverter. It was not until the late 1970s that IPT-powered EVs began to fetch academic interest when Bolger and others began to publish papers on electric highway-systems. Through the 1980s, a project organized by The Partner for Advanced Transit and Highways in California made an IPT-powered vehicle with 60% efficiency when operating under variable coupling conditions. In 1986, Kelly and Owens proposed an aircraft entertainment system wirelessly powered by the use of wires hidden underneath the carpet. A power supply generating current at 38 kHz was used to energize the wires, and pickup coils under the seats coupled 8 watts for each passenger. In 1991, Boys and Green at the University of Auckland developed an IPT-system which was suitable for materials handling systems. This development was the first IPT-system where the individual components could be identified and improved separately, making it a foundation for much of the work done regarding wireless power transfer over the past couple of decades[1].

Due to rapid technological advances and development in the last decades, wireless power transfer has become an essential technology in a variety of applications, offering significant benefits in modern automation systems. Remarkable development concerning static IPT with short air gap and stable coupling conditions have been made, and now the main focus has been aimed at dynamic IPT. Here, there are still many challenges to overcome, as system conditions such as magnetic coupling and load may change notably during operation, thus requiring the need for more robust systems tolerant to misalignment and parameter variation.

1.2 Problem description

The main objective of this thesis is to derive, analyze, implement and validate a nonlinear and small-signal state-space model representing the envelope of the first harmonic currents and voltages of an IPT-system with constant voltage load (CVL) in a wide range of operating conditions. This analysis should form the basis for the design of a suitable power control scheme, preferably without depending on communication across the air gap between the sending and receiving side of the IPT-system.

1.3 Contributions

The main contributions of this work can be compactly summarized as follows:

- The development of a method to linearize the nonlinear state-space model, representing the envelope of the fundamental frequency currents and voltages of a series-series (SS)-compensated IPT-system with CVL, in any feasible operating point.
- Model verification of the resulting generalized small-signal state-space model and the nonlinear state-space model by numerous time-domain simulations in the MATLAB/Simulink/Simscape environment.
- All stability analysis, such as eigenvalues trajectories, performed in off-resonant conditions, as well as all analysis regarding parametric sensitivities, participation factors, and Gramians, both in resonant and off-resonant operation.
- Investigation of frequency responses in order to obtain a reduced-order model, effectively removing six states without altering the most dominating dynamics of the system, as revealed by time-domain simulations.
- The design of control loops based only on sending side power feedback by using small-signal input-output frequency characteristics, thus eliminating the need for communication across the air gap of the IPT-system. The resulting PI-controller is implemented in the MATLAB/Simulink/Simscape environment and the closed-loop performance is evaluated by several time-domain simulations.
- The design, implementation and time-domain simulations of a gain-scheduled controller, which adapts to the highly nonlinear operating range, thus providing fast and damped response over the whole expected range of operation.

1.4 Outline

The remaining of this thesis is structured as follows:

- ***Chapter 2 – Theory*** gives an introduction to IPT-technology and on what challenges this technology faces, as well as a brief presentation on modeling and analysis methods and background theory.
- ***Chapter 3 – Nonlinear and Small-Signal Model*** describes the derivation and linearization procedure of a nonlinear state-space model representing the dynamics of an SS-compensated IPT-system with CVL. It also presents a small-signal state-space model assuming constant resistive load (CRL).
- ***Chapter 4 – Frequency Characteristics*** explains the procedure for deriving important general circuit expressions. Furthermore, it provides design techniques utilized to obtain and shape the frequency characteristics in order to establish a system suitable for power control by regulating the operating frequency.
- ***Chapter 5 – Model Verification*** presents numerous time-domain simulation to confirm the validity of the presented state-space models in several different realistic operating conditions.
- ***Chapter 6 – Sensitivity and Stability Analysis*** provides comprehensive small-signal stability and sensitivity analysis in order to assess the dynamic behavior of the system under variable load and coupling conditions. Moreover, control properties such as controllability and observability are studied with a variety of input-output configurations and operating conditions.
- ***Chapter 7 – Frequency Domain Analysis and Power Control*** gives insight into model order reduction techniques and provides a reduced-order model validated through time-domain simulations. Subsequently, small-signal frequency responses are utilized to design control loops with a simple PI-controller for providing the necessary operating frequency in order to maintain constant output power under variable coupling conditions.
- ***Chapter 8 – Closing Remarks*** issues concluding remarks and suggestions for future work.

Chapter 2

Theory

This chapter provides some basic theory of IPT-systems as well as describing some crucial concepts and mathematical tools used throughout this work. Some of the material provided here is also presented in the specialization project.

2.1 Basic principles of inductive power transfer systems

A block scheme of a simplified IPT-model is shown in Figure 2.1. It consists of a high-frequency DC/AC switching converter on the transmitting side, two magnetically coupled coils – the transmitter and receiver – and an AC/DC rectifier on the receiving side. Several types of topologies are possible, depending on e.g., control strategy, application, desired level of complexity, and cost.

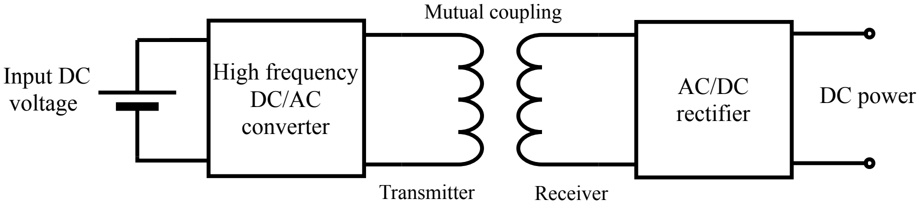

Figure 2.1: Simpel model of an IPT-system.

The main idea of an IPT-system is the same as for the more familiar transformers and can be summarized as follows: An input voltage is converted to high-frequency ac-voltage which excites the transmitting side and generates an alternating current. Then, by Ampere's circuital law, the alternating current through the coil generates a magnetic field, which oscillates with the same frequency as the power source. IPT-systems usually operate in the kHz – GHz range, depending on application. By Faraday's law of induction, an alternating electromotive force is then induced in the receiving coil which in turn generates an alternating current. The alternating current at the receiving side is converted into a dc-signal required for charging the given device. This procedure may happen when the receiving coil is within the required range of the transmitting coil for the given application [9][10].

2.1.1 Magnetically coupled circuit

As mentioned, the main idea of an IPT-system is based on a magnetic field linking the coupled circuits – the sending and the receiving side. In literature, the sending side circuit of the IPT-system is also sometimes called primary or transmitter circuit, whereas the receiving side circuit is sometimes called secondary or pickup circuit. The circuit in Figure 2.2 represents two magnetically coupled coils. The mutual inductance is labeled M and the self-inductance's of the coils are labeled L_1 and L_2.

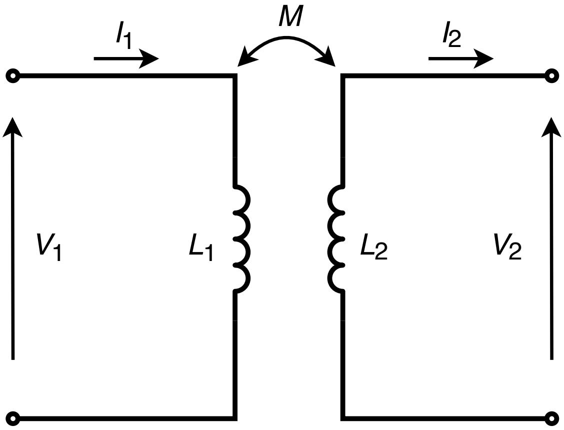

Figure 2.2: Mutually coupled coils.

The voltage induced in the receiving side circuit can be related to the current flowing in the sending side circuit by the mutual inductance M. A current is present only if the output terminals are connected to a load. Even if this is conceptually the same idea as for transformers, due to the absence of a solid magnetic core between the primary and secondary side, the magnetic coupling is in general significantly weaker for IPT-systems.

The magnetic coupling coefficient is related to the mutual inductance through:

$$k = \frac{M}{\sqrt{L_1 L_2}}, \qquad 0 \leq k \leq 1 \tag{2.1}$$

The coupling factor k is a dimensionless parameter describing the strength of the mutual coupling between the coils. The higher the separation between the coils, the lower magnetic coupling, and vice verse. Moreover, lateral and longitudinal displacement and the relative orientation of the coils also cause variation in the magnetic coupling. Variation in the coupling conditions is a common issue in the field of IPT.

Depending on their application, IPT-systems can be subdivided into two main groups: dynamic and static IPT. Dynamic IPT refers to in-motion charging of EVs, whereas static IPT refers to stationary charging of EVs. The main challenges that arise in static wireless charging also arise in dynamic wireless charging. However, the latter is subject to some more difficulties, and a summary of the challenges in both cases are presented below.

A considerable challenge in design for dynamic power transfer is the large, and possibly varying, air gap between the sending coil and receiver coil, as well as the almost inevitable misalignment. In IPT-systems for roadway-powered EVs, the air gap between the roadside transmitter and the vehicle side receiver is quite high compared to more static systems using the same functionality, especially such as transformers. This considerable air gap significantly lowers the magnetic coupling and efficiency. Moreover, the track system in the ground has to be covered with a layer of bitumen or some other kind of material used in road construction, making an already large air gap even more substantial. Additionally, a ship docked at the harbor is exposed to waves and tide and will therefore drift and move relative to a transmitter mounted on the dock. Subsequently, the loading or unloading of ship cargo will affect the displacement and buoyancy of the vessel – and, therefore, the air draft[5]. This results in more movement of the ship relative to the dock-mounted transmitter. Due to this, the weak magnetic coupling becomes a problem for IPT-systems. The main focus in the designing of IPT-systems is, therefore, to enhance the tolerance to misalignment and the resulting variation of the magnetic coupling by improving the magnetic design and control of power[1]. As explained above, an IPT-system has several parameters which could vary during in-motion dynamic charging, such as the coupling factor. In order to deal with such parameter variation, good controllability is needed[11]. The use of larger coils can also attenuate the variation in the magnetic coupling conditions, however, this increases expenses and counteracts the realization of compact systems, which could limit the scope of IPT-applications.

2.1.2 Compansation topologies

Wireless charging of marine vessels and land-based EVs entails a significant and varying air gap between the sending and pickup coil due to, e.g., waves, tide, unevenness in the road structure and the need for adequate clearance between the road surface and the EV. Also, a marine vessel or an electric vehicle in motion will almost always cause some misalignment. These constraints weaken the mutual coupling and cause a high leakage inductance, which leads to reduced efficiency. It is, therefore, crucial to choose a suitable compensation scheme when designing an IPT-system. Conditions such as maximum efficiency and output power independent of both load and coupling coefficient need to be considered[12]. To cope with these challenges requires the introduction of capacitive compensation in both sending- and pickup coil[13], which enhances the power transfer capability and reduces the voltage and current ratings of the sending side converter[14].

The different topologies can be very complicated, but four basic compensation schemes are usually studied, namely series-series, series-parallel, parallel-series, parallel-parallel. Out of these, the most used compensation schemes are series-series and series-parallel. The different topologies offer separate advantages and downsides, and one needs to carefully choose, depending on the application, the appropriate compensation scheme. The compensation topology considered in this report is the SS-compensation, that is, both primary and secondary coils are series compensated. With this topology, the compensation capacitance's are independent of both the magnetic coupling and the load, making the design more convenient. Besides, this topology can act as a constant current source, which is desirable when charging a battery. Moreover, the resonant frequency of this structure is only subject to minor variations due to varying load and magnetic coupling conditions under operation[15], which is a significant advantage. It is also very effective when there is no misalignment[16][17].

2.1.3 Series-series compensated inductive power transfer system

The IPT-system studied in this thesis is displayed in Figure 2.3[18]. As can be seen, the topology is an SS-compensated IPT-system with an H-bridge converter on the sending side and a diode rectifier on the receiving side, connected directly to a CVL representing a battery. The sending side coil is energized by the output voltage v_1 of the H-bridge converter, and the diode bridge rectifies the ac signals v_2 and i_2 in the receiving coil.

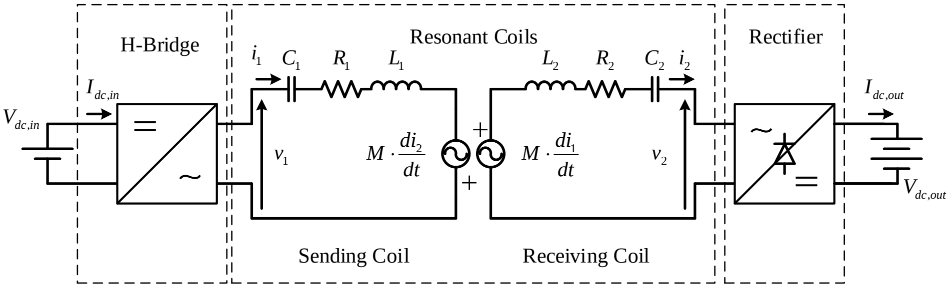

Figure 2.3: SS-compensated IPT-system with CVL.

The sending and receiving side's resonance frequencies are defined, respectively, according to:

$$\omega_{0,1} = \frac{1}{\sqrt{C_1 L_1}}, \quad \omega_{0,2} = \frac{1}{\sqrt{C_2 L_2}} \tag{2.2}$$

In order for the system to operate in resonance, the compensation capacitances are tuned so that these two expressions are equal. When the excitation frequency of the voltage source exciting the sending coil equals this frequency, the system is said to be operating in resonance.

Assuming that all currents and voltages in the system are sinusoidal waveforms, a first harmonic approximation can be deduced, which is a modeling technique where only the fundamental frequency components of the voltages and currents in the system are assumed to contribute to the power transfer. This modeling technique provides decent accuracy as long as the voltage and current waveforms are close to sinusoidal.

With the use of Kirchoff's voltage law (KVL) and applying the first harmonic approximation, the differential equations describing the dynamics of the circuit can be found in the time-domain as:

$$v_1(t) = R_1 i_1(t) + L_1 \frac{di_1(t)}{dt} - M \frac{di_2(t)}{dt} + v_{C1}(t) \tag{2.3a}$$

$$v_2(t) = -R_2 i_2(t) - L_2 \frac{di_2(t)}{dt} + M \frac{di_1(t)}{dt} - v_{C2}(t) \tag{2.3b}$$

$$\frac{dv_{C_1}(t)}{dt} = \frac{1}{C_1} i_1(t) \tag{2.3c}$$

$$\frac{dv_{C_2}(t)}{dt} = \frac{1}{C_2} i_2(t) \tag{2.3d}$$

The time-dependency notation is omitted for ease of use in the remaining of this thesis.

2.1.4 Constant voltage load

CVL resulting from battery charging is characteristic where the output voltage of the system on the load resistance is modeled as constant, regardless of the value of the load. Hence, the receiving side voltage v_2 in Figure 2.3 will remain constant despite changes in the receiving side current due to variable operating conditions. Studies have shown that the dynamics of IPT-systems modeled with a CRL are not accurately capturing the dynamic behavior CVL-conditions impose on the system[15][18]. Thus, CVL load modeling approach will be the main focus of this work.

The action of the diode rectifier in Figure 2.3 implies that the phase of the receiving side voltage v_2 must be equal to the phase of the receiving side current i_2. Furthermore, the amplitude of the receiving side voltage will also be dependent on the load voltage $V_{dc,out}$. Therefore, the CVL-characteristics resulting from battery charging can be modeled by:

$$v_2 = \frac{i_2}{I_2} \cdot \frac{4}{\pi} \cdot V_{dc,out} \tag{2.4}$$

where I_2 is the amplitude of the receiving side current i_2. Thus, the fraction $\frac{i_2}{I_2}$ determines the phase and the term $\frac{4}{\pi} V_{dc,out}$ determines the amplitude of the voltage at the receiving side. The scaling factor $\frac{4}{\pi}$ is a result of Fourier analysis as the fundamental component of a square wave has a peak amplitude of $\frac{4}{\pi}$ times the dc-voltage. This equation is an important relationship since the diode rectifier together with the constant voltage source inflicts nonlinear behavior on the system[18].

2.1.5 Constant resistive load

Load modeling with a CRL instead of a CVL results in a fundamentally different dynamic behavior of the system, as this modeling approach does not impose any nonlinearity. Under this assumption, the relationship between the receiving side voltage and current is:

$$v_2 = R_{eq} \cdot i_2 \tag{2.5}$$

R_{eq} is the equivalent load resistance. Here, the receiving side voltage will change in response to changes in the receiving side current due to variation in the operating conditions, in contrast to the case with CVL.

2.1.6 Bifurcation

The H-bridge converter in Figure 2.3 may operate with constant or variable operating frequency, depending on e.g., the application, desired control strategy, and commutation requirements. When the phase angle of the impedance seen by the converter crosses zero during operation, i.e., switches from inductive to capacitive, or vice verse, the behavior of the converter changes accordingly. This phenomenon is called bifurcation, playing an essential role regarding converter switching losses. A slightly inductive operation of the sending side converter is advantageous, as this ensures soft-switching[19][20]. It is, therefore, essential to assess the impedance phase characteristics of the system under the intended operation.

2.2 Modeling and analysis methods

2.2.1 Phasor modeling

By representing the currents and voltages as complex phasor variables, an equivalent harmonic circuit as in Figure 2.4 can be derived.

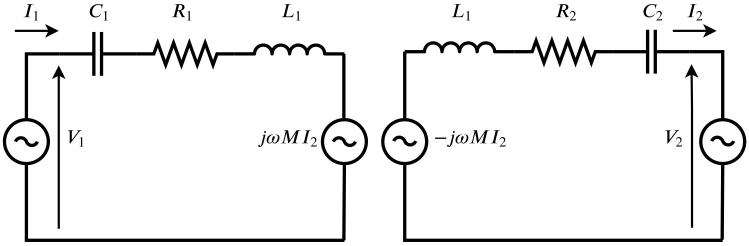

Figure 2.4: Harmonic equivalent circuit with CVL.

Again by utilizing KVL, the relationship between the voltages and currents in the frequency domain can be found to be:

$$\hat{V}_1 = R_1\hat{I}_1 + j\omega L_1\hat{I}_1 - j\omega M\hat{I}_2 + \hat{V}_{C1} \tag{2.6a}$$

$$\hat{V}_2 = -R_1\hat{I}_2 - j\omega L_1\hat{I}_2 + j\omega M\hat{I}_1 - \hat{V}_{C2} \tag{2.6b}$$

$$\hat{V}_{C1} = \frac{1}{j\omega C_1}\hat{I}_1 \tag{2.6c}$$

$$\hat{V}_{C2} = \frac{1}{j\omega C_2}\hat{I}_2 \tag{2.6d}$$

With this approach, sinusoidal currents and voltages can be represented as complex vectors which is advantageous for stationary analysis.

2.2.2 General state-space representation

Writing a dynamical system in a state-space form is a systematic and convenient way of representing higher-order systems. It is a common approach for representing time-varying, time-invariant, nonlinear as well as linear systems and can be utilized in a majority of different domains, such as e.g., mechanical, electrical, biological, and economic.

The dynamics of a nonlinear system represented in a state-space formulation are described by:

$$\begin{aligned} \dot{\boldsymbol{x}}(t) &= \boldsymbol{f}(\boldsymbol{x}(t), \boldsymbol{u}(t)) \\ \boldsymbol{y}(t) &= \boldsymbol{g}(\boldsymbol{x}(t), \boldsymbol{u}(t)) \end{aligned} \tag{2.7}$$

where $\boldsymbol{x}(t) \in \mathbb{R}^n$ are the states, $\boldsymbol{u}(t) \in \mathbb{R}^m$ are the control inputs and $\boldsymbol{y}(t) \in \mathbb{R}^q$ are the outputs of the model. The vectors $\boldsymbol{f} \in \mathbb{R}^n$ and $\boldsymbol{g} \in \mathbb{R}^q$ contains the functions describing the nonlinear model.

The dynamics of a linear and time-invariant system represented in state-space formulation are given by:

$$\begin{aligned} \dot{\boldsymbol{x}}(t) &= \boldsymbol{A}\boldsymbol{x}(t) + \boldsymbol{B}\boldsymbol{u}(t) \\ \boldsymbol{y}(t) &= \boldsymbol{C}\boldsymbol{x}(t) + \boldsymbol{D}\boldsymbol{u}(t) \end{aligned} \tag{2.8}$$

where, as above, $\boldsymbol{x}(t) \in \mathbb{R}^n$ are the states, $\boldsymbol{u}(t) \in \mathbb{R}^m$ are the control inputs and $\boldsymbol{y}(t) \in \mathbb{R}^q$ are the outputs. The state matrix $\boldsymbol{A} \in \mathbb{R}^{n\times n}$, input matrix $\boldsymbol{B} \in \mathbb{R}^{n\times m}$, output matrix $\boldsymbol{C} \in \mathbb{R}^{q\times n}$ and the feedthrough matrix $\boldsymbol{D} \in \mathbb{R}^{q\times m}$ are constant matrices, meaning that they do not change with time.

2.2.3 Linearization and equilibrium points

Linearization of nonlinear models is desired because linear models are significantly easier to analyze than nonlinear models. Mathematical tools such as e.g., Laplace transformation and stability analysis by investigating eigenvalues and eigenvectors as well as many control design methods are based on linear models. A system is linear if the two functions $\boldsymbol{f}$ and $\boldsymbol{g}$ in Equation 2.7 are linear in the variables $\boldsymbol{x}$ and $\boldsymbol{u}$.

The linearization procedure of a nonlinear model can be described as follows. Given the nonlinear state-space model in Equation 2.7. The *i*-th differential equation can be written as:

$$\frac{dx_i}{dt} = f_i(x_1,\, \dots,\, x_n,\, u_1,\, \dots,\, u_m) \tag{2.9}$$

The linearization procedure is based upon Taylor series. When linearizing a dynamical system, the Taylor series expansion is terminated after the first order term. It is assumed that the nonlinear system is continuous and has continuous first order derivatives. By linearizing around an operating point defined by p, that is $(x_1^p,\, \dots,\, x_n^p,\, u_1^p,\, \dots,\, u_m^p)$, with a small perturbation Δx_i and Δu_i away from the operating point, Equation 2.9 can be rewritten:

$$\frac{d}{dt}(x_i^p + \Delta x_i) = f_i(x_i^p + \Delta x_1,\, \dots,\, x_n^p + \Delta x_n,\, u_1^p + \Delta u_1,\, \dots,\, u_m^p + \Delta u_m) \tag{2.10}$$

Taylor-expansion and assuming small enough variation in Δx_i and Δu_i such that all higher-order terms of the Taylor-expansion can be neglected, results in:

$$\begin{aligned} &\dot{x}_i^p + \Delta \dot{x}_i \approx f_i(x_i^p,\, \dots,\, x_n^p,\, u_1^p,\, \dots,\, u_m^p) + \\ &\left.\frac{\partial f_i}{\partial x_1}\right|_p \Delta x_1 + \,\dots\, + \left.\frac{\partial f_i}{\partial x_n}\right|_p \Delta x_n + \left.\frac{\partial f_i}{\partial u_1}\right|_p \Delta u_1 + \,\dots + \left.\frac{\partial f_i}{\partial u_n}\right|_p \Delta u_m \end{aligned} \tag{2.11}$$

where p denotes the operating point ($x = x^p$, $u = u^p$). Equation 2.9 in the operating point can be written:

$$\dot{x}_i^p = f_i(x_i^p,\ \ldots,\ x_n^p,\ u_1^p,\ \ldots,\ u_m^p) \tag{2.12}$$

By substituting this result in Equation 2.11, the term cancels out, and a model for small perturbations around the operating point arises:

$$\Delta\dot{x}_i = \left.\frac{\partial f_i}{\partial x_1}\right|_p \Delta x_1 + \ \ldots\ + \left.\frac{\partial f_i}{\partial x_n}\right|_p \Delta x_n + \left.\frac{\partial f_i}{\partial u_1}\right|_p \Delta u_1 + \ \ldots + \left.\frac{\partial f_i}{\partial u_m}\right|_p \Delta u_m \tag{2.13}$$

which can be written in more compact form by collecting all the linearized differential equations in one single linear vector equation:

$$\Delta\dot{\boldsymbol{x}} = \boldsymbol{A}(\boldsymbol{x}^p, \boldsymbol{u}^p) \cdot \Delta\boldsymbol{x} + \boldsymbol{B}(\boldsymbol{x}^p, \boldsymbol{u}^p) \cdot \Delta\boldsymbol{u} \tag{2.14}$$

where the matrices $\boldsymbol{A}(\boldsymbol{x}^p, \boldsymbol{u}^p)$ and $\boldsymbol{B}(\boldsymbol{x}^p, \boldsymbol{u}^p)$ are given by:

$$\boldsymbol{A}(\boldsymbol{x}^p, \boldsymbol{u}^p) = \left.\begin{pmatrix} \frac{\partial f_1}{\partial x_1} & \frac{\partial f_1}{\partial x_2} & \cdots & \frac{\partial f_1}{\partial x_n} \\ \frac{\partial f_2}{\partial x_1} & \frac{\partial f_2}{\partial x_2} & \cdots & \frac{\partial f_2}{\partial x_n} \\ \vdots & \vdots & \ddots & \vdots \\ \frac{\partial f_n}{\partial x_1} & \frac{\partial f_n}{\partial x_2} & \cdots & \frac{\partial f_n}{\partial x_n} \end{pmatrix}\right|_{\boldsymbol{x^p},\boldsymbol{u^p}} \in \mathbb{R}^{n\times n} \tag{2.15}$$

$$\boldsymbol{B}(\boldsymbol{x}^p, \boldsymbol{u}^p) = \left.\begin{pmatrix} \frac{\partial f_1}{\partial u_1} & \frac{\partial f_1}{\partial u_2} & \cdots & \frac{\partial f_1}{\partial u_m} \\ \frac{\partial f_2}{\partial u_1} & \frac{\partial f_2}{\partial u_2} & \cdots & \frac{\partial f_2}{\partial u_m} \\ \vdots & \vdots & \ddots & \vdots \\ \frac{\partial f_n}{\partial u_1} & \frac{\partial f_n}{\partial u_2} & \cdots & \frac{\partial f_n}{\partial u_m} \end{pmatrix}\right|_{\boldsymbol{x^p},\boldsymbol{u^p}} \in \mathbb{R}^{n\times m} \tag{2.16}$$

or more compactly:

$$\boldsymbol{A}(\boldsymbol{x}^p, \boldsymbol{u}^p) = \left.\frac{\partial f_i}{\partial \boldsymbol{x}}\right|_{\boldsymbol{x}^p,\boldsymbol{u}^p} \qquad \boldsymbol{B}(\boldsymbol{x}^p, \boldsymbol{u}^p) = \left.\frac{\partial f_i}{\partial \boldsymbol{u}}\right|_{\boldsymbol{x}^p,\boldsymbol{u}^p} \tag{2.17}$$

Similar procedure for the nonlinear output equation in 2.7, i.e. Taylor-expansion and neglecting higher-order terms, ultimately results in:

$$\Delta \boldsymbol{y} = \boldsymbol{C}(\boldsymbol{x}^p, \boldsymbol{u}^p) \cdot \Delta \boldsymbol{x} + \boldsymbol{D}(\boldsymbol{x}^p, \boldsymbol{u}^p) \cdot \Delta \boldsymbol{u} \tag{2.18}$$

with matrices:

$$\boldsymbol{C}(\boldsymbol{x}^p, \boldsymbol{u}^p) = \left. \begin{pmatrix} \frac{\partial g_1}{\partial x_1} & \frac{\partial g_1}{\partial x_2} & \cdots & \frac{\partial g_1}{\partial x_n} \\ \frac{\partial g_2}{\partial x_1} & \frac{\partial g_2}{\partial x_2} & \cdots & \frac{\partial g_2}{\partial x_n} \\ \vdots & \vdots & \ddots & \vdots \\ \frac{\partial g_q}{\partial x_1} & \frac{\partial g_q}{\partial x_2} & \cdots & \frac{\partial g_q}{\partial x_n} \end{pmatrix} \right|_{\boldsymbol{x^p}, \boldsymbol{u^p}} \in \mathbb{R}^{q \times n} \tag{2.19}$$

$$\boldsymbol{D}(\boldsymbol{x}^p, \boldsymbol{u}^p) = \left. \begin{pmatrix} \frac{\partial g_1}{\partial u_1} & \frac{\partial g_1}{\partial u_2} & \cdots & \frac{\partial g_1}{\partial u_m} \\ \frac{\partial g_2}{\partial u_1} & \frac{\partial g_2}{\partial u_2} & \cdots & \frac{\partial g_2}{\partial u_m} \\ \vdots & \vdots & \ddots & \vdots \\ \frac{\partial g_q}{\partial u_1} & \frac{\partial g_q}{\partial u_2} & \cdots & \frac{\partial g_q}{\partial u_m} \end{pmatrix} \right|_{\boldsymbol{x^p}, \boldsymbol{u^p}} \in \mathbb{R}^{q \times m} \tag{2.20}$$

or more compactly:

$$\boldsymbol{C}(\boldsymbol{x}^p, \boldsymbol{u}^p) = \left. \frac{\partial g_i}{\partial \boldsymbol{x}} \right|_{\boldsymbol{x}^p, \boldsymbol{u}^p} \qquad \boldsymbol{D}(\boldsymbol{x}^p, \boldsymbol{u}^p) = \left. \frac{\partial g_i}{\partial \boldsymbol{u}} \right|_{\boldsymbol{x}^p, \boldsymbol{u}^p} \tag{2.21}$$

The linearized model is expressed in terms of deviation variables, indicated by the Δ-notation. This notation is typically suppressed for ease of use. It is, however, vital to be aware of that, as the linearization point needs to be considered when converting from deviation variables to real variables.

Equilibrium points

Consider again the differential equations describing the nonlinear dynamics in Equation 2.7. The operating point $(\boldsymbol{x}^p, \boldsymbol{u}^p)$ in the linearization procedure explained above is usually an equilibrium point. A point $\boldsymbol{x}^p \in \mathbb{R}^n$ is called an equilibrium point if the input $\boldsymbol{u}^p \in \mathbb{R}^m$ is of such kind so that:

$$\dot{\boldsymbol{x}}(t) = \boldsymbol{f}(\boldsymbol{x}^p, \boldsymbol{u}^p) = 0, \quad \forall t \tag{2.22}$$

Linearizing around the equilibrium point is necessary in order to assess the system's stability properties, and a linearized model around the equilibrium point is very effective for analyzing the dynamic behavior of the system. Thus, the studied model must have a defined equilibrium point for a given input, and in order to assess the stability properties, all states of the system must settle to a constant value in steady-state. From Equation 2.22 it can be seen that all state variables have a zero derivative in the equilibrium point.

General methods for assessing important properties such as e.g., stability and sensitivity analysis of a dynamic system are not applicable if any of the state-variables are time-periodic in steady-state. Therefore, traditional stability analysis cannot be applied to investigate electrical systems where the state variables are sinusoidal voltages and currents. Thus, approaches such as phasor modeling or modeling in a synchronously rotating dq-reference frame may be utilized[21].

2.2.4 Eigenvectors and eigenvalues

Consider the linear state-space representation in Equation 2.8. The eigenvalues of the square $n \times n$ state matrix $\boldsymbol{A}$, which coincides with the poles of the overall system, are the n roots λ_i, $i = 1, \ldots, n$ of the characteristic polynomial:

$$det(\boldsymbol{A} - \lambda \boldsymbol{I}) = 0 \tag{2.23}$$

This equation is a monic polynomial of degree n, i.e., there will be equally many eigenvalues as there are states in the system. The eigenvalues are either single real poles or complex conjugate poles, that is, $\lambda_i = a + jb$.

Knowledge of the rightmost and least damped eigenvalues of a dynamical system is crucial in the small-signal analysis of power systems. In short:

- If all eigenvalues are located in the open left-hand plane, i.e. all eigenvalues have negative real parts, the system is asymptotically stable: $\Re\{\lambda_i(A)\} < 0, \forall i$.
- If there exists at least one eigenvalue which is located in the open right-hand plane, the system is unstable: $\forall i, \exists \lambda_i : \Re\{\lambda_i(A)\} > 0$.
- If there exists at least one eigenvalue which is is located at the imaginary axis, i.e. have zero real part, and all others are located in the left-hand plane, the system is marginally stable and it is not possible to asses the small-signal stability of the linearized system: $\forall i, \exists \lambda_i : \Re\{\lambda_i(A)\} = 0$.

The right eigenvector $\boldsymbol{r}_i$ corresponding to the eigenvalue λ_i is the column vector satisfying the following equation:

$$(\boldsymbol{A} - \lambda_i \boldsymbol{I})\boldsymbol{r}_i = 0 \Leftrightarrow \boldsymbol{A}\boldsymbol{r}_i = \lambda_i \boldsymbol{r}_i \tag{2.24}$$

The left eigenvector $\boldsymbol{l}_i$ corresponding to the eigenvalue λ_i is the column vector satisfying the following equation:

$$\boldsymbol{l}_i^H(\boldsymbol{A} - \lambda_i \boldsymbol{I}) = 0 \Leftrightarrow \boldsymbol{l}_i^H \boldsymbol{A} = \lambda_i \boldsymbol{l}_i^H \tag{2.25}$$

In this equation, the H-superscript denotes the conjugate transpose. All eigenvectors corresponding to distinct eigenvalues are always linearly independent. For distinct eigenvalues, the left and right eigenvectors are mutually orthogonal and are usually scaled such that they, in addition, are mutually orthonormal:

$$\boldsymbol{l}_i^H \boldsymbol{r}_j = \begin{cases} 1 \text{ if } i = j \\ 0 \text{ if } i \neq j \end{cases} \tag{2.26}$$

Collecting the right eigenvectors as columns in a matrix $\boldsymbol{R}$, the left eigenvectors as rows in a matrix $\boldsymbol{L}$ and the eigenvalues as diagonal elements in a matrix $\boldsymbol{\Lambda}$ results in:

$$\boldsymbol{R} = \begin{bmatrix} \boldsymbol{r}_1 & \boldsymbol{r}_2 & \dots & \boldsymbol{r}_n \end{bmatrix} \tag{2.27}$$

$$\boldsymbol{L} = \begin{bmatrix} \boldsymbol{l}_1 & \boldsymbol{l}_2 & \dots & \boldsymbol{l}_n \end{bmatrix}^H \tag{2.28}$$

$$\boldsymbol{\Lambda} = \begin{bmatrix} \lambda_1 & 0 & \dots & 0 \\ 0 & \lambda_2 & \dots & 0 \\ \vdots & \vdots & \ddots & \vdots \\ 0 & 0 & \dots & \lambda_n \end{bmatrix} \tag{2.29}$$

From this, assuming linearly independent eigenvectors, the following identities may be defined:

$$\boldsymbol{A}\boldsymbol{R} = \boldsymbol{R}\boldsymbol{\Lambda} \Rightarrow \boldsymbol{R}^{-1}\boldsymbol{A}\boldsymbol{R} = \boldsymbol{\Lambda} \tag{2.30a}$$

$$\boldsymbol{L}\boldsymbol{R} = \boldsymbol{I} \Rightarrow \boldsymbol{L}\boldsymbol{A}\boldsymbol{R} = \boldsymbol{\Lambda} \tag{2.30b}$$

By considering the linear state-space representation in Equation 2.8 and defining a new state vector $\boldsymbol{z}(t) = \boldsymbol{T}^{-1}\boldsymbol{x}(t)$, i.e., $\boldsymbol{x}(t) = \boldsymbol{T}\boldsymbol{z}(t)$, the system can be defined on diagonal form as:

$$\boldsymbol{R}\dot{\boldsymbol{z}}(t) = \boldsymbol{A}\boldsymbol{R}\boldsymbol{z}(t) + \boldsymbol{B}\boldsymbol{u}(t) \Leftrightarrow \dot{\boldsymbol{z}}(t) = \boldsymbol{\Lambda}\boldsymbol{z}(t) + \boldsymbol{T}^{-\boldsymbol{1}}\boldsymbol{B}\boldsymbol{u}(t) \tag{2.31}$$

This equation is, due to the diagonal form, a set of uncoupled differential equations in terms of the new states $\boldsymbol{z}(t)$. Thus, the zero-input solutions for each new states are $z_i(t) = z_i(0)e^{\lambda_i t}$, where $z_i(0)$ is the initial state value at $t = 0$. As can be seen, the mode is stable if and only if the eigenvalues λ_i lies in the open left-hand plane. Backsubstituting so that the system is represented in terms of the original states, results in:

$$\boldsymbol{x}(t) = \boldsymbol{R}\boldsymbol{z}(t) = \sum_{i=1}^{n} \boldsymbol{r_i}\boldsymbol{l_i}\boldsymbol{x}(0)e^{\lambda_i t} \tag{2.32}$$

From this equation, it is possible to find a measure of the relative participation of the state k in the i-th mode and vice versa, as described in the next subsection[21].

2.2.5 Parametric sensitivity and participation factors

The participation factor is a tool for analyzing the level of interaction between the states and the modes of a linear time-invariant system. It is a method of quantifying the degree of connection a system variable has in a system mode, which makes it possible to determine which state variables that are most relevant for a particular mode. That is, the participation factor is a measure of eigenvalue sensitivity. This approach could simplify the analysis of the system, since, instead of looking into the entire model, the main focus could lie on the state variables which interact most with the critical modes[22].

There exist several different approaches to the participation factors for a linear time-invariant system. In this report, four methods have been explored, and the different formulas for calculating the participation factor p_{ki} of the state x_k in the i-th mode are as follows[22][23]:

Method I:

$$p_{ki} = l_k^i r_k^i \tag{2.33}$$

Method II:

$$p_{ki} = \frac{(\Re\{l_k^i\})^2}{\Re\{\boldsymbol{l}^i\}(\Re\{\boldsymbol{l}^i\})^T} \tag{2.34}$$

Method III:

$$p_{ki} = \frac{|l_k^i|^2}{\sum_{j=1}^{n} |l_j^i|} \tag{2.35}$$

Method IV:

$$p_{ki} = 2\Re\{l_k^i r_k^i\}) \tag{2.36}$$

where $\boldsymbol{l}^i$ and $\boldsymbol{r}^i$ are respectively the left and right eigenvectors of the matrix $\boldsymbol{A}$ in Equation 2.8 associated with the eigenvalues λ_i for $i \in 1 \dots n$, and l_k^i and r_k^i are the k-th index of the i-th eigenvector.

Parametric sensitivity

Parametric sensitivity analysis is a tool for assessing how the parameters of the dynamic system affect the eigenvalues of the state matrix $\boldsymbol{A}$. The sensitivity of an eigenvalue to a parameter of the system can be found by taking the derivative of the eigenvalues with respect to that specific parameter. By considering a system with n states and k changeable parameters, the complex-valued parametric sensitivity matrix can be expressed as:

$$\boldsymbol{S} = \begin{pmatrix} s_{1,1} & s_{1,2} & \cdots & s_{1,k} \\ s_{2,1} & s_{2,2} & \cdots & s_{2,k} \\ \vdots & \vdots & \ddots & \vdots \\ s_{n,1} & s_{n,2} & \cdots & s_{n,k} \end{pmatrix} \in \mathbb{R}^{n \times k} \tag{2.37}$$

The matrix elements can be found according to:

$$s_{i,k} = \frac{d\lambda_i}{d\rho_k} = \frac{\boldsymbol{r}_i^H \dfrac{\partial \boldsymbol{A}}{\partial \rho_k} \boldsymbol{l}_i}{\boldsymbol{r}_i^H \boldsymbol{l}_i} \tag{2.38}$$

where ρ_k is a parameter of the system.

The real part of the elements indicates how much an eigenvalue moves along the real axis for a change in the corresponding parameter, whereas the imaginary part of the elements indicates how much the eigenvalue moves along the imaginary axis for a change in the corresponding parameter. This procedure is a useful tool for establishing which parameters to focus on in order to improve the dynamic response of the system.

As explained, eigenvalue analysis of electrical power systems is a helpful tool for analyzing small-signal stability and dynamic behavior. Linear system theory can be applied to improve performance and prevent instability. Parametric sensitivity analysis can be utilized in order to study the impacts of parameter variations on the dynamic behavior, which can be used to find the most appropriate controller gain to modify in order to improve the dynamic response of the system. Poorly damped and oscillating modes can be identified and analyzed, and participation factors can be exploited to find the states involved in the poorly damped modes, which can be used to design damping controllers[21].

2.2.6 Controllability

Controllability refers to the ability of a controller to alter the functionality of a system and is an important property in control theory – playing a major role in control problems such as feedback stabilization and optimal control.

Theorem Controllability:

The state-space representation in Equation 2.8 or the pair $(\boldsymbol{A}, \boldsymbol{B})$ is said to be controllable if for any initial state $\boldsymbol{x}(0) = \boldsymbol{x}_0$ and any final state $\boldsymbol{x}_1$, there exists and input $\boldsymbol{u}(\cdot)$ that transfer $\boldsymbol{x}_0$ to $\boldsymbol{x}_1$ in a finite time. Otherwise, the pair $(\boldsymbol{A}, \boldsymbol{B})$ is said to be uncontrollable[24]. Kalman's controllability matrix reads:

$$\boldsymbol{\mathcal{C}} = [\boldsymbol{B} \quad \boldsymbol{A}\boldsymbol{B} \quad \boldsymbol{A}^2\boldsymbol{B} \; \dots \; \boldsymbol{A}^{n-1}\boldsymbol{B}] \tag{2.39}$$

Kalman's rank criterion states that the rank of the controllability matrix needs to be n, i.e. have full row rank, for the system to be controllable. This is a binary rank condition which only states whether the system is completely controllable or not, and do not say anything about in what way the system is or is not controllable or how much input energy which is required to steer the system around in the state-space. It provides no information on how the system behaves from its inital state to its final state or on how easy it is to control the different states. Moreover, some states may also be of no practical importance for the system, indicating that these states could be less emphasized in controller design considerations. It is therefore relevant to consider more quantitative measures of controllability. The controllability Gramian handles this matter.

Controllability Gramian

The symmetric positive semidefinite matrix:

$$\boldsymbol{W}_c(t) = \int_0^t e^{\boldsymbol{A}\tau}\boldsymbol{B}\boldsymbol{B}^T e^{\boldsymbol{A}^T\tau} d\tau \in \mathbb{R}^{n\times n} \tag{2.40}$$

is called the controllability Gramian at time t. The eigenvectors and eigenvalues of this matrix are the vectors $\boldsymbol{\xi}$ and the roots λ of the characteristic polynomial of $\boldsymbol{W}_c(t)$ such that:

$$\boldsymbol{W}_c\boldsymbol{\xi} = \lambda\boldsymbol{\xi} \tag{2.41}$$

The eigenvectors corresponding to the largest eigenvalues of the Gramian are the most controllable directions in the state-space $\boldsymbol{x}(t) \in \mathbb{R}^n$. This means that it is possible to go further in the directions of the eigenvectors corresponding to larger eigenvalues than it is possible in the directions spanned by eigenvectors with a corresponding smaller eigenvalue – using the same amount of input energy. Thus, this matrix provides an energy-related quantification of controllability; it describes how much energy is required to move the system around in the state-space[25].

For stable systems, there exists a finite positive definite Gramian defined by:

$$\boldsymbol{W}_c = \int_0^\infty e^{\boldsymbol{A}\tau}\boldsymbol{B}\boldsymbol{B}^T e^{\boldsymbol{A}^T\tau} d\tau \in \mathbb{R}^{n\times n} \tag{2.42}$$

which can easily be found by solving the Lyapunov equation:

$$\boldsymbol{A}\boldsymbol{W}_c + \boldsymbol{W}_c\boldsymbol{A}^T = -\boldsymbol{B}\boldsymbol{B}^T \tag{2.43}$$

The controllable directions, i.e., the eigenvectors, and the eigenvalues of this matrix defines an energy ellipsoid in $\mathbb{R}^n$ which describes the surface of how far in any direction it is possible to steer the system with a unit or less of input energy, i.e.:

$$\mathcal{E}_{min} = \{\boldsymbol{x} \in \mathbb{R}^n \mid \boldsymbol{x}^T\boldsymbol{W}_c^{-1}\boldsymbol{x} \leq 1\} \tag{2.44}$$

From the controllability Gramian, there exist several different ways to quantify and interpret the controllability:

1) The trace of the Gramian, $tr(\boldsymbol{W}_c)$. It can be interpreted as the average controllability in all of the directions in the state-space, as it is inversely related to the average energy needed

to move the system around. If the system is uncontrollable, the average controllability would be zero because there exists at least one direction of which it is impossible to drive the system using the control inputs.

2) The determinant of the Gramian, $det(\boldsymbol{W}_c)$. It is related to the volume enclosed by the ellipsis the Gramian defines:

$$V(\mathcal{E}_{min}) = \frac{\pi^{\frac{n}{2}}}{\Gamma(\frac{n}{2}+1)} \sqrt[n]{det(\boldsymbol{W}_c)} \tag{2.45}$$

where Γ is the gamma function. That is, the determinant is a measure of the set of states that can be reached with one unit or less of input energy. However, computing the determinant could be problematic when the states n grows large, so for large systems, it is more common to consider the logarithm of the determinant instead, $log(det(\boldsymbol{W}_c))$. If the system is uncontrollable, the volume of the ellipsis would be zero.

3) The smallest eigenvalue of the Gramian, $min\{\lambda_1 \ \dots \ \lambda_n\}$. As described earlier, this measure is inversely related to the amount of energy required to move the system in the direction of the state-space that is most difficult to control. That is, the smaller the eigenvalue, the more energy needed.

4) The eigenvector corresponding to the smallest eigenvalue. This eigenvector is the direction that requires the most input energy to steer the system, compared to all other directions in the n-dimensional state-space. The eigenvectors span the controllable subspace, and the corresponding eigenvalues can be interpreted as the length of the axes.

5) The rank of the Gramian, $rank(\boldsymbol{W}_c)$. This rank is the dimension of the controllable subspace[25].

2.2.7 Observability

Observability refers to the ability of estimating any state $\boldsymbol{x}(t)$ from the measurement $\boldsymbol{y}(t)$.

Theorem Observability:

The state-space representation in Equation 2.8 is said to be controllable if for any unknown initial state $\boldsymbol{x}(0)$, there exists a finite $t_1 > 0$ such that knowledge of the input $\boldsymbol{u}$ and the output $\boldsymbol{y}$ over $[0, t_1]$ suffices to determine uniquely the initial state $\boldsymbol{x}(0)$. Otherwise the system is said to be unobservable[24]. Kalman's observability matrix reads:

$$\boldsymbol{\mathcal{O}} = [\boldsymbol{C} \quad \boldsymbol{CA} \quad \boldsymbol{CA}^2 \ \dots \ \boldsymbol{CA}^{n-1}]^T \tag{2.46}$$

Kalman's rank criterion states that the rank of this observability matrix needs to be n, i.e., have full column rank, for the system to be observable. Similarly, as for the controllability property, this is also a binary rank condition and does not say anything in what way the system is or is not observable. Some states could i.e. be observable through higher-order derivatives and thus more exposed to e.g. noise corruption, limiting observability in a practical sense. Therefore, the more quantitative observability Gramian matrix has been introduced to handle this matter as well.

Observability Gramian

The symmetric positive semidefinite matrix can be expressed as:

$$\boldsymbol{W}_o(t) = \int_0^t e^{\boldsymbol{A}\tau}\boldsymbol{C}^T\boldsymbol{C}e^{\boldsymbol{A}^T\tau}d\tau \in \mathbb{R}^{n\times n} \tag{2.47}$$

This matrix called the observability Gramian at time t. The eigenvectors and eigenvalues of this matrix are the vectors $\boldsymbol{\xi}$ and the roots λ of the characteristic polynomial of $\boldsymbol{W}_o(t)$ such that:

$$\boldsymbol{W}_o\boldsymbol{\xi} = \lambda\boldsymbol{\xi} \tag{2.48}$$

For stable systems, there exists a finite positive definite Gramian defined by:

$$\boldsymbol{W}_o = \int_0^\infty e^{\boldsymbol{A}\tau}\boldsymbol{C}^T\boldsymbol{C}e^{\boldsymbol{A}^T\tau}d\tau \in \mathbb{R}^{n\times n} \tag{2.49}$$

which can easily be found by solving the Lyapunov equation:

$$\boldsymbol{A}\boldsymbol{W}_o + \boldsymbol{W}_o\boldsymbol{A}^T = -\boldsymbol{C}^T\boldsymbol{C} \tag{2.50}$$

Controllability and observability are dual properties. Thus, all measures and interpretations of the controllability Gramian hold for the observability Gramian as well – albeit describing the degree of observability in the latter case.

2.3 Chapter summary

In this chapter, some key topics and circuit theory of IPT-systems were presented. The concept of mutual coupling and how it relates to a coupling factor was introduced, as well as some challenges IPT-technology face. The essential relationship for establishing the nonlinear CVL-conditions is given, as well as the corresponding relationship for CRL-modeling. Furthermore, important background theory, mathematical tools, and their application are explained.

Chapter 3

Frequency Characteristics

This chapter explains the procedure of achieving an expression for the output power in the IPT-system, both with CVL and CRL. Furthermore, frequency characteristics are presented, as well as some methods for modifying and shaping these characteristics in order to obtain a system suitable for frequency control to maintain constant power transfer under variable coupling conditions.

3.1 Power transfer

3.1.1 Constant voltage load

The harmonic equivalent circuit of the IPT-system is shown in Figure 3.1

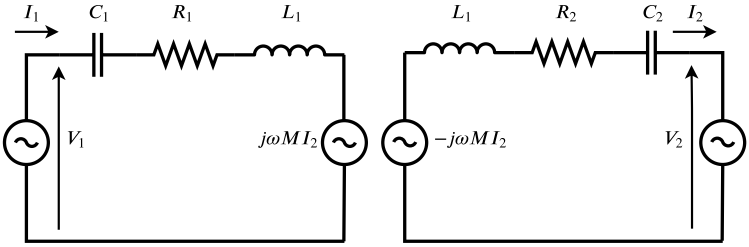

Figure 3.1: Harmonic equivalent circuit with CVL.

With conventional phasor circuit theory, the relationship between the currents and voltages in the circuit can be expressed in the frequency domain as:

$$\hat{V}_1 = R_1\hat{I}_1 + j\omega L_1\hat{I}_1 - j\omega M\hat{I}_2 + \hat{V}_{C1} \tag{3.1a}$$

$$\hat{V}_2 = -R_1\hat{I}_2 - j\omega L_1\hat{I}_2 + j\omega M\hat{I}_1 - \hat{V}_{C2} \tag{3.1b}$$

$$\hat{V}_{C1} = \frac{1}{j\omega C_1}\hat{I}_1 \tag{3.1c}$$

$$\hat{V}_{C2} = \frac{1}{j\omega C_2}\hat{I}_2 \tag{3.1d}$$

Substituting Equation 3.1c and Equation 3.1d in Equation 3.1a and Equation 3.1b, respectively, gives the following:

$$\hat{V}_1 = R_1\hat{I}_1 + j\omega L_1\hat{I}_1 - j\omega M\hat{I}_2 + \frac{1}{j\omega C_1}\hat{I}_1 \tag{3.2a}$$

$$\hat{V}_2 = -R_1\hat{I}_2 - j\omega L_1\hat{I}_2 + j\omega M\hat{I}_1 - \frac{1}{j\omega C_1}\hat{I}_2 \tag{3.2b}$$

Solving these equations for the currents $\hat{I}_1$ and $\hat{I}_2$ results in rather long and complicated expressions and are not displayed here. The are, however, reported in Appendix D. Assuming operation in resonance, $\omega = \omega_0 = \frac{1}{\sqrt{L_1C_1}} = \frac{1}{\sqrt{L_2C_2}}$, a more simple solution arises:

$$\hat{I}_1 = -\frac{j \cdot M \cdot \hat{V}_2 \cdot \omega_0 - R_2 \cdot \hat{V}_1}{M^2 \cdot \omega_0^2 + R_1 \cdot R_2} \tag{3.3a}$$

$$\hat{I}_2 = \frac{j \cdot M \cdot \hat{V}_1 \cdot \omega_0 - R_1 \cdot \hat{V}_2}{M^2 \cdot \omega_0^2 + R_1 \cdot R_2} \tag{3.3b}$$

In general, the phase of the sending side voltage can be chosen to be zero, i.e. $\angle\hat{V}_1 = 0°$ and, thus, $\hat{V}_1 = V_1$. Furthermore, since the system is operating in resonance, the phase of the sending side voltage and current has to be equal, i.e., $\angle\hat{V}_1 = \angle\hat{I}_1 = 0°$, which means that $\hat{I}_1 = I_1$. Moreover, the phase of the receiving side current needs to be equal to the phase of the receiving side voltage due to the combined action of the diode rectifier and the CVL, that is, $\angle\hat{I}_2 = \angle\hat{V}_2$. With these constraints, it is possible to treat the obtained solutions for the currents further.

Since it can be assumed that the phase of the sending side voltage and thus the sending side current is zero, it can be seen from Equation 3.3a that $\hat{V}_2$ needs to have a phase of 90° relative to the current $\hat{I}_1$ in order for the expression to become real, i.e., $\hat{V}_2 = V_2\angle 90^\circ = jV_2$. Imposing this constraint results in a receiving side current of:

$$\hat{I}_2 = \frac{j(\cdot M \cdot V_1 \cdot \omega_0 - R_1 \cdot V_2)}{M^2 \cdot \omega_0^2 + R_1 \cdot R_2} \tag{3.4}$$

Since the phase of $\hat{I}_2$, as stated above, needs to have equal phase as $\hat{V}_2$, i.e. $\hat{I}_2 = I_2\angle 90^\circ = jI_2$, the resulting currents is real quantities and can be expressed as:

$$\hat{I}_1 = I_1 = \frac{M \cdot V_2 \cdot \omega_0 + R_2 \cdot V_2}{M^2 \cdot \omega_0^2 + R_1 \cdot R_2} \tag{3.5a}$$

$$\hat{I}_2 = I_2 = \frac{M \cdot V_1 \cdot \omega_0 - R_1 \cdot V_2}{M^2 \cdot \omega_0^2 + R_1 \cdot R_2} \tag{3.5b}$$

Thus, in an ideal lossless case with $R_1 = R_2 = 0$, the currents are:

$$I_1 = \frac{V_2}{M \cdot \omega_0} \tag{3.6a}$$

$$I_2 = \frac{V_1}{M \cdot \omega_0} \tag{3.6b}$$

Interestingly, when operating in resonance, an increase in the sending side voltage will mainly increase the receiving side current almost without affecting the sending side current, and vice verse.

From these results, the ideal steady-state power flow in resonance can be expressed as:

$$P_{ideal} = P_0(k_{nom}) = V_1 \cdot I_1 = V_2 \cdot I_2 = \frac{V_1 \cdot V_2}{M \cdot \omega_0} = \frac{V_1 \cdot V_2}{k_{nom}\sqrt{L_1 \cdot L_2} \cdot \omega_0} \tag{3.7}$$

To obtain a general solution for the power dissipated to the load, CVL-behavior needs to be addressed. The fundamental relationship between the current and voltage at the receiving side can be expressed with Ohm's law as:

$$v_2 = R_{eq} \cdot i_2 \tag{3.8}$$

However, in order to represent the CVL-condition, the equivalent load resistance cannot be modeled as a constant. It must be considered that the amplitude of the voltage will remain constant during operation. In addition, the phase of the current and voltage is equal due to the constraints imposed by the diode rectifier, meaning that the quantity R_{eq} will be real.

Thus, performing the phasor equivalent substitution $\hat{V}_2 = R_{eq} \cdot \hat{I}_2$ and solving the following equations for the currents:

$$\begin{aligned} \hat{V}_1 &= R_1\hat{I}_1 + j\omega L_1\hat{I}_1 - j\omega M\hat{I}_2 + \frac{1}{j\omega C_1}\hat{I}_1 \\ R_{eq}\hat{I}_2 &= -R_1\hat{I}_2 - j\omega L_1\hat{I}_2 + j\omega M\hat{I}_1 - \frac{1}{j\omega C_1}\hat{I}_2 \end{aligned} \tag{3.9}$$

results in current expressions dependent on R_{eq}. By again exploiting the identity in Equation 3.8, i.e. multiplying the obtained result for the receiving side current $\hat{I}_2(R_{eq})$ with R_{eq}, results in a general complex expression for the receiving side voltage $\hat{V}_2$. Now a general solution for the real quantity R_{eq} can be found by solving the obtained complex expression $\hat{V}_2 = \hat{I}_2(R_{eq}) \cdot R_{eq}$ for the equivalent resistance. However, in order to obtain the correct real solution of the equivalent load resistance, the magnitude of the voltage expression needs to be considered, since $\hat{V}_2$ is complex valued.

Thus, the power delivered to the load can be found by:

$$P_{out} = V_2^2 / R_{eq}(\omega, V_1, V_2) \tag{3.10}$$

In this equation, the quantity R_{eq} will be dependent on, e.g., operating frequency ω, sending side voltage V_1 and receiving side voltage V_2, meaning it will change during operation and is thus no CRL. The general solution for this complex expression is not shown here for brevity but also reported in Appendix D.

From the simplified expression in Equation 3.7, it can easily be seen that the steady-state power flow will change as the magnetic coupling varies. This is illustrated in Figure 3.2.

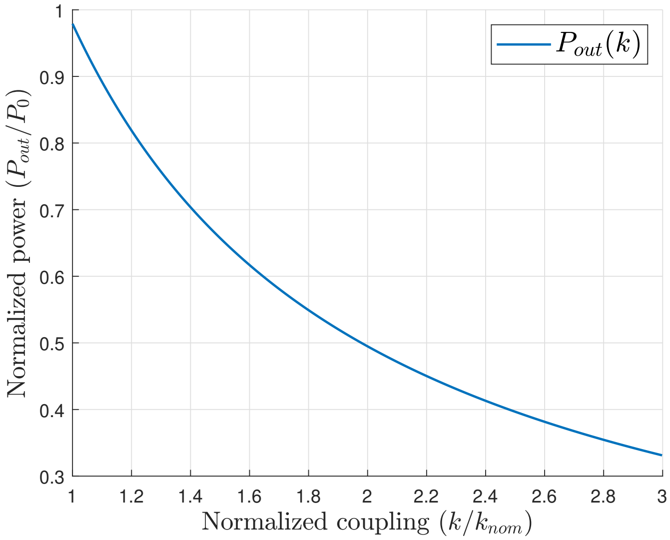

Figure 3.2: Power transferred to load under varying coupling conditions without any control strategy. Power normalized to $P_0(k_{nom})$.

Similarly, the power flow will also change when the load conditions vary.

3.1.2 Constant resistive load

With the assumption of a constant equivalent load resistance, the situation is quite different. In that case, the steady-state currents assuming resonant operation are:

$$I_1 = \frac{V_{1,0} \cdot (R_2 + R_{eq})}{R_1 \cdot (R_2 + R_{eq}) + \omega_0^2 \cdot M^2} \approx \frac{V_{1,0} \cdot R_{eq}}{\omega_0^2 \cdot M^2} \tag{3.11a}$$

$$I_2 = \frac{\omega_0 \cdot M \cdot V_{1,0}}{R_1 \cdot (R_2 + R_{eq}) + \omega_0^2 \cdot M^2} \approx \frac{V_{1,0}}{\omega_0 \cdot M} \tag{3.11b}$$

The real power transferred to the load is given by:

$$P_{out} = |I_2|^2 \cdot R_{eq} \tag{3.12}$$

where the general expression for I_2 can be found by solving Equation 3.9 for the currents.

3.2 Steady-state frequency characteristics

The nominal parameters of the IPT-system are expressed in Table 3.1.

Table 3.1: PARAMETERS OF ANALYZED IPT-SYSTEM

Nominal power, P_0	10 kW
Nominal operating frequency, f_0	85 kHz
Nominal coupling factor, k	0.2
Primary coil	
Nominal voltage, V_1	380 V
Self-inductance, L_1	176 μH
Leakage inductance, $L_{\alpha 1}$	39.36 μH
Quality factor, Q_1	310
Resonant capacitance, C_1	19.92 nF
Resistance, R_1	0.3032 Ω
Secondary coil	
Nominal voltage, V_2	235 V
Self-inductance, L_2	41 μH
Leakage inductance, $L_{\alpha 2}$	39.36 μH
Quality factor, Q_2	270
Resonant capacitance, C_2	85.51 nF
Resistance, R_2	0.0811 Ω

The resonant frequency is defined according to:

$$\omega = \omega_0 = \frac{1}{\sqrt{C_1 L_1}} = \frac{1}{\sqrt{C_2 L_2}} = 2\pi \cdot f_0 = 5.3407 \cdot 10^5 \text{ rad/s} \tag{3.13}$$

3.2.1 Control strategies

In order to keep the output power constant when operating under different coupling conditions, a control strategy could be to regulate the excitation frequency accordingly. However, keeping the output power constant with frequency control is no straightforward task, and some considerations need to be taken in order for that to happen.

Figure 3.3 shows the frequency characteristics, i.e., the power transfer as a function of operating frequency, of the CVL IPT-system under variable operating conditions. The system is nominally configured with the parameters reported in Table 3.1.

Figure 3.3a illustrates the frequency characteristics under variable coupling conditions, and it can be observed that the possible output power is well below the power reference when the magnetic coupling increases. At low coupling, wanted power transfer can only happen close to the limit frequencies, which is undesired, as a small change in the operating frequency will significantly affect the power transfer. Furthermore, it can be seen that the frequency range where non-zero power transfer can take place widens as the coupling conditions increases. The shape of the curves, however, is quite similar for all four conditions.

The characteristics displayed in Figure 3.3b shows the power transfer capabilities with varying load voltage. It can be seen that the shape of the curves is significantly altered when the load voltage is varied. At low load, two pronounced power peaks close to the limit frequencies can be observed, whereas, at higher load, the number of power peaks is reduced to one, taking place at the resonance frequency. Thus, wanted output power can only take place close to the limit frequencies in the case for high load conditions. Moreover, the range of possible power transfer gets more narrow as the load increases.

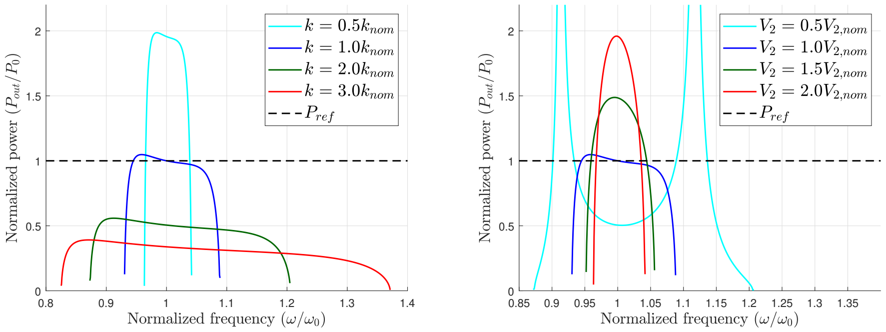

(a) Variable coupling conditions.

(b) Variable load conditions.

Figure 3.3: Frequency characteristics showing power transfer under varying operating conditions. Power normalized to $P_0 = P_0(k_{nom}, V_{2,nom})$ for both cases.

Lowering the sending side voltage will shift these curves down, and vice verse, as well as modifying their shape. In the case with varying load conditions, frequency control is maybe not the best choice of control strategy. As can be seen, in an operating condition corresponding to one single peak in the power transfer characteristics, either lowering or increasing the operating frequency will decrease the power. However, if the load condition drops below a certain voltage, two peaks will appear, and the characteristics will have a local minimum at the resonant frequency. Thus, in that case, both lowering and increasing the frequency will increase the power transfer. Operating in resonance and shifting the observed curves up or down by changing the sending side voltage could be a more suitable choice.

In the case with low coupling factor, $k = 0.5k_{nom}$, the voltage needs to be reduced in order for wanted power transfer to take place away from the limit frequencies. With higher coupling conditions, however, it is possible to take advantage of the curve shapes and the increasing frequency range by introducing some design techniques, making frequency control an appropriate choice. Thus, a combined voltage/frequency control can ideally be applied to the system to keep wanted output power, and whether to change the frequency or voltage depends on the current operating conditions. Indeed, solely controlling the sending side voltage in order to maintain constant power flow is possible. The sending side current will, however, change accordingly, thus possibly increasing the volt-ampere requirements of the supply. An off-resonant frequency control strategy could reduce this problem.

It should be noted that the IPT-parameters used in this thesis initially was intended for an IPT-system operating in resonance with voltage control to regulate the output power. In general, when designing an IPT-system, the intended control strategy and the desired application should be carefully considered, as parameters such as, e.g., input/output voltage and self-inductance's have a significant impact on the frequency characteristics of the system, as indicated above. Thus, the nominal parameters used here may not be optimal for the planned control scheme, and there are, therefore, some matters which need extra attention.

In the following, frequency control to maintain constant power under variable coupling conditions will be explored, considering the range $k_{nom} \leq k \leq 3k_{nom}$.

3.2.2 Coil unbalancing

By introducing an unbalance factor defined according to:

$$x_u = \sqrt{\frac{L_1}{L_2}}\frac{V_2}{V_1} \tag{3.14}$$

and utilizing a design rule as follows:

$$V_1 = \sqrt{\frac{L_1}{L_2}}\frac{V_2}{x_u} \tag{3.15}$$

it is possible to shape the frequency characteristics of the IPT-system[15].

The effect of unbalancing is shown in Figure 3.4.

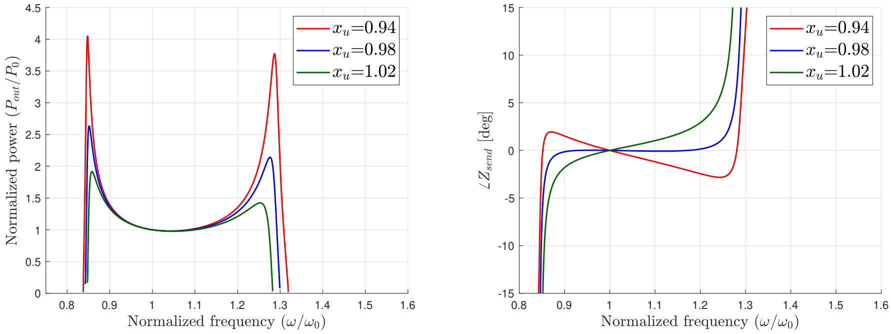

(a) Power transferred to the load.

(b) Argument of impedance seen by the source.

Figure 3.4: Frequency characteristics showing the effect of unbalancing, coupling factor k = 0.4.

The argument of the impedance seen by the source is found from the expression:

$$\angle Z_{send} = \arctan\left(\frac{v_{1,d,0} + jv_{1,q,0}}{i_{1,d,0} + ji_{1,q,0}}\right) \tag{3.16}$$

As Figure 3.4 illustrates, introducing some unbalance has a significant impact on the steady-state frequency characteristics of the system. Figure 3.4a shows that the range of power regulation increases as the unbalance factor decreases, and the power peaks close to the limit frequencies get more prominent.

Figure 3.4b shows how the unbalancing affects the phase characteristics of the equivalent impedance seen by the sending side converter. Monotonous phase characteristics appear when the unbalance factor is higher than 1.00, while the phase characteristics cross zero phase angle three times with an unbalance factor lower than that, i.e., the sign of the derivative changes along the curve. This phenomenon is called *bifurcation*; the impedance switches from inductive to capacitive or vice verse, thus changing the behavior of the H-bridge converter.

3.2.3 Coil detuning

It is possible to shape the frequency characteristics further by introducing a detuning factor defined according to:

$$x_c = \frac{C_1 \cdot L_1}{C_2 \cdot L_2} > 1 \text{ or } x_c = \frac{C_1 \cdot L_1}{C_2 \cdot L_2} < 1 \tag{3.17}$$

This detuning factor ensures different resonant frequencies at the sending and receiving side of the IPT-system. The effect of detuning is illustrated in Figure 3.5.

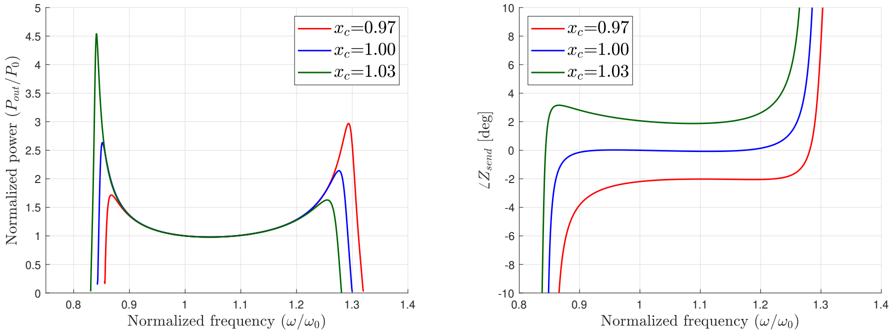

(a) Power transferred to the load. **(b)** Argument of impedance seen by the source.

Figure 3.5: Frequency characteristics showing the effect of detuning, coupling factor k = 0.4, unbalance factor x_u = 0.98.

As seen from Figure 3.5a, a detuning factor of $x_c > 1$ increases the range of possible power transfer at frequencies lower than the resonant frequency. The sub-resonant power peak close to the limit frequency is significantly enhanced. In contrast, a factor of $x_c < 1$ increases the range of possible power transfer at higher frequencies, emphasizing the super-resonant power peak.

Figure 3.5b shows how the detuning affects the phase characteristics, and it can be seen that a detuning factor of $x_c > 1$ provides a positive phase angle over the whole frequency range of particular interest, which means that the equivalent impedance seen by the sending side converter is inductive. A factor of $x_c < 1$ provides in contrast a negative phase angle, meaning that the equivalent impedance is capacitive. Operation with unity detuning factor corresponds to having the same resonant frequency at either side of the link, and the phase characteristics imply that the impedance will be close to pure resistive over the whole range of interest. An inductive impedance is preferable as this will lead to zero voltage switching with a low current of all semiconductor devices and thereby limiting the switching losses, thus favoring sub-resonant operation[15]. Both methods are, however, explored in the following.

A detuning factor of $x_c > 1$ corresponds to a higher resonant frequency at the receiving side compared to the sending side, whereas a detuning factor of $x_c < 1$ corresponds to a lower resonant frequency at the receiving side, since the IPT-system is detuned according to:

$$C_1 = x_c \cdot \frac{C_2 \cdot L_2}{L_1} \tag{3.18}$$

3.2.4 Comparison with different load modeling

Figure 3.6 shows the differences in the frequency characteristics between CRL and CVL with a perfectly tuned system $x_c = x_u = 1.00$.

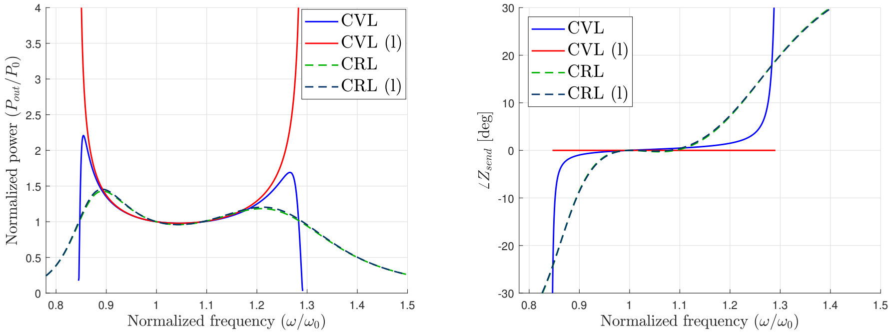

(a) Power transferred to the load. **(b)** Argument of impedance seen by the source.

Figure 3.6: Frequency characteristics comparing CVL and CRL, coupling factor $k = 0.4$, detuning factor $x_c = 1$, unbalance factor $x_u = 1$, (l) denotes a lossless system.

As evident from Figure 3.6, significant discrepancies between the characteristics with CVL and CRL can be observed when considering off-resonant operation. In the lossless case with CVL, the power peaks near the limit frequencies approach infinity, whereas in the case with CRL, the power flow is always bounded. It can also be seen that losses in the system profoundly affects the CVL-characteristics, as the power flow, in this case, is bounded from above, whereas in the case with CRL, losses do not have any significant effect. Moreover, the equivalent sending side impedance with CVL is always zero in the feasible frequency range with an ideal lossless case and close to zero taking losses into account. In the CRL case, notably more variation in the impedance phase angle with the frequency can be observed.

In Figure 3.7, differences in the two load modeling approaches with detuning is illustrated.

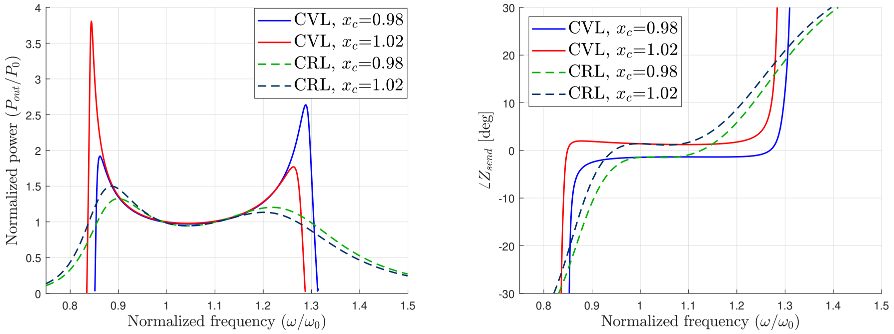

(a) Power transferred to the load. **(b)** Argument of impedance seen by the source.

Figure 3.7: Frequency characteristics comparing CVL and CRL, coupling factor $k = 0.4$, unbalance factor $x_u = 1$.

As seen, coil detuning has a significant more influence on both the phase and power characteristics with CVL compared to CRL. It is possible to take advantage of these differences, which is seen in the following.

The characteristics are drawn with an equivalent resistance of $R_{eq} = \omega_0 \cdot k \cdot L_2$.

Coil unbalancing will only shift the curves with CRL upwards or downwards. Thus, they will perfectly coincide when normalized to their respective values of x_u. Comparison between CVL and CRL with unbalancing is, therefore, omitted.

3.2.5 Constant power transfer in sub-resonant operation

Adding an appropriate amount of unbalancing and detuning can ensure that there indeed exists a combination of coupling factor and operating frequency such that maintaining constant power flow is possible through frequency control.

Due to the nominal parameters originally being designed for a system intended for a different strategy, in particular, with $x_{u,nom} \approx 1.28$, the following inequality arose:

$$P_{out}(\omega_0, k_{nom}, x_u = 0.98, x_c = 1.03) > P_0(k_{nom}) \tag{3.19}$$

Therefore, normalization to $P_0(k_{nom})$ would make it impossible to obtain 1 pu power transfer at low coupling conditions with frequency control, i.e. without changing the sending side voltage accordingly, so normalization to $P_{out}(\omega_0, k_{nom}, x_u, x_c)$ is done instead. The main idea is equivalent, regardless.

Figure 3.8 shows the frequency characteristics for three different coupling conditions where a sub-resonant operation is emphasized.

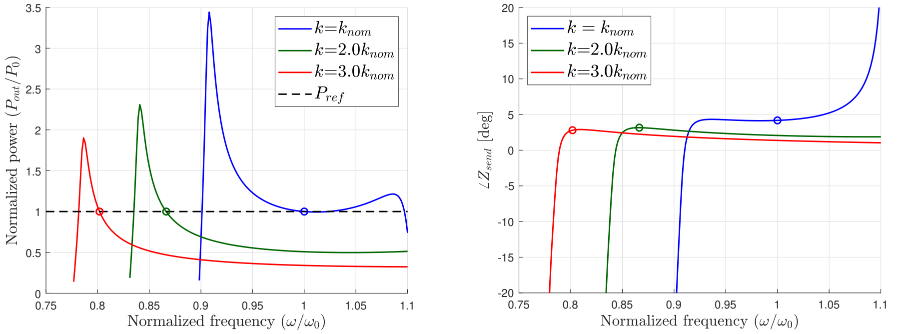

(a) Power transferred to the load.

(b) Argument of impedance seen by the source.

Figure 3.8: Frequency characteristics with variable coupling conditions in sub-resonant operation. Power normalized to $P_{out}(\omega_0, k_{nom}, x_u, x_c)$, unbalance factor x_u = 0.98, detuning factor x_c = 1.03. Operating points marked with a circle.

It can be seen from Figure 3.8a that, by adding an unbalance factor of $x_u = 0.98$ and a detuning factor of $x_c = 1.03$, power transfer can be maintained at 1 pu by regulating the frequency in sub-resonant range when the coupling condition varies. Figure 3.8b shows the phase characteristics for the same conditions and indicates that the sending side impedance will remain slightly inductive during the intended operation. Figure 3.9 shows the frequency trajectory as a function of the coupling factor k needed to maintain constant power, as well as the corresponding output power as a function of both the operating frequency ω and coupling factor k. Same coil design and power normalization as above.

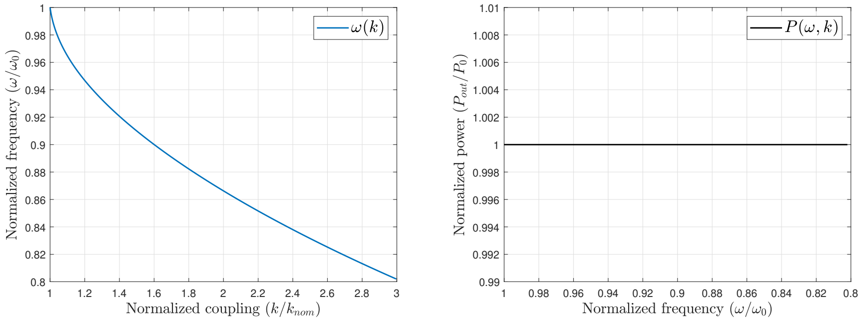

(a) Frequency trajectory.

(b) Power transferred to the load.

Figure 3.9: Frequency trajectory for maintaining constant power in sub-resonant range under variable coupling condition and the corresponding power transfer.

Clearly, the output power calculated as a function of the coupling factor and operating frequency is maintained at the reference with the intended strategy.

Figure 3.10 shows the value of the sending side current and equivalent sending side impedance phase angle during the proposed operation. As suggested, the impedance stays slightly inductive during the intended control method, illustrated i Figure 3.10b. Furthermore, the value is monotonously decreasing, meaning there are no sign change of the derivative. Thus, problems with bifurcation are avoided. Since the sending side voltage is kept constant, the sending side current is expected to be close to constant as well. From Figure 3.10a, a slight reduction of the current can be observed. This reduction can be expected due to the change in reactive power at the sending side as the excitation frequency drops far from resonance.

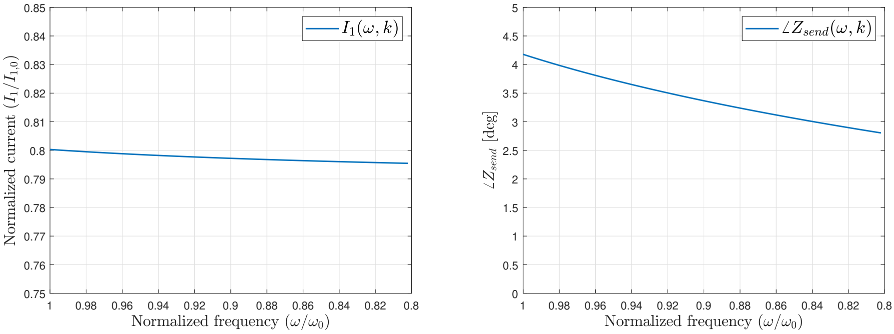

(a) Sending side current.

(b) Impedance seen by the source.

Figure 3.10: Sending side current and phase angle of the input impedance seen by the source during sub-resonant operation under variable coupling conditions.

The sending side current is normalized to:

$$I_{1,0} = \frac{P_{out}(\omega_0, k_{nom}, x_u, x_c)}{V_{1,nom}} \tag{3.20}$$

3.2.6 Constant power transfer in super-resonant operation

Similarly, as above, an appropriate amount of unbalancing and detuning can also ensure that constant output power can be maintained with super-resonant frequency control under variable coupling conditions. Figure 3.8 shows the frequency characteristics for three different coupling conditions where super-resonant frequency range is emphasized.

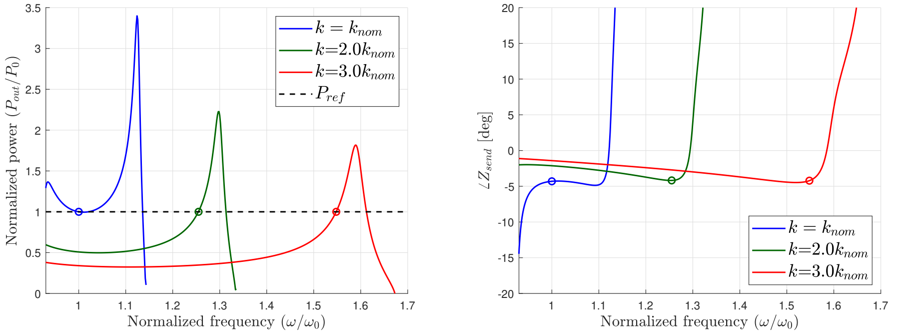

(a) Power transferred to the load. **(b)** Argument of impedance seen by the source.

Figure 3.11: Frequency characteristics with variable coupling conditions in super-resonant operation. Power normalized to $P_{out}(\omega_0, k_{nom}, x_u, x_c)$, unbalance factor x_u = 0.95, detuning factor x_c = 0.97. Operating points marked with a circle.

As can be seen from Figure 3.11a, by adding some unbalance and detuning, in this case, an unbalance factor of $x_u = 0.95$ and detuning factor of $x_c = 0.97$, power transfer can also be maintained at 1 pu by regulating the frequency in super-resonant range with different magnetic coupling. Figure 3.11b shows the phase characteristics for the same conditions, and, as opposed to sub-resonant frequency control, indicates that the sending side equivalent impedance will remain slightly capacitive during the entire operating range. Figure 3.12 shows the excitation frequency as a function of the coupling factor k needed to maintain constant output power, together with the corresponding output power – with same coil design and power normalization as for the case above.

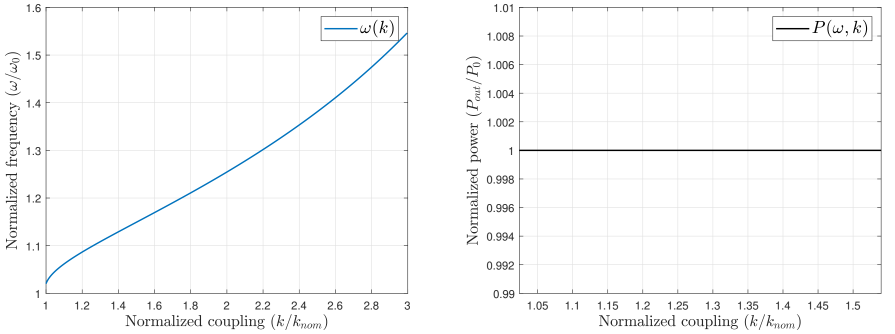

(a) Frequency trajectory. **(b)** Power transferred to the load.

Figure 3.12: Frequency trajectory for maintaining constant power in super-resonant operation under variable coupling condition and the corresponding power transfer.

As expected, the output power as a function of the coupling factor and the operating frequency is kept at the reference here as well.

Figure 3.13 shows the sending side current and sending side impedance phase angle during the super-resonant frequency control. As opposed to sub-resonant frequency control, the impedance remains slightly capacitive during the intended control method, as illustrated in Figure 3.13b. The sending side current is shown in Figure 3.13a, and it can be seen that the current is only subject to minor variations.

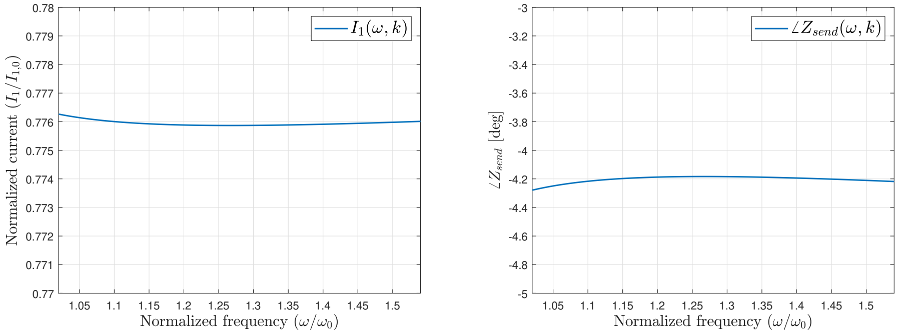

(a) Sending side current.

(b) Impedance seen by the source.

Figure 3.13: Sending side current and phase angle of the input impedance seen by the source during super-resonant operation under variable coupling conditions.

The sending side current is normalized to the same base value as earlier:

$$I_{1,0} = \frac{P_{out}(\omega_0, k_{nom}, x_u, x_c)}{V_{1,nom}} \tag{3.21}$$

As earlier mentioned, controlling the output power by regulating the voltage in resonance or by regulating the operating frequency will impose contrasting stress on the sending side converter. Figure 3.14 illustrates how the sending side voltage and current will change as a function of the coupling conditions under the two mentioned control strategies. The volt-ampere-requirements of the H-bridge converter is clearly higher in the case with voltage control in resonance compared to off-resonant frequency control, as the current is inversely related to the voltage and will increase as the coupling conditions decreases due to the reduced voltage. In the case with varying frequency, the sending side voltage is kept constant, and, therefore, the current will remain close to constant as well.

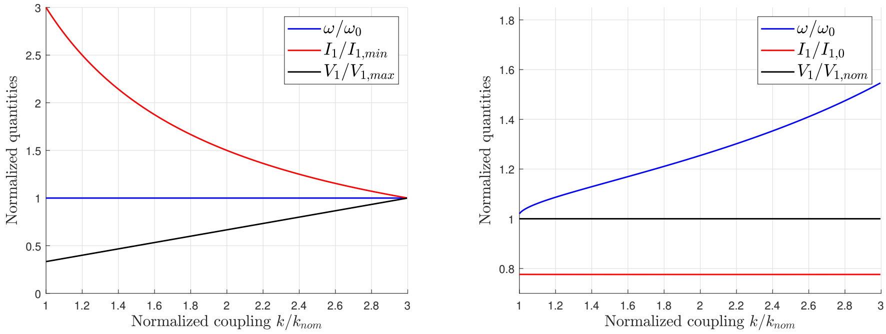

(a) Resonant operation. **(b)** Super-resonant operation.

Figure 3.14: Variation of sending side voltage and current for maintaining constant power transfer under variable coupling conditions.

A similar result as in Figure 3.14b can be obtained in the case for sub-resonant operation as well, albeit with a decreasing frequency trajectory curve and a slightly different sending side current.

3.3 Chapter summary

In this chapter, a method for obtaining an expression for the output power for an SS-compensated IPT-system with CVL as well as CRL have been described. Moreover, power transfer capabilities and the equivalent sending side impedance characteristics have been explored and shaped by introducing coil unbalancing and detuning in order to achieve a system suitable for frequency control to keep the power flow constant under variable coupling conditions. It is seen that both sub- and super-resonant operations can provide similar results. However, the latter case will imply capacitive operation of the sending side converter, whereas inductive operation is ensured when operating in a sub-resonant range.

Chapter 4

Nonlinear and Small-Signal State-Space Models

This chapter presents the derivation procedure of a nonlinear state-space model representing the current and voltage envelopes of an SS-compensated IPT-system with CVL. The nonlinear model is expressed with direct-quadrature (dq)-axis state variables in a synchronous reference frame (SRF). Furthermore, a linearized model suitable for small-signal analysis in any feasible operating condition will be derived and presented as well as the linearization procedure for obtaining this model, both with CVL and CRL.

4.1 State-space model in synchronous reference frame

The differential equations describing the dynamics of the system in Figure 2.1 can be obtained by applying KVL around the sending- and pickup coil:

$$v_1 = R_1 i_1 + L_1 \frac{di_1}{dt} - M\frac{di_2}{dt} + v_{C1} \tag{4.1a}$$

$$v_2 = -R_2 i_2 - L_2 \frac{di_2}{dt} + M\frac{di_1}{dt} - v_{C2} \tag{4.1b}$$

$$\frac{dv_{C_1}}{dt} = \frac{1}{C_1} i_1 \tag{4.1c}$$

$$\frac{dv_{C_2}}{dt} = \frac{1}{C_2} i_2 \tag{4.1d}$$

All variables of this model will be time-periodic when reached steady-state. These time-periodic variables obstruct the model to be represented in a state-space formulation where the state variables arrive at a constant value when evaluated at the equilibrium point. In order to assess a variety of stability properties and control theory measures, a steady-state time-invariant state-space representation is required. This time-invariant representation can be achieved by considering modeling approaches such as dynamic phasors or representing the time-periodic variables in a synchronously rotating dq-reference frame[26], which have been widely utilized in litterature[27][28][29][30].

Rearranging the equations of the model obtained above and expressing the model with the derivatives of the state variables on the left-hand side, i.e., solving equations Equation 4.1a and Equation 4.1b for the derivatives of the current, results in:

$$\frac{di_1}{dt} = \frac{1}{L_1}(v_1 - R_1 i_1 - v_{C1} + M\frac{di_2}{dt}) \tag{4.2a}$$

$$\frac{di_2}{dt} = \frac{1}{L_2}(-v_2 - R_2 i_2 - v_{C2} + M\frac{di_1}{dt}) \tag{4.2b}$$

These two equations are connected due to the mutual coupling between the coils, that is, the derivative of the current in the sending coil shows up in the equation describing the dynamics of the pickup coil, and vice verse. Therefore, substituting equation Equation 4.2b in Equation 4.2a, gives:

$$\begin{aligned}
\frac{di_1}{dt} &= \frac{1}{L_1}(v_1 - R_1 i_1 - v_{C1} + \frac{M}{L_2}(-v_2 - R_2 i_2 - v_{C2} + M\frac{di_1}{dt}))\\
\Rightarrow \frac{di_1}{dt}(1 - \frac{M^2}{L_1 L_2}) &= \frac{1}{L_1}(v_1 - R_1 i_1 - v_{C1} - \frac{M}{L_2}v_2 - \frac{MR_2}{L_2}i_2 - \frac{M}{L_2}v_{C2})\\
\Rightarrow \frac{di_1}{dt} &= \frac{1}{L_1 - \frac{M^2}{L_2}}(v_1 - R_1 i_1 - v_{C1} - \frac{M}{L_2}v_2 - \frac{MR_2}{L_2}i_2 - \frac{M}{L_2}v_{C2})\\
\Rightarrow \frac{di_1}{dt} &= -\frac{R_1}{L_{\alpha 1}}i_1 - \frac{MR_2}{L_{\alpha 1}L_2}i_2 - \frac{1}{L_{\alpha 1}}v_{C1} - \frac{M}{L_{\alpha 1}L_2}v_{C2} + \frac{1}{L_{\alpha 1}}v_1 - \frac{M}{L_{\alpha 1}L_2}v_2
\end{aligned} \tag{4.3a}$$

Applying the same procedure for equation Equation 4.2b, i.e. substituting equation Equation 4.2a in equation Equation 4.2b, gives:

$$\frac{di_2}{dt} = -\frac{MR_1}{L_{\alpha 2}L_1}i_1 - \frac{R_2}{L_{\alpha 2}}i_2 - \frac{M}{L_{\alpha 2}L_1}v_{C1} - \frac{1}{L_{\alpha 2}}v_{C2} + \frac{M}{L_{\alpha 2}L_1}v_1 - \frac{1}{L_{\alpha 2}}v_2 \tag{4.4}$$

with the leakage factors defined according to:

$$\begin{aligned}
L_{\alpha 1} &= L_1 - \frac{M^2}{L_2}\\
L_{\alpha 2} &= L_2 - \frac{M^2}{L_1}
\end{aligned} \tag{4.5}$$

4.1.1 Synchronous reference frame

Expressing the model by dq-axis state variables, the phase angle and amplitude of the first harmonic frequency components of the currents and voltages in the IPT-system can be accurately represented. The d- and q-axis state variables are equivalent to the real and imaginary parts of dynamic phasor models. In a dq-frame, time-periodic ac-signals appear as dc-signals, thus allowing for linearization. This procedure of changing the reference frame is called the Park-transformation and is commonly applied to electrical systems with time-periodic signals so that, e.g., a proportional-integral controller can be implemented to achieve zero steady-state error.

Since Park-transformation requires two orthogonal signals, it is not directly applicable to single-phase systems. Therefore, a set of fictive orthogonal quantities phase-shifted from the real quantities by a quarter of the fundamental period can be assumed, such that they together form a stationary frame, thus allowing for Park-transformation[31][32]. These quantities are indicated with arrow notation in the following.

The systems operating frequency is defined by ω, which is related to the angle θ through the equality $\theta = \omega t$.

Thus, applying a transformation such that the model is represented in an SRF according to $x_{dq} = \vec{x} \cdot e^{-j\theta}$, by multiplying both sides of Equation 4.3a with the term $e^{-j\theta}$, results in:

$$\begin{aligned}\frac{d\vec{i}_1}{dt} \cdot e^{-j\theta} = &-\frac{R_1}{L_{\alpha 1}} \underbrace{\vec{i}_1 \cdot e^{-j\theta}}_{i_{1,dq}} - \frac{MR_2}{L_{\alpha 1}L_2} \underbrace{\vec{i}_2 \cdot e^{-j\theta}}_{i_{2,dq}} - \frac{1}{L_{\alpha 1}} \underbrace{\vec{v}_{C1} \cdot e^{-j\theta}}_{v_{C1,dq}} - \frac{M}{L_{\alpha 1}L_2} \underbrace{\vec{v}_{C2} \cdot e^{-j\theta}}_{v_{C2,dq}} \\ &+ \frac{1}{L_{\alpha 1}} \underbrace{\vec{v}_1 \cdot e^{-j\theta}}_{v_{1,dq}} - \frac{M}{L_{\alpha 1}L_2} \underbrace{\vec{v}_2 \cdot e^{-j\theta}}_{v_{2,dq}}\end{aligned} \tag{4.6}$$

By noting that $x_{dq} = \vec{x} \cdot e^{-j\theta} \iff \vec{x} = x_{dq} \cdot e^{j\theta}$ and using the relationship $\theta = \omega t$, it is possible to treat the derivative term on the left hand side:

$$\begin{aligned}\frac{d\vec{i}_1}{dt} \cdot e^{-j\theta} &= (\frac{d}{dt}(i_{1,dq} \cdot e^{j\omega t}))e^{-j\omega t} \\ &= (\frac{di_{1,dq}}{dt}e^{j\omega t} + j\omega \cdot i_{1,dq} \cdot e^{j\omega t})e^{-j\omega t} \\ &= \frac{di_{1,dq}}{dt} + j\omega \cdot i_{1,dq}\end{aligned} \tag{4.7}$$

This result is valid when assuming a time-invariant operating frequency. Furthermore, it is an accurate approximation as long as the frequency is slowly varying and do not change notably within one period[26]. In this case, the assumption of $\omega(t) \approx \omega$ provides a precise result. If very rapid variations of the frequency were present, i.e. $\omega = \omega(t)$, the time derivative of the term $j\omega(t) \cdot t$ resulting from the chain rule would be $j\omega(t) + j\frac{d\omega(t)}{dt}t$. This above concerns will, however, not limit the intended application in this work, as variations in the frequency will be slow and thus not violate the assumption.

By combining these above results, a differential vector equation describing the current at the sending side arises:

$$\begin{aligned}\frac{di_{1,dq}}{dt} = & -j\omega\cdot i_{1,dq} - \frac{R_1}{L_{\alpha1}}\cdot i_{1,dq} - \frac{MR_2}{L_{\alpha1}L_2}\cdot i_{2,dq} - \frac{1}{L_{\alpha1}}\cdot v_{C1,dq} \\ & - \frac{M}{L_{\alpha1}L_2}\cdot v_{C2,dq} + \frac{1}{L_{\alpha1}}\cdot v_{1,dq} - \frac{M}{L_{\alpha1}L_2}\cdot v_{2,dq}\end{aligned} \tag{4.8}$$

A similar procedure for Equation 4.2b, i.e., applying the Park transformation, results in a differential vector equation describing the current at the receiving side:

$$\begin{aligned}\frac{di_{2,dq}}{dt} = & -j\omega\cdot i_{2,dq} - \frac{MR_1}{L_{\alpha2}L_1}\cdot i_{1,dq} - \frac{R_2}{L_{\alpha2}}\cdot i_{2,dq} - \frac{M}{L_{\alpha2}L_1}\cdot v_{C1,dq} \\ & - \frac{1}{L_{\alpha2}}\cdot v_{C2,dq} + \frac{M}{L_{\alpha2}L_1}\cdot v_{1,dq} - \frac{1}{L_{\alpha2}}\cdot v_{2,dq}\end{aligned} \tag{4.9}$$

Furthermore, applying the dq-transformation on the last two equations of the model, Equation 4.1c and Equation 4.1d, results in:

$$\frac{d\vec{v}_{C1}}{dt}\cdot e^{-j\theta} = \frac{1}{C_1}\vec{i}_1\cdot e^{-j\theta} \tag{4.10a}$$

$$\frac{d\vec{v}_{C2}}{dt}\cdot e^{-j\theta} = \frac{1}{C_2}\vec{i}_2\cdot e^{-j\theta} \tag{4.10b}$$

By treating the derivative terms as before, the following is obtained:

$$\begin{aligned}\frac{d\vec{v}_{C1}}{dt}\cdot e^{-j\theta} &= (\frac{d}{dt}(v_{C1,dq}\cdot e^{j\omega t}))e^{-j\omega t} \\ &= (\frac{dv_{C1,dq}}{dt}\cdot e^{j\omega t} + j\omega\cdot v_{C1,dq}\cdot e^{j\omega t})e^{-j\omega t} \\ &= \frac{dv_{C1,dq}}{dt} + j\omega\cdot v_{C1,dq}\end{aligned} \tag{4.11}$$

and:

$$
\begin{aligned}
\frac{d\vec{v}_{C2}}{dt} \cdot e^{-j\theta} &= (\frac{d}{dt}(v_{C2,dq} \cdot e^{j\omega t}))e^{-j\omega t} \\
&= (\frac{dv_{C2,dq}}{dt} \cdot e^{j\omega t} + j\omega \cdot v_{C2,dq} \cdot e^{j\omega t})e^{-j\omega t} \\
&= \frac{dv_{C2,dq}}{dt} + j\omega \cdot v_{C2,dq}
\end{aligned} \tag{4.12}
$$

Thus, the two differential vector equations describing the voltages across the capacitors at both sending- and pickup coil arises:

$$
\frac{dv_{C1,dq}}{dt} = -j\omega \cdot v_{C1,dq} + \frac{1}{C_1} \cdot i_{1,dq} \tag{4.13a}
$$

$$
\frac{dv_{C2,dq}}{dt} = -j\omega \cdot v_{C2,dq} + \frac{1}{C_2} \cdot i_{2,dq} \tag{4.13b}
$$

The time-varying ac-signals in Equation 4.1a-4.1d can now be represented as dc-signals from the real and complex terms of the dq-axis state variables, similarly to dynamic phasor-based modeling. However, the cross-coupling terms $j\omega \cdot x_{dq}$ resulting from Park-transformation, where x_{dq} represents an arbitrary dq-axis state variable, impose a nonlinearity to the state-space representation.

4.1.2 Constant voltage load and nonlinearity

In order to represent the CVL-characteristic of the model, the voltage at the receiving side should be expressed in terms of the output voltage $V_{dc,out}$ and receiving coil current i_2 due to the action of the diode rectifier. Imposing the constraints described in Section 2.1.4, the fundamental frequency component of the voltage v_2 can be expressed as[18]:

$$
v_2 = \frac{i_2}{I_2} \cdot \frac{4}{\pi} \cdot V_{dc,out} \tag{4.14}
$$

where I_2 is the amplitude of i_2. In the dq-reference frame, the amplitude I_2 is the euclidean norm of the complex vector $i_{2,dq}$, i.e. $|i_{2,dq}| = \sqrt{i_{2,d}^2 + i_{2,q}^2}$. Thus, the voltage at the receiving side is expressed in dq-components as:

$$
v_{2,dq} = \frac{i_{2,dq}}{\sqrt{i_{2,d}^2 + i_{2,q}^2}} \cdot \frac{4}{\pi} \cdot V_{dc,out} \tag{4.15}
$$

As can be seen from the expression above, some state variables now appear both squared and under square roots, as well as multiplied by the input signal $V_{dc,out}$. Therefore, more nonlinearity is introduced to the system.

The overall model is now described in dq-coordinates by four nonlinear complex vector equations of the form:

$$\begin{aligned}\frac{di_{1,dq}}{dt} =& -j\omega \cdot i_{1,dq} - \frac{R_1}{L_{\alpha 1}} \cdot i_{1,dq} - \frac{MR_2}{L_{\alpha 1}L_2} \cdot i_{2,dq} - \frac{1}{L_{\alpha 1}} \cdot v_{C1,dq} - \frac{M}{L_{\alpha 1}L_2} \cdot v_{C2,dq} \\ &+ \frac{1}{L_{\alpha 1}} \cdot v_{1,dq} - \frac{M}{L_{\alpha 1}L_2} \cdot \frac{i_{2,dq}}{\sqrt{i_{2,d}^2 + i_{2,q}^2}} \cdot \frac{4}{\pi} \cdot V_{dc,out}\end{aligned} \tag{4.16}$$

$$\begin{aligned}\frac{di_{2,dq}}{dt} =& -j\omega \cdot i_{2,dq} - \frac{MR_1}{L_{\alpha 2}L_1} \cdot i_{1,dq} - \frac{R_2}{L_{\alpha 2}} \cdot i_{2,dq} - \frac{M}{L_{\alpha 2}L_1} \cdot v_{C1,dq} - \frac{1}{L_{\alpha 2}} \cdot v_{C2,dq} \\ &+ \frac{M}{L_{\alpha 2}L_1} \cdot v_{1,dq} - \frac{1}{L_{\alpha 2}} \cdot \frac{i_{2,dq}}{\sqrt{i_{2,d}^2 + i_{2,q}^2}} \cdot \frac{4}{\pi} \cdot V_{dc,out}\end{aligned} \tag{4.17}$$

$$\frac{dv_{C1,dq}}{dt} = -j\omega \cdot v_{C1,dq} + \frac{1}{C_1} \cdot i_{1,dq} \tag{4.18}$$

$$\frac{dv_{C2,dq}}{dt} = -j\omega \cdot v_{C2,dq} + \frac{1}{C_2} \cdot i_{2,dq} \tag{4.19}$$

4.1.3 General nonlinear state-space representation

Decomposing these above equations into real and complex terms by representing them on dq-form with $x_{dq} = x_d + jx_q$, a nonlinear state-space model is obtained, expressed in the general from $\dot{\boldsymbol{x}} = \boldsymbol{f}(\boldsymbol{x}, \boldsymbol{u})$ with the state- and input variables $\boldsymbol{x}$ and $\boldsymbol{u}$ defined as:

$$\boldsymbol{x} = \begin{bmatrix} i_{1,d} & i_{1,q} & i_{2,d} & i_{2,q} & v_{C1,d} & v_{C1,q} & v_{C2,d} & v_{C2,q} \end{bmatrix}^T \tag{4.20}$$

$$\boldsymbol{u} = \begin{bmatrix} v_{1,d} & v_{1,q} & \omega & V_{dc,out} \end{bmatrix}^T \tag{4.21}$$

The resulting nonlinear model of the system from Figure 2.1 is therefore given by:

$$\begin{aligned}\frac{di_{1,d}}{dt} =&\omega \cdot i_{1,q} - \frac{R_1}{L_{\alpha 1}} \cdot i_{1,d} - \frac{MR_2}{L_{\alpha 1}L_2} \cdot i_{2,d} - \frac{1}{L_{\alpha 1}} \cdot v_{C1,d} - \frac{M}{L_{\alpha 1}L_2} \cdot v_{C2,d} \\ &+ \frac{1}{L_{\alpha 1}} \cdot v_{1,d} - \frac{M}{L_{\alpha 1}L_2} \cdot \frac{i_{2,d}}{\sqrt{i_{2,d}^2 + i_{2,q}^2}} \cdot \frac{4}{\pi} \cdot V_{dc,out}\end{aligned} \tag{4.22}$$

$$\begin{aligned}\frac{di_{1,q}}{dt} =&-\omega \cdot i_{1,d} - \frac{R_1}{L_{\alpha 1}} \cdot i_{1,q} - \frac{MR_2}{L_{\alpha 1}L_2} \cdot i_{2,q} - \frac{1}{L_{\alpha 1}} \cdot v_{C1,q} - \frac{M}{L_{\alpha 1}L_2} \cdot v_{C2,q} \\ &+ \frac{1}{L_{\alpha 1}} \cdot v_{1,q} - \frac{M}{L_{\alpha 1}L_2} \cdot \frac{i_{2,q}}{\sqrt{i_{2,d}^2 + i_{2,q}^2}} \cdot \frac{4}{\pi} \cdot V_{dc,out}\end{aligned} \tag{4.23}$$

$$\begin{aligned}\frac{di_{2,d}}{dt} =&\omega \cdot i_{2,q} - \frac{MR_1}{L_{\alpha 2}L_1} \cdot i_{1,d} - \frac{R_2}{L_{\alpha 2}} \cdot i_{2,d} - \frac{M}{L_{\alpha 2}L_1} \cdot v_{C1,d} - \frac{1}{L_{\alpha 2}} \cdot v_{C2,d} \\ &+ \frac{M}{L_{\alpha 2}L_1} \cdot v_{1,d} - \frac{1}{L_{\alpha 2}} \cdot \frac{i_{2,d}}{\sqrt{i_{2,d}^2 + i_{2,q}^2}} \cdot \frac{4}{\pi} \cdot V_{dc,out}\end{aligned} \tag{4.24}$$

$$\begin{aligned}\frac{di_{2,q}}{dt} =&-\omega \cdot i_{2,d} - \frac{MR_1}{L_{\alpha 2}L_1} \cdot i_{1,q} - \frac{R_2}{L_{\alpha 2}} \cdot i_{2,q} - \frac{M}{L_{\alpha 2}L_1} \cdot v_{C1,q} - \frac{1}{L_{\alpha 2}} \cdot v_{C2,q} \\ &+ \frac{M}{L_{\alpha 2}L_1} \cdot v_{1,q} - \frac{1}{L_{\alpha 2}} \cdot \frac{i_{2,q}}{\sqrt{i_{2,d}^2 + i_{2,q}^2}} \cdot \frac{4}{\pi} \cdot V_{dc,out}\end{aligned} \tag{4.25}$$

$$\frac{dv_{C1,d}}{dt} = \omega \cdot v_{C1,q} + \frac{1}{C_1} \cdot i_{1,d} \tag{4.26}$$

$$\frac{dv_{C1,q}}{dt} = -\omega \cdot v_{C1,d} + \frac{1}{C_1} \cdot i_{1,q} \tag{4.27}$$

$$\frac{dv_{C2,d}}{dt} = \omega \cdot v_{C2,q} + \frac{1}{C_2} \cdot i_{2,d} \tag{4.28}$$

$$\frac{dv_{C2,q}}{dt} = -\omega \cdot v_{C2,d} + \frac{1}{C_2} \cdot i_{2,q} \tag{4.29}$$

This model can be used for simulating and analyzing the IPT-system and accurately capture the envelope of the fundamental frequency currents and voltages at any possible operating point, as long as the first harmonic approximation is valid and as long as the operating frequency ω is constant or slowly varying[26].

4.2 Steady-state solutions in resonant operation

In order to perform eigenvalue analysis and to study stabilization properties like controllability and observability, it is necessary to linearize the model at an operating point defined by $\boldsymbol{f}(\boldsymbol{x}, \boldsymbol{u}) = 0$.

The reference frame of the dq-model can be chosen arbitrary, and for convenience it is defined to be synchronized with the peak amplitude of v_1. Therefore, the operating q-axis voltage component at the sending side is zero, $v_{1,q,0} = 0$, and the operating d-axis voltage component is equal to the peak amplitude of v_1, $v_{1,d,0} = V_{1,0}$[18].

Solving the equation $\boldsymbol{f}(\boldsymbol{x}, \boldsymbol{u}) = 0$ results in the following steady-state values for the dq-current components:

$$i_{1,d,0} = \frac{V_{1,0} \cdot R_2 + \dfrac{4}{\pi} \cdot V_{dc,out,0} \cdot \omega_0 \cdot M}{R_1 \cdot R_2 + \omega_0^2 \cdot M^2} \approx \frac{4}{\pi} \cdot \frac{V_{dc,out,0}}{\omega_0 \cdot M} \tag{4.30a}$$

$$i_{1,q,0} = 0 \tag{4.30b}$$

$$i_{2,d,0} = 0 \tag{4.30c}$$

$$i_{2,q,0} = \frac{\omega_0 \cdot M \cdot V_{1,0} - R_1 \cdot \dfrac{4}{\pi} \cdot V_{dc,out,0}}{R_1 \cdot R_2 + \omega_0^2 \cdot M^2} \approx \frac{V_{1,0}}{\omega_0 \cdot M} \tag{4.30d}$$

Here, the approximations are made by assuming an ideal lossless case, $R_1 = R_2 = 0$.

Inserting these components into the steady-state equations of 4.26-4.29, i.e. with zero derivative, the steady-state solutions for the voltages are found to be:

$$v_{C1,d,0} = \frac{1}{C_1 \cdot \omega_0} \cdot i_{1,q,0} = 0 \tag{4.31a}$$

$$\begin{aligned} v_{C1,q,0} &= -\frac{1}{C_1 \cdot \omega_0} \cdot i_{1,d,0} \\ &= -\frac{V_{1,0} \cdot R_2 + \frac{4}{\pi} \cdot V_{dc,out,0} \cdot \omega_0 \cdot M}{C_1 \cdot \omega_0 \cdot (R_1 \cdot R_2 + \omega_0^2 \cdot M^2)} \approx -\frac{4}{\pi} \cdot \frac{V_{dc,out,0}}{C_1 \cdot \omega_0^2 \cdot M} \end{aligned} \tag{4.31b}$$

$$\begin{aligned} v_{C2,d,0} &= \frac{1}{C_2 \cdot \omega_0} \cdot i_{2,q,0} \\ &= \frac{\omega_0 \cdot M \cdot V_{1,0} - R_1 \cdot \frac{4}{\pi} \cdot V_{dc,out,0}}{C_2 \cdot \omega_0 \cdot (R_1 \cdot R_2 + \omega_0^2 \cdot M^2)} \approx \frac{V_{1,0}}{C_2 \cdot \omega_0^2 \cdot M} \end{aligned} \tag{4.31c}$$

$$v_{C2,q,0} = -\frac{1}{C_2 \cdot \omega_0} \cdot i_{2,d,0} = 0 \tag{4.31d}$$

Where again the approximations are made by assuming an ideal lossless case. These steady-state solutions are only valid when assuming a perfectly tuned system with a single resonant frequency $\omega = \omega_0 = \frac{1}{\sqrt{L_1 C_1}} = \frac{1}{\sqrt{L_2 C_2}}$. The general steady-state solutions, i.e., solutions valid in off-resonant operation and with potentially different resonance frequencies at either side of the link are amazingly complicated and not reported here.

4.3 Small-signal model with constant voltage load

The linearized model describing the small-signal dynamics can be written in compact form as:

$$\Delta \dot{\boldsymbol{x}} = \boldsymbol{A}(\boldsymbol{x}^p, \boldsymbol{u}^p) \cdot \Delta \boldsymbol{x} + \boldsymbol{B}(\boldsymbol{x}^p, \boldsymbol{u}^p) \cdot \Delta \boldsymbol{u} \tag{4.32}$$

where the matrices can be found according to:

$$\boldsymbol{A}(\boldsymbol{x}^p, \boldsymbol{u}^p) = \left.\frac{\partial f_i}{\partial \boldsymbol{x}}\right|_{\boldsymbol{x}^p, \boldsymbol{u}^p} \qquad \boldsymbol{B}(\boldsymbol{x}^p, \boldsymbol{u}^p) = \left.\frac{\partial f_i}{\partial \boldsymbol{u}}\right|_{\boldsymbol{x}^p, \boldsymbol{u}^p} \tag{4.33}$$

Computing the elements of these matrices is quite uncomplicated, except some troublesome entries:

$$\begin{aligned} A_{1,3} = \left.\frac{\partial f_1}{\partial i_{2,d}}\right|_{\substack{\boldsymbol{x}=\boldsymbol{x}^p\\ \boldsymbol{u}=\boldsymbol{u}^p}} &= -\frac{MR_2}{L_{\alpha 1}L_2} - \frac{4}{\pi}\frac{MV_{dc,out,0}}{L_{\alpha 1}L_2}\frac{i_{2,q,0}^2}{(i_{2,d,0}^2 + i_{2,q,0}^2)^{3/2}} \\ &\overset{res}{=} -\frac{MR_2}{L_{\alpha 1}L_2} - \frac{4}{\pi}\frac{MV_{dc,out,0}}{L_{\alpha 1}L_2}\frac{1}{|i_{2,q,0}|} \\ &\overset{res}{=} -\frac{MR_2}{L_{\alpha 1}L_2} - \frac{\frac{4}{\pi}V_{dc,out,0}(R_1R_2 + \omega_0^2M^2)M}{L_{\alpha 1}L_2|\omega_0 MV_{1,0} - R_1\frac{4}{\pi}V_{dc,out,0}|} \approx \frac{\frac{4}{\pi}V_{dc,out,0}\cdot\omega_0 M^2}{L_{\alpha 1}L_2V_{1,0}} \end{aligned} \tag{4.34}$$

$$A_{1,4} = \left.\frac{\partial f_1}{\partial i_{2,q}}\right|_{\substack{\boldsymbol{x}=\boldsymbol{x}^p\\ \boldsymbol{u}=\boldsymbol{u}^p}} = -\frac{4}{\pi}\frac{MV_{dc,out,0}}{L_{\alpha 1}L_2}\frac{i_{2,d,0}\cdot i_{2,q,0}}{(i_{2,d,0}^2 + i_{2,q,0}^2)^{3/2}} \overset{res}{=} 0 \tag{4.35}$$

$$A_{2,3} = \left.\frac{\partial f_2}{\partial i_{2,d}}\right|_{\substack{\boldsymbol{x}=\boldsymbol{x}^p\\ \boldsymbol{u}=\boldsymbol{u}^p}} = -\frac{4}{\pi}\frac{MV_{dc,out,0}}{L_{\alpha 1}L_2}\frac{i_{2,d,0}\cdot i_{2,q,0}}{(i_{2,d,0}^2 + i_{2,q,0}^2)^{3/2}} \overset{res}{=} 0 \tag{4.36}$$

$$\begin{aligned} A_{2,4} = \left.\frac{\partial f_2}{\partial i_{2,q}}\right|_{\substack{\boldsymbol{x}=\boldsymbol{x}^p\\ \boldsymbol{u}=\boldsymbol{u}^p}} &= -\frac{MR_2}{L_{\alpha 1}L_2} - \frac{4}{\pi}\frac{MV_{dc,out,0}}{L_{\alpha 1}L_2}\frac{i_{2,d,0}^2}{(i_{2,d,0}^2 + i_{2,q,0}^2)^{3/2}} \\ &\overset{res}{=} \frac{MR_2}{L_{\alpha 1}L_2} \approx 0 \end{aligned} \tag{4.37}$$

$$\begin{aligned} A_{3,3} = \left.\frac{\partial f_3}{\partial i_{2,d}}\right|_{\substack{\boldsymbol{x}=\boldsymbol{x}^p\\ \boldsymbol{u}=\boldsymbol{u}^p}} &= -\frac{R_2}{L_{\alpha 2}} - \frac{4}{\pi}\frac{V_{dc,out,0}}{L_{\alpha 2}}\frac{i_{2,q,0}^2}{(i_{2,d,0}^2 + i_{2,q,0}^2)^{3/2}} \\ &\overset{res}{=} -\frac{R_2}{L_{\alpha 2}} - \frac{4}{\pi}\frac{V_{dc,out,0}}{L_{\alpha 2}}\frac{1}{|i_{2,q,0}|} \\ &\overset{res}{=} -\frac{R_2}{L_{\alpha 2}} - \frac{\frac{4}{\pi}V_{dc,out,0}(R_1R_2 + \omega_0^2M^2)}{L_{\alpha 2}|\omega_0 MV_{1,0} - R_1\frac{4}{\pi}V_{dc,out,0}|} \approx -\frac{\frac{4}{\pi}V_{dc,out,0}\cdot\omega_0 M}{L_{\alpha 2}V_{1,0}} \end{aligned} \tag{4.38}$$

$$A_{3,4} = \left.\frac{\partial f_3}{\partial i_{2,q}}\right|_{\substack{\boldsymbol{x}=\boldsymbol{x}^p \\ \boldsymbol{u}=\boldsymbol{u}^p}} = \omega_0 - \frac{4}{\pi}\frac{V_{dc,out,0}}{L_{\alpha 2}}\frac{i_{2,d,0}\cdot i_{2,q,0}}{(i_{2,d,0}^2 + i_{2,q,0}^2)^{3/2}} \overset{res}{=} \omega_0 \tag{4.39}$$

$$A_{4,3} = \left.\frac{\partial f_4}{\partial i_{2,d}}\right|_{\substack{\boldsymbol{x}=\boldsymbol{x}^p \\ \boldsymbol{u}=\boldsymbol{u}^p}} = -\omega_0 - \frac{4}{\pi}\frac{V_{dc,out,0}}{L_{\alpha 2}}\frac{i_{2,d,0}\cdot i_{2,q,0}}{(i_{2,d,0}^2 + i_{2,q,0}^2)^{3/2}} \overset{res}{=} -\omega_0 \tag{4.40}$$

$$\begin{aligned} A_{4,4} = \left.\frac{\partial f_4}{\partial i_{2,q}}\right|_{\substack{\boldsymbol{x}=\boldsymbol{x}^p \\ \boldsymbol{u}=\boldsymbol{u}^p}} &= -\frac{R_2}{L_{\alpha 2}} - \frac{4}{\pi}\frac{V_{dc,out,0}}{L_{\alpha 2}}\frac{i_{2,d,0}^2}{(i_{2,d,0}^2 + i_{2,q,0}^2)^{3/2}} \\ &\overset{res}{=} -\frac{R_2}{L_{\alpha 2}} \approx 0 \end{aligned} \tag{4.41}$$

$$B_{1,4} = \left.\frac{\partial f_1}{\partial V_{dc,out}}\right|_{\substack{\boldsymbol{x}=\boldsymbol{x}^p \\ \boldsymbol{u}=\boldsymbol{u}^p}} = -\frac{4}{\pi}\frac{M}{L_{\alpha 1}L_2}\frac{i_{2,d,0}}{\sqrt{i_{2,d,0}^2 + i_{2,d,0}^2}} \overset{res}{=} 0 \tag{4.42}$$

$$B_{2,4} = \left.\frac{\partial f_2}{\partial V_{dc,out}}\right|_{\substack{\boldsymbol{x}=\boldsymbol{x}^p \\ \boldsymbol{u}=\boldsymbol{u}^p}} = -\frac{4}{\pi}\frac{M}{L_{\alpha 1}L_2}\frac{i_{2,q,0}}{\sqrt{i_{2,d,0}^2 + i_{2,d,0}^2}} \overset{res}{=} -\frac{4}{\pi}\frac{M}{L_{\alpha 1}L_2} sgn(i_{2,q,0}) \tag{4.43}$$

$$B_{3,4} = \left.\frac{\partial f_3}{\partial V_{dc,out}}\right|_{\substack{\boldsymbol{x}=\boldsymbol{x}^p \\ \boldsymbol{u}=\boldsymbol{u}^p}} = -\frac{4}{\pi}\frac{1}{L_{\alpha 2}}\frac{i_{2,d,0}}{\sqrt{i_{2,d,0}^2 + i_{2,q,0}^2}} \overset{res}{=} 0 \tag{4.44}$$

$$B_{4,4} = \left.\frac{\partial f_4}{\partial V_{dc,out}}\right|_{\substack{\boldsymbol{x}=\boldsymbol{x}^p \\ \boldsymbol{u}=\boldsymbol{u}^p}} = -\frac{4}{\pi}\frac{1}{L_{\alpha 2}}\frac{i_{2,q,0}}{\sqrt{i_{2,d,0}^2 + i_{2,q,0}^2}} \overset{res}{=} -\frac{4}{\pi}\frac{1}{L_{\alpha 2}} sgn(i_{2,q,0}) \tag{4.45}$$

Here, the ”res”-notation above the equality sign indicates that the following calculations are done with the assumption of a perfectly tuned system and operation in resonance, $\omega = \omega_0 = \frac{1}{\sqrt{L_1 C_1}} = \frac{1}{\sqrt{L_2 C_2}}$, and the approximations are made by assuming an ideal lossless resonant case. The sgn-notation denotes the $signum$ function. All other elements can be easily found by straightforward derivation. However, these calculations are not shown here for brevity. By inserting the obtained results in Equation 4.33, the resulting $\boldsymbol{A}$- and $\boldsymbol{B}$-matrices are found to be:

$$\boldsymbol{A} = \begin{pmatrix} -\frac{R_1}{L_{\alpha 1}} & \omega_0 & A_{1,3} & A_{1,4} & -\frac{1}{L_{\alpha 1}} & 0 & -\frac{M}{L_{\alpha 1} L_2} & 0 \\ -\omega_0 & -\frac{R_1}{L_{\alpha 1}} & A_{2,3} & A_{2,4} & 0 & -\frac{1}{L_{\alpha 1}} & 0 & -\frac{M}{L_{\alpha 1} L_2} \\ -\frac{M R_1}{L_{\alpha 2} L_1} & 0 & A_{3,3} & A_{3,4} & -\frac{M}{L_{\alpha 2} L_1} & 0 & -\frac{1}{L_{\alpha 2}} & 0 \\ 0 & -\frac{M R_1}{L_{\alpha 2} L_1} & A_{4,3} & A_{4,4} & 0 & -\frac{M}{L_{\alpha 2} L_1} & 0 & -\frac{1}{L_{\alpha 2}} \\ \frac{1}{C_1} & 0 & 0 & 0 & 0 & \omega_0 & 0 & 0 \\ 0 & \frac{1}{C_1} & 0 & 0 & -\omega_0 & 0 & 0 & 0 \\ 0 & 0 & \frac{1}{C_2} & 0 & 0 & 0 & 0 & \omega_0 \\ 0 & 0 & 0 & \frac{1}{C_2} & 0 & 0 & -\omega_0 & 0 \end{pmatrix} \tag{4.46}$$

$$\boldsymbol{B} = \begin{pmatrix} \frac{1}{L_{\alpha 1}} & 0 & i_{1,q,0} & B_{1,4} \\ 0 & \frac{1}{L_{\alpha 1}} & -i_{1,d,0} & B_{2,4} \\ \frac{M}{L_{\alpha 2} L_1} & 0 & i_{2,q,0} & B_{3,4} \\ 0 & \frac{M}{L_{\alpha 2} L_1} & -i_{2,d,0} & B_{4,4} \\ 0 & 0 & v_{C1,q,0} & 0 \\ 0 & 0 & -v_{C1,d,0} & 0 \\ 0 & 0 & v_{C2,q,0} & 0 \\ 0 & 0 & -v_{C2,d,0} & 0 \end{pmatrix} \tag{4.47}$$

Where $A_{1,3}$, $A_{1,4}$, $A_{2,3}$, $A_{2,3}$, $A_{3,3}$, $A_{3,4}$, $A_{4,3}$, $A_{4,4}$, $B_{1,4}$, $B_{2,4}$, $B_{3,4}$, $B_{4,4}$ are the results obtained above. Considering operation in resonance, the analytic expressions for the steady-state solutions and matrix elements are used. Assuming an ideal lossless resonant case, the approximations are used, and the value of the matrix elements $A_{1,1}$, $A_{2,2}$, $A_{2,4}$, $A_{3,1}$ are, in addition, all zero due to the assumption negligible losses.

Thus, the complete linearized model is described in state-space representation as:

$$\Delta\dot{\boldsymbol{x}} = \boldsymbol{A}(\boldsymbol{x}^p, \boldsymbol{u}^p) \cdot \Delta\boldsymbol{x} + \boldsymbol{B}(\boldsymbol{x}^p, \boldsymbol{u}^p) \cdot \Delta\boldsymbol{u} \tag{4.48}$$

where the matrices $\boldsymbol{A}$ and $\boldsymbol{B}$ are reported in equation Equation 4.46 and Equation 4.47, respectively, and the state vector $\Delta\boldsymbol{x}$ and input vector $\Delta\boldsymbol{u}$ are defined as follows:

$$\Delta\boldsymbol{x} = \begin{bmatrix} \Delta i_{1,d} & \Delta i_{1,q} & \Delta i_{2,d} & \Delta i_{2,q} & \Delta v_{C1,d} & \Delta v_{C1,q} & \Delta v_{C2,d} & \Delta v_{C2,q} \end{bmatrix}^T \tag{4.49}$$

$$\Delta\boldsymbol{u} = \begin{bmatrix} \Delta v_{1,d} & \Delta v_{1,q} & \Delta\omega & \Delta V_{dc,out} \end{bmatrix}^T \tag{4.50}$$

where $\Delta\boldsymbol{x} = \boldsymbol{x} - \boldsymbol{x}^p$ and $\Delta\boldsymbol{u} = \boldsymbol{u} - \boldsymbol{u}^p$. $\boldsymbol{x}^p$ is the steady-state solution corresponding to the operating input $\boldsymbol{u}^p$.

4.4 Small-signal model with constant resistive load

Modeling the load as a CRL would alter the system. In this case, the the receiving side voltage v_2 in Figure 2.3 would be determined by the equivalent resistance R_{eq} and the receiving side current i_2. Thus, in the derivation procedure of the dq-model, the following simplification is applied:

$$\frac{1}{\sqrt{i_{2,d}^2 + i_{2,q}^2}} \cdot \frac{4}{\pi} \cdot V_{dc,out} = R_{eq} \tag{4.51}$$

Similar as in the case with CVL, applying the above substitution and solving the equation $\boldsymbol{f}(\boldsymbol{x}, \boldsymbol{u}) = 0$, results in the following steady-state values for the dq-currents assuming resonant operation:

$$i_{1,d,0} = \frac{V_{1,0} \cdot (R_2 + R_{eq})}{R_1 \cdot (R_2 + R_{eq}) + \omega_0^2 \cdot M^2} \approx \frac{V_{1,0} \cdot R_{eq}}{\omega_0^2 \cdot M^2} \tag{4.52a}$$

$$i_{1,q,0} = 0 \tag{4.52b}$$

$$i_{2,d,0} = 0 \tag{4.52c}$$

$$i_{2,q,0} = \frac{\omega_0 \cdot M \cdot V_{1,0}}{R_1 \cdot (R_2 + R_{eq}) + \omega_0^2 \cdot M^2} \approx \frac{V_{1,0}}{\omega_0 \cdot M} \tag{4.52d}$$

$$\tag{4.52e}$$

Moreover, inserting these expressions in the steady-state capacitor voltage equations results in:

$$v_{C1,d,0} = \frac{1}{C_1 \cdot \omega_0} \cdot i_{1,q,0} = 0 \tag{4.53a}$$

$$\begin{aligned} v_{C1,q,0} &= -\frac{1}{C_1 \cdot \omega_0} \cdot i_{1,d,0} \\ &= -\frac{V_{1,0} \cdot (R_2 + R_{eq})}{C_1 \cdot \omega_0 \cdot (R_1 \cdot (R_2 + R_{eq}) + \omega_0^2 \cdot M^2)} \approx -\frac{V_{1,0} \cdot R_{eq}}{C_1 \cdot \omega_0^3 \cdot M^2} \end{aligned} \tag{4.53b}$$

$$\begin{aligned} v_{C2,d,0} &= \frac{1}{C_2 \cdot \omega_0} \cdot i_{2,q,0} \\ &= \frac{\omega_0 \cdot M \cdot V_{1,0}}{C_2 \cdot \omega_0 \cdot (R_1 \cdot (R_2 + R_{eq}) + \omega_0^2 \cdot M^2)} \approx \frac{V_{1,0}}{C_2 \cdot \omega_0^2 \cdot M} \end{aligned} \tag{4.53c}$$

$$v_{C2,q,0} = -\frac{1}{C_2 \cdot \omega_0} \cdot i_{2,d,0} = 0 \tag{4.53d}$$

With these expressions, it is possible to derive a linearized model according to:

$$\Delta \dot{\boldsymbol{x}} = \boldsymbol{A_{CRL}}(\boldsymbol{x}^p, \boldsymbol{u}^p) \cdot \Delta \boldsymbol{x} + \boldsymbol{B_{CRL}}(\boldsymbol{x}^p, \boldsymbol{u}^p) \cdot \Delta \boldsymbol{u} \tag{4.54}$$

where the state and input matrices are defined as:

$$\boldsymbol{A_{CRL}}(\boldsymbol{x}^p, \boldsymbol{u}^p) = \left.\frac{\partial f_i}{\partial \boldsymbol{x}}\right|_{\boldsymbol{x}^p, \boldsymbol{u}^p} \qquad \boldsymbol{B_{CRL}}(\boldsymbol{x}^p, \boldsymbol{u}^p) = \left.\frac{\partial f_i}{\partial \boldsymbol{u}}\right|_{\boldsymbol{x}^p, \boldsymbol{u}^p} \tag{4.55}$$

Performing these calculations, the resulting matrices arise:

$$\boldsymbol{A_{CRL}} = \begin{pmatrix} -\frac{R_1}{L_{\alpha 1}} & \omega_0 & \frac{M(R_2+R_{eq})}{-L_{\alpha 1}L_2} & 0 & -\frac{1}{L_{\alpha 1}} & 0 & \frac{M}{L_{\alpha 1}L_2} & 0 \\ -\omega_0 & -\frac{R_1}{L_{\alpha 1}} & 0 & \frac{M(R_2+R_{eq})}{-L_{\alpha 1}L_2} & 0 & -\frac{1}{L_{\alpha 1}} & 0 & -\frac{M}{L_{\alpha 1}L_2} \\ -\frac{MR_1}{L_{\alpha 2}L_1} & 0 & \frac{R_2+R_{eq}}{-L_{\alpha 2}} & 0 & -\frac{M}{L_{\alpha 2}L_1} & 0 & -\frac{1}{L_{\alpha 2}} & 0 \\ 0 & -\frac{MR_1}{L_{\alpha 2}L_1} & 0 & \frac{R_2+R_{eq}}{-L_{\alpha 2}} & 0 & -\frac{M}{L_{\alpha 2}L_1} & 0 & -\frac{1}{L_{\alpha 2}} \\ \frac{1}{C_1} & 0 & 0 & 0 & 0 & \omega_0 & 0 & 0 \\ 0 & \frac{1}{C_1} & 0 & 0 & -\omega_0 & 0 & 0 & 0 \\ 0 & 0 & \frac{1}{C_2} & 0 & 0 & 0 & 0 & \omega_0 \\ 0 & 0 & 0 & \frac{1}{C_2} & 0 & 0 & -\omega_0 & 0 \end{pmatrix} \tag{4.56}$$

$$\boldsymbol{B_{CRL}} = \begin{pmatrix} \frac{1}{L_{\alpha 1}} & 0 & i_{1,q,0} \\ 0 & \frac{1}{L_{\alpha 1}} & -i_{1,d,0} \\ \frac{M}{L_{\alpha 2}L_1} & 0 & i_{2,q,0} \\ 0 & \frac{M}{L_{\alpha 2}L_1} & -i_{2,d,0} \\ 0 & 0 & v_{C1,q,0} \\ 0 & 0 & -v_{C1,d,0} \\ 0 & 0 & v_{C2,q,0} \\ 0 & 0 & -v_{C2,d,0} \end{pmatrix} \tag{4.57}$$

It can be seen that the only model nonlinearity affecting the $\boldsymbol{A}$-matrix, in this case, is the operating frequency of ω_0, which will change according to the operating point. The steady-state currents do not imply any changes of the state matrix in the case with CRL as opposed to CVL, only the input matrix is affected.

Thus the linearized model assuming a CRL is described in state-space representation as:

$$\Delta\dot{\boldsymbol{x}} = \boldsymbol{A_{CRL}}(\boldsymbol{x}^p, \boldsymbol{u}^p) \cdot \Delta\boldsymbol{x} + \boldsymbol{B_{CRL}}(\boldsymbol{x}^p, \boldsymbol{u}^p) \cdot \Delta\boldsymbol{u} \tag{4.58}$$

where the matrices $\boldsymbol{A}$ and $\boldsymbol{B}$ are reported in equation Equation 4.56 and Equation 4.57, respectively, and the state vector $\Delta\boldsymbol{x}$ and input vector $\Delta\boldsymbol{u}$ are as follows:

$$\Delta \boldsymbol{x} = \begin{bmatrix} \Delta i_{1,d} & \Delta i_{1,q} & \Delta i_{2,d} & \Delta i_{2,q} & \Delta v_{C1,d} & \Delta v_{C1,q} & \Delta v_{C2,d} & \Delta v_{C2,q} \end{bmatrix}^T \tag{4.59}$$

$$\Delta \boldsymbol{u} = \begin{bmatrix} \Delta v_{1,d} & \Delta v_{1,q} & \Delta \omega \end{bmatrix}^T \tag{4.60}$$

Again, $\Delta \boldsymbol{x} = \boldsymbol{x} - \boldsymbol{x}^p$ and $\Delta \boldsymbol{u} = \boldsymbol{u} - \boldsymbol{u}^p$. $\boldsymbol{x}^p$ are the steady-state solution corresponding to the operating input $\boldsymbol{u}^p$.

4.5 Chapter summary

In this chapter, the derivation procedure of a nonlinear state-space model expressed in dq-axis state variables, representing an SS-compensated IPT-system with CVL, has been explained, together with the required assumptions imposed in order to establish its range of validity. Moreover, the linearization method has been applied to the nonlinear representation, assuming both CRL and CVL, thus resulting in small-signal state-space models suitable for extensive analysis in the full range of intended operation.

Chapter 5

Model Verification

Both the nonlinear and linearized dq-model should be simulated in order to assess their validity. Therefore, the two state-space models have been implemented, as well as the circuit describing the IPT-system in Figure 2.3, in the MATLAB/Simulink/Simscape environment. The presented dq-model has been thoroughly processed in order to be able to linearize it at any feasible operating condition, allowing for various time-domain simulations to be performed. The developed Simulink diagrams are shown in Appendix C.

This chapter presents several simulations in numerous operating conditions, thus documenting the robustness and validity of the state-space models. All simulations are performed with a two-level square waveform as the input voltage, expect from the simulations which consider step changes in the operating frequency. For these simulations, a sinusoidal input is utilized.

5.1 Simulation in resonant operation

The models in this section have been simulated with the parameters displayed in Table 3.1. Figure 5.1b and Figure 5.1c illustrates the dynamic response of the current at the sending and receiving side when a sequence of step changes in the input voltages as shown in Figure 5.1a is applied.

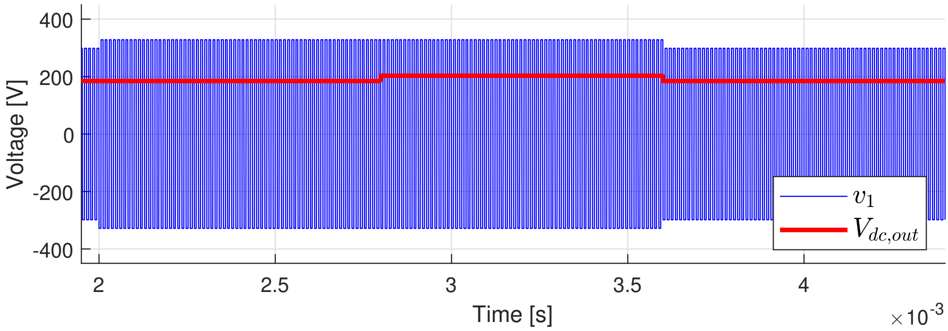

(a) Voltage at sending and receiving side.

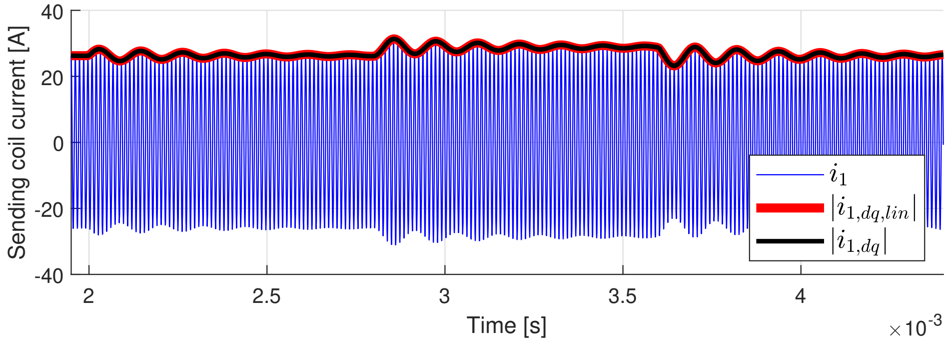

(b) Sending side current for the three simulated models.

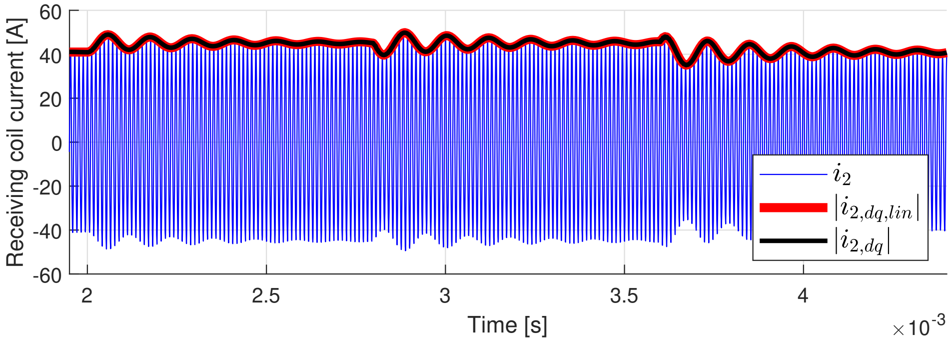

(c) Receiving side current for the three simulated models.

Figure 5.1: Model verification by simulation of the circuit, the linearized dq-model and the nonlinear dq-model in resonant operation.

In the simulations illustrated in Figure 5.1, the small-signal model has been obtained with a sending side voltage of $v_1 = V_{1,0}$ and a receiving side dc-voltage of $V_{dc,out} = V_{dc,out,0}$. For the presented simulations, the system is at first in steady-state condition at the operating point, until a step change of $v_1 = 1.1V_{1,0}$ is applied at t = 2 ms. At t = 2.8 ms, the system is brought further away from the operating point of the small-signal model with a step change of $V_{dc,out} = 1.1V_{dc,out,0}$. At t = 3.6 ms, both v_1 and $V_{dc,out}$ are stepped down to their nominal values and the system is brought back to the linearization point. This sequence is shown in Figure 5.1a.

The dynamic response of the sending- and receiving side currents is shown in Figure 5.1b and Figure 5.1c, respectively. It can be seen that the nonlinear dq-model is capturing the dynamic response to the input steps of the simulated IPT-model with good accuracy, both at the sending and receiving side. Furthermore, the small-signal model exhibits seemingly identical behavior as the nonlinear model, thus precisely capturing the current amplitude at both sides of the IPT-system as well.

An additional demonstration of the state-space models is presented in Figure 5.2, illustrating the dynamics of a step change in the operating frequency. For the presented simulation, the small-signal model is obtained with the same operating inputs as above. However, for this case, the system is first operating at steady-state with an operating frequency of 14 954 rad/s higher than the linearization frequency, before a step back to the linearization point is applied at t = 4 ms.

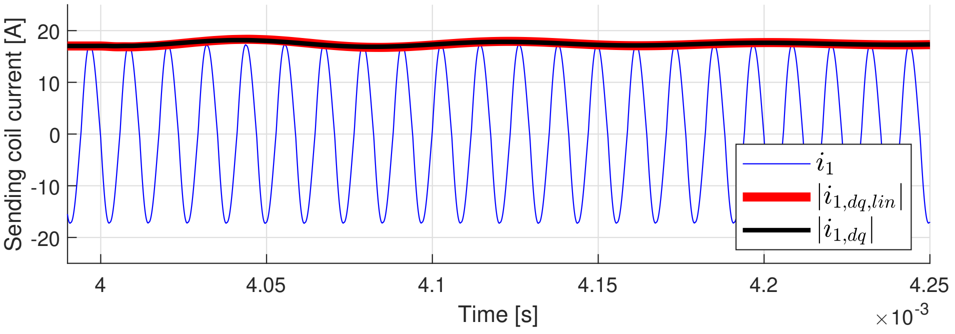

(a) Comparison of the sending side current for the three simulated models.

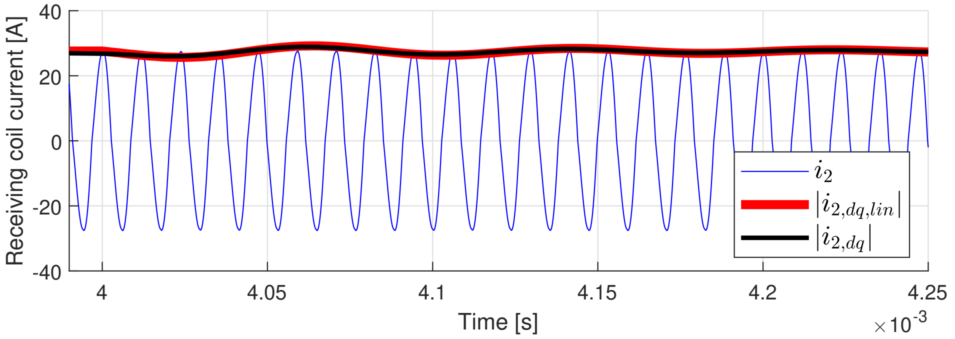

(b) Comparison of the receiving side current for the three simulated models.

Figure 5.2: Model verification by simulation of the circuit, the linearized dq-model and the nonlinear dq-model in resonant operation. Coupling factor $k = 1.5k_{nom}$

A slight deviation in the damping can be seen, indicating that the small-signal model is sensitive to perturbations in the operating frequency. This could also be seen from the frequency characteristics derived in Chapter 3, as a small change in the operating frequency could significantly influence the power flow. However, the oscillations and settling time of the current dynamics are still quite accurately captured. These above results show that the small-signal model is a good approximation when not operating far from the linearization point.

5.1.1 Variable load conditions

Since dynamic parameters such as load voltage and magnetic coupling may change during operation of the system, it is crucial that the developed state-space models represent the dynamic behavior of the actual IPT-system under those circumstances. Therefore, simulations with different load- and coupling conditions have been performed in order to provide additional verification of the state-space models.

In Figure 5.3 and Figure 5.4, the three models have been simulated with respectively low and high load conditions and illustrates how the system reacts to steps in the input voltage.

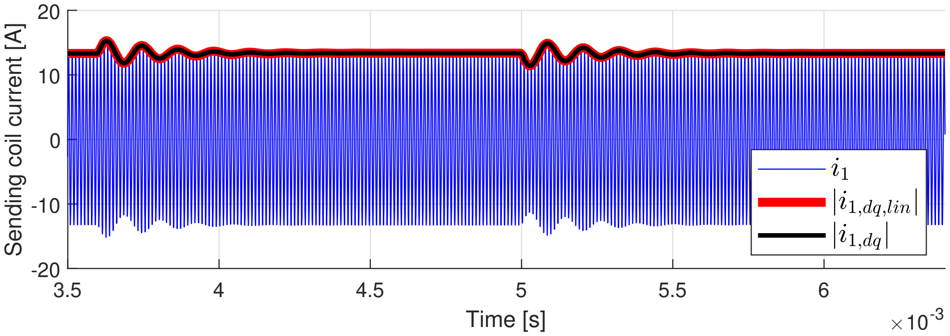

(a) Comparison of the sending side current for the three simulated models.

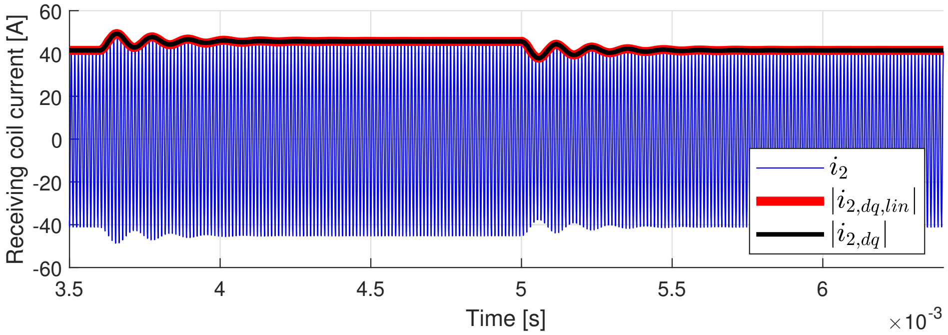

(b) Comparison of the receiving side current for the three simulated models.

Figure 5.3: Model verification by simulation of the circuit, the linearized dq-model and the nonlinear dq-model in resonant operation and with low load conditions, $V_2 = 0.5V_{2,nom}$.

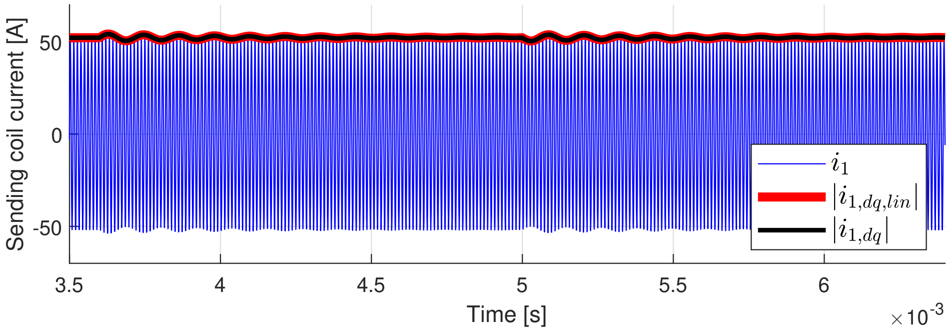

(a) Comparison of the sending side current for the three simulated models.

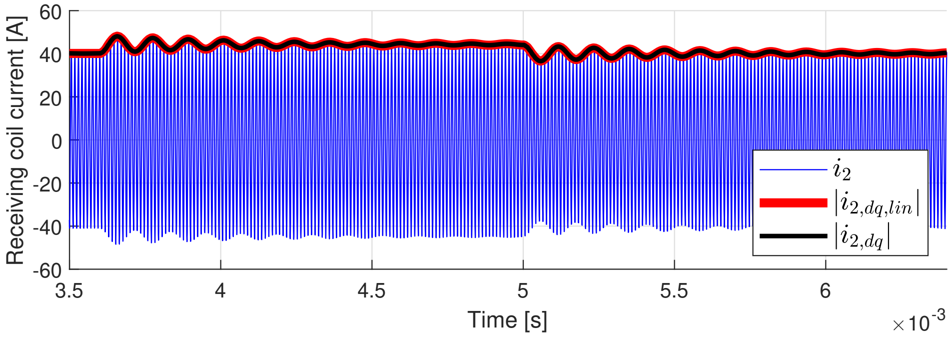

(b) Comparison of the receiving side current for the three simulated models.

Figure 5.4: Model verification by simulation of the circuit, the linearized dq-model and the nonlinear dq-model in resonant operation and with high load conditions, $V_2 = 2V_{2,nom}$.

For these simulations, a step change of $v_1 = 1.1V_{1,0}$, taking the system away from the operating point of the small-small signal model, is applied after t = 3.6 ms. When steady-state operation has been reached in the case with high load conditions, the system is brought back to the linearization point at t = 5 ms. As seen, the envelope of the current dynamics is accurately captured in both cases. The simulation sequence is equal for both conditions in order to more easily make a direct comparison of the oscillations and damping.

5.1.2 Variable coupling conditions

In Figure 5.5 and Figure 5.6, the three models have been simulated with respectively low and high coupling factor and shows the dynamic response on both sending and receiving side to a step in the input voltage.

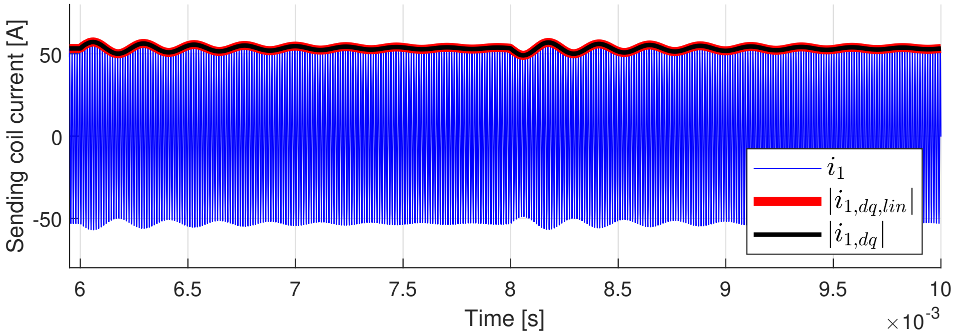

(a) Comparison of the sending side current for the three simulated models.

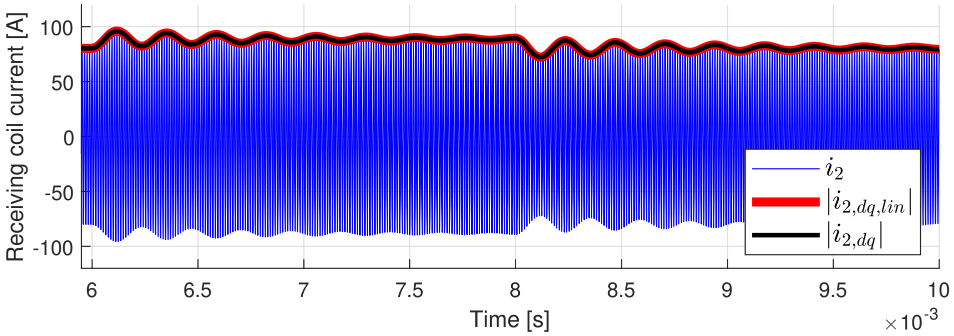

(b) Comparison of the receiving side current for the three simulated models.

Figure 5.5: Model verification by simulation of the circuit, the linearized dq-model and the nonlinear dq-model in resonant operation and with low coupling conditions, $k = 0.5k_{nom}$.

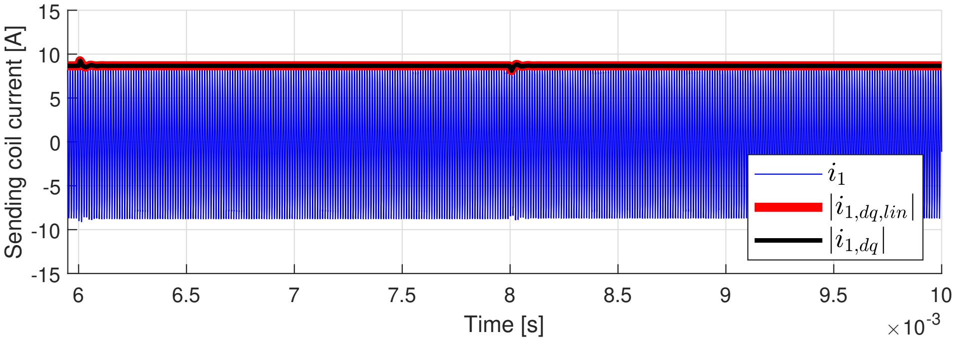

(a) Comparison of the sending side current for the three simulated models.

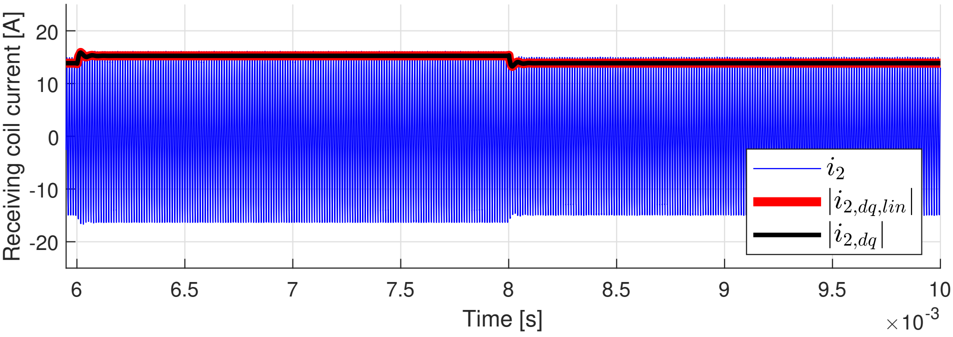

(b) Comparison of the receiving side current for the three simulated models.

Figure 5.6: Model verification by simulation of the circuit, the linearized dq-model and the nonlinear dq-model in resonant operation and with high coupling conditions, $k = 3k_{nom}$.

Quite similar as for above, a step change of $v_1 = 1.1V_{1,0}$ is applied after 6 ms, taking the models away from the linearization point of the small-signal model. After a steady-state operation has been reached at this point, emphasizing the case with low coupling factor, the models are brought back to the linearization point at t = 8 ms. As can be seen from Figure 5.5, the current amplitudes are accurately captured throughout the sequence of input steps in the case with a low coupling factor of $k = 0.5k_{nom}$. In the case with high coupling conditions, however, it can be observed that the nonlinear and linear state-space models are having some trouble of accurately capturing the envelope of the current waveforms. The oscillating modes and damping are well represented, but there is indeed a deviation from the current amplitude. This deviation arises due to the current waveforms are becoming increasingly distorted as the coupling factor increases, making the harmonic approximation less accurate, but still a reasonable assumption. The distorted current waveform is displayed in Figure 5.7.

It can also be observed that the system is significantly faster and more damped with high coupling conditions compared to low coupling conditions. The simulation sequence is equal for both cases here as well, making the comparison of the oscillations and damping easier.

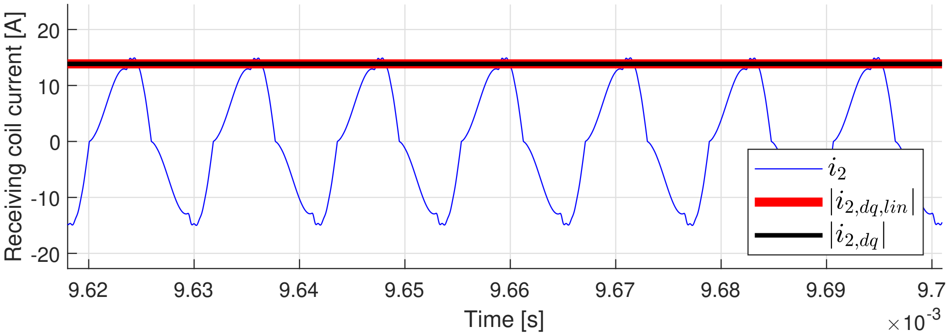

Figure 5.7: Enlarged view of current waveforms with coupling factor $k = 3k_{nom}$.

5.1.3 Comparison between constant voltage and constant resistive load

In order to evaluate the differences in the dynamic behavior of CVL and CRL, the resistive loaded model is also implemented in the MATLAB/Simulink/Simscape environment. In Figure 5.8, the response of the linearized CRL-model is plotted on top of the CVL-models.

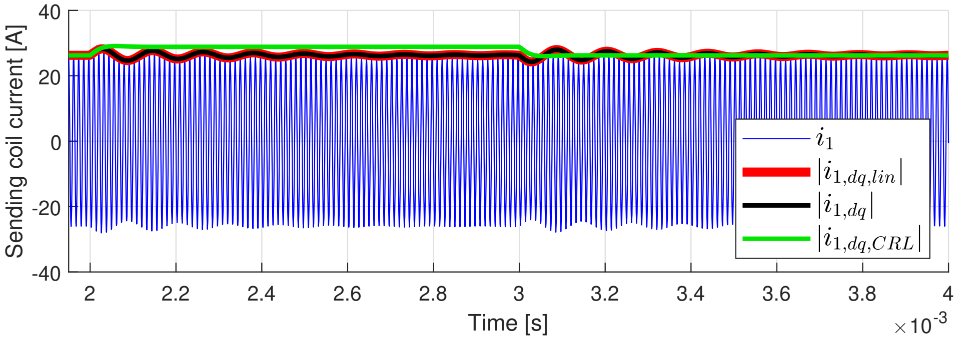

(a) Sending side currents.

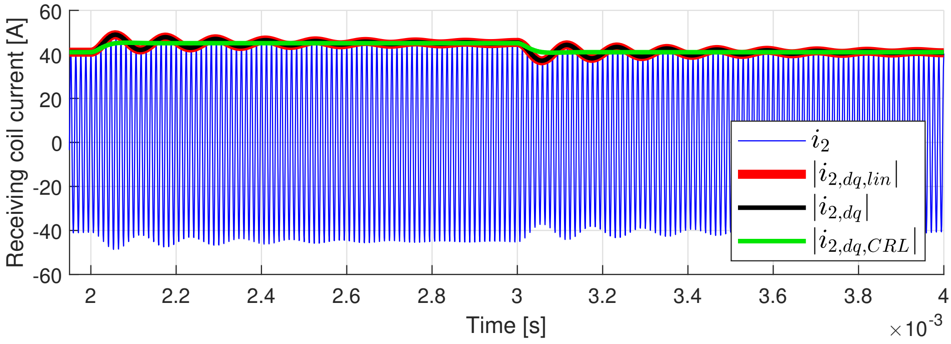

(b) Receiving side currents.

Figure 5.8: Comparison between CVL- and CRL-modeling.

The sequence of step changes is similar to the above simulations, i.e., a step change in the sending side voltage is applied after t = 2 ms and a step back to the linearization point is applied after t = 3 ms. As can be seen, the CRL-model is significantly faster and more damped than the CVL-model, indicating that such load modeling should not be used in design and analysis of IPT-system, as the system seems more damped and robust than it is. The deviation in the sending side current after the step change at t = 2 ms is due to the fundamental different behavior a CRL possess compared to a CVL. The response seen is confirmed correct in Figure 5.9, which shows the sending side current of the circuit model with CRL and the corresponding linearized model. This behavior could also be anticipated by comparing the steady-state solutions obtained in 3.5a and Equation 3.11a. In the CVL-case, the current in the sending side coil is mainly dependent on the voltage in the receiving coil, and vice verse, whereas in the CRL-case, the situation is quite different, thus causing the observed deviation.

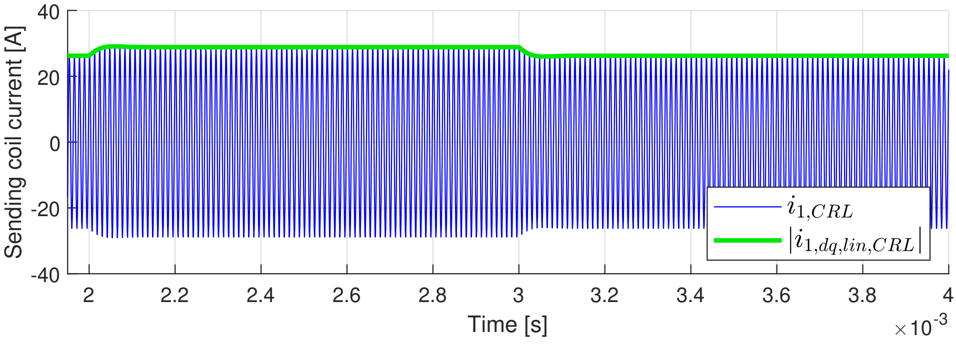

Figure 5.9: Model verification by simulation of the linearized model and circuit with CRL.

For the above simulations, the value of the CRL is equal to the equivalent steady-state resistance $R_{eq} = V_{2,0}/I_{2,0}$.

5.2 Simulation in off-resonant operation

In order to evaluate the validity of the results obtained when considering sub- and super-resonant operation, i.e., how the nonlinear dq-model and small-signal model behave in off-resonant conditions corresponding to 1 pu power transfer, time-domain simulations are also here performed, emphasizing operating points where the power transfer is kept at the reference. Figure 5.10 illustrates two points along the frequency trajectories for maintaining constant power for which the following simulations are performed, in both sub- and super-resonant frequency range.

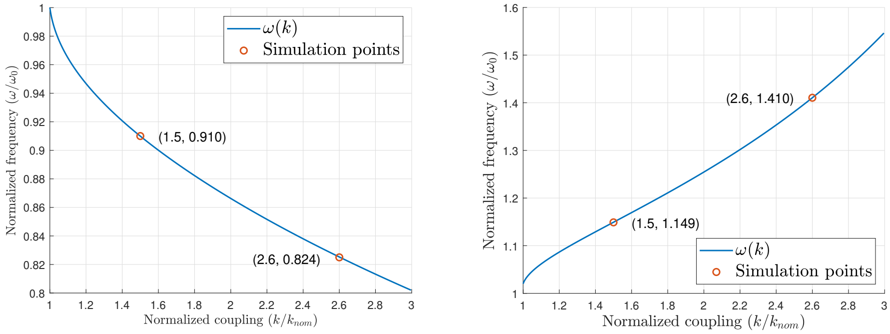

(a) Sub-resonant frequency control.

(b) Super-resonant frequency control.

Figure 5.10: Frequency trajectory for maintaining constant output power – marked with simulation points.

5.2.1 Sub-resonant operation

The simulation results for comparing the dynamic response of the models in sub-resonant operation are presented in Figure 5.11 and Figure 5.12.

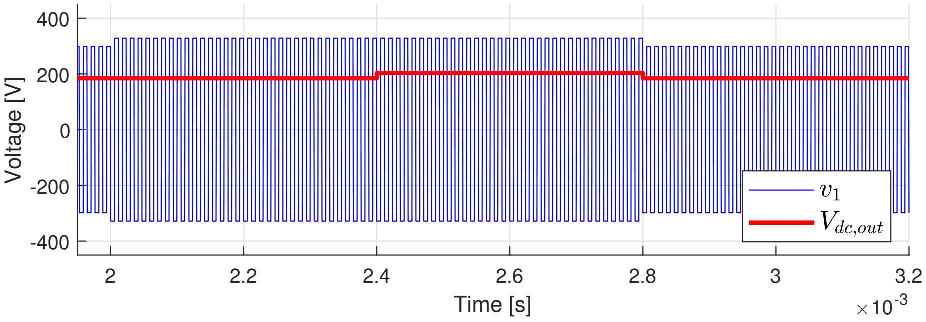

(a) Voltage at sending and receiving side.

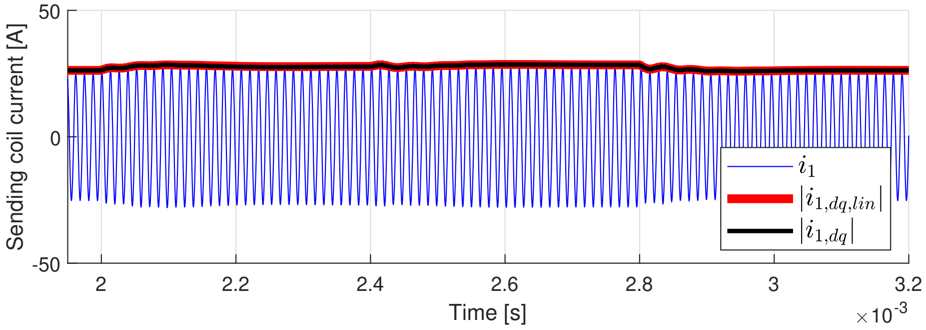

(b) Comparison of the sending side current for the three simulated models.

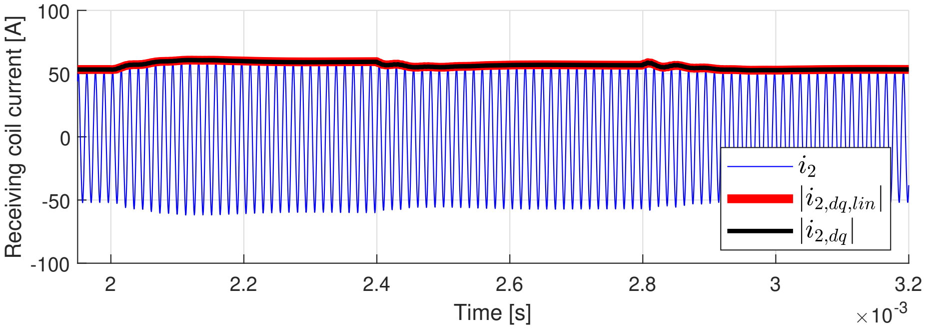

(c) Comparison of the receiving side current for the three simulated models.

Figure 5.11: Model verification by simulation of the circuit, the linearized dq-model and the non-linear dq-model in sub-resonant operation for maintaining constant output power. Operating frequency $\omega = 0.910\omega_0$, coupling factor $k = 1.5k_{nom}$, unbalance factor $x_u = 0.98$, detuning factor $x_c = 1.03$.

Here, the operating point of the small-signal model has been obtained with an unbalance factor of $x_u = 0.98$, detuning factor $x_c = 1.03$, operating frequency $\omega = 0.910\omega_0$ and a coupling coefficient of $k = 1.5k_{nom}$. Similar to the case with resonant operation, a step change in the sending side voltage of $v_1 = 1.1V_{1,0}$ is applied at t = 2 ms, and when steady-state operation is achieved at this point, a step change in the load voltage of $V_{dc,out} = 1.1V_{dc,out,0}$ is applied at 2.4 ms. When steady-state condition again is reached with these input voltages, a step back to the linearization point of the small-signal model is executed at t = 2.8 ms. This sequence of input steps is illustrated in Figure 5.11a.

The same sequence is repeated for another point corresponding to nominal power transfer, this time at high coupling factor $k = 2.6k_{nom}$ and correspondingly reduced operating frequency with $\omega = 0.824\omega_0$. Apart from that, similar conditions as for the simulations presented above. The dynamic response of the sending- and receiving side currents for this case is presented in Figure 5.12.

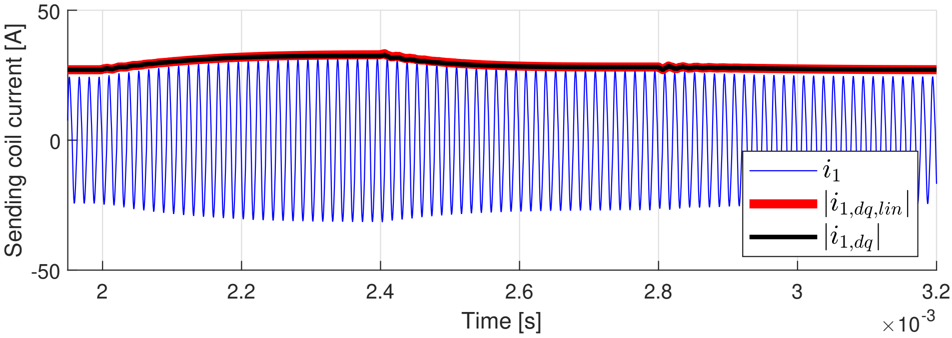

(a) Comparison of the sending side current for the three simulated models.

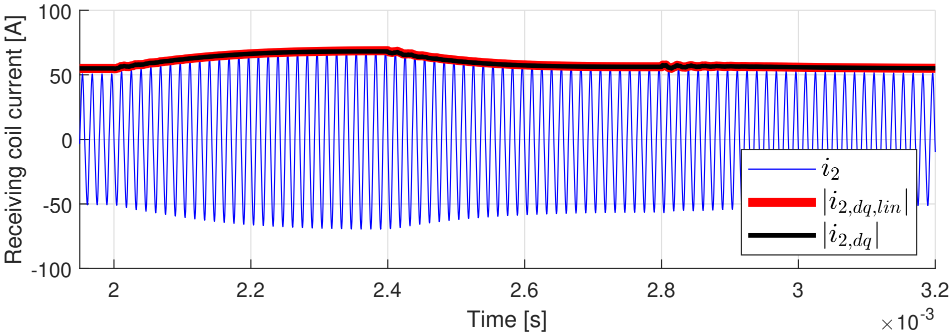

(b) Comparison of the receiving side current for the three simulated models.

Figure 5.12: Model verification by simulation of the circuit, the linearized dq-model and the non-linear dq-model in sub-resonant operation for maintaining constant output power. Operating frequency $\omega = 0.824\omega_0$, coupling factor $k = 2.6k_{nom}$, unbalance factor $x_u = 0.98$, detuning factor $x_c = 1.03$.

As can be seen, the nonlinear model, as well as the small-signal model, quite accurately captures the current amplitudes of the circuit model along the constant power frequency trajectory. However, some slight deviation of the current amplitudes can be observed, especially in the case of high coupling. This deviation is also due to the current waveforms becoming slightly distorted when the coupling conditions are high and with operation far from resonance. The distortion is shown in Figure 5.13 and it can be seen that the current waveform do not represent a perfect sine wave under these conditions, as the observed waveform is more V-shaped and edged. In any case, the oscillating modes are still accurately captured, and the settling- and rise time are virtually identical. Thus, the state-space models represent the dynamic behavior of the circuit very well.

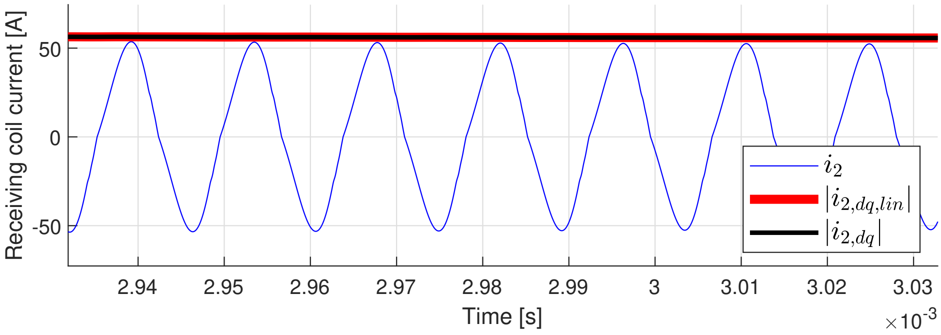

Figure 5.13: Enlarged view of current waveforms in simulation point $k = 2.6k_{nom}$, $\omega = 0.824\omega_0$.

5.2.2 Super-resonant operation

The simulation results for comparing the dynamic response of the models in super-resonant operation are presented in Figure 5.14 and Figure 5.15.

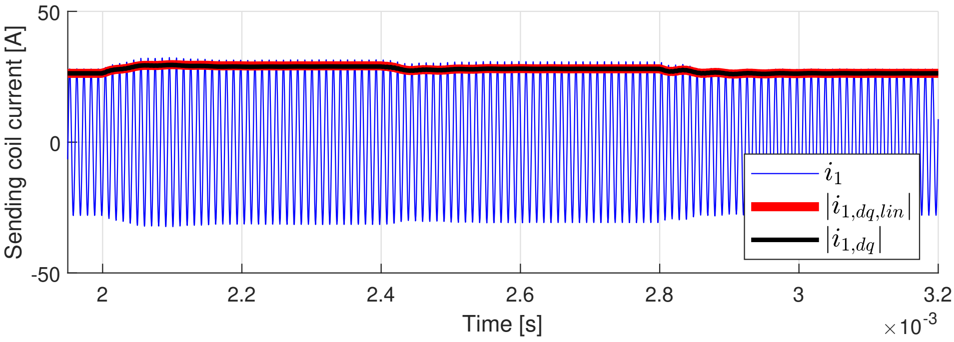

(a) Comparison of the sending side current for the three simulated models.

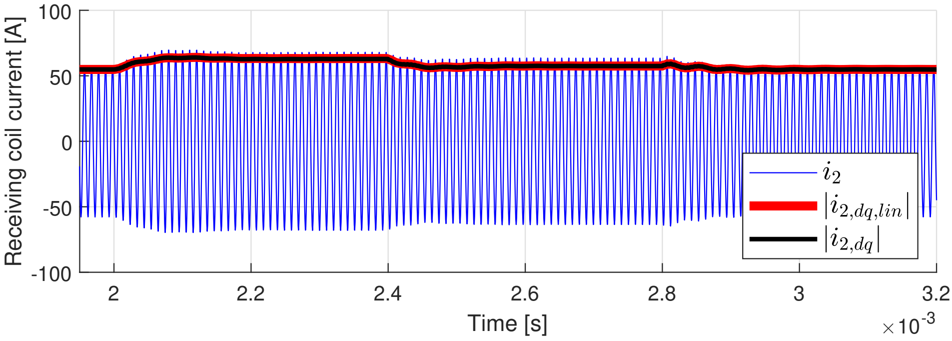

(b) Comparison of the receiving side current for the three simulated models.

Figure 5.14: Model verification by simulation of the circuit, the linearized dq-model and the non-linear dq-model in super-resonant operation for maintaining constant output power. Operating frequency $\omega = 1.149\omega_0$, coupling factor $k = 1.5k_{nom}$, unbalance factor $x_u = 0.95$, detuning factor $x_c = 0.97$.

For these simulation results, the small-signal model has been obtained with an unbalance factor of $x_u = 0.95$, detuning factor $x_c = 0.97$, operating frequency $\omega = 1.149\omega_0$ and a coupling coefficient of $k = 1.5k_{nom}$. The simulation sequence is identical as for the sub-resonant case.

Similar to before, the very same procedure is repeated for the case with high coupling, $k = 2.6k_{nom}$, and with correspondingly increased operating frequency, $\omega = 1.410\omega_0$. These simulation results are presented in Figure 5.15.

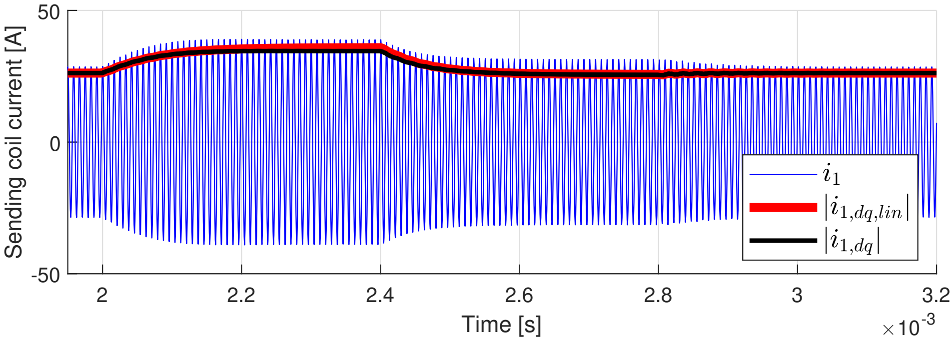

(a) Comparison of the sending side current for the three simulated models.

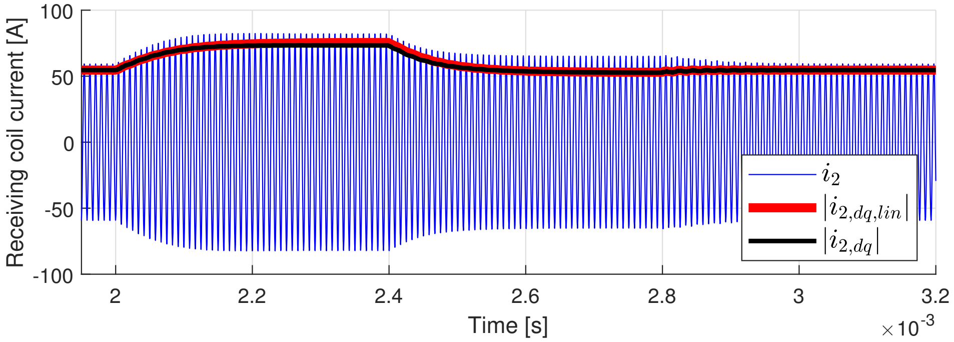

(b) Comparison of the receiving side current for the three simulated models.

Figure 5.15: Model verification by simulation of the circuit, the linearized dq-model and the non-linear dq-model in super-resonant operation for maintaining constant output power. Operating frequency $\omega = 1.410\omega_0$, coupling factor $k = 2.6k_{nom}$, unbalance factor $x_u = 0.95$, detuning factor $x_c = 0.97$.

As can be observed, the state-space models are having some trouble with capturing the current amplitudes of the circuit when operating in a super-resonant frequency range along the constant power frequency trajectory displayed in Figure 5.10b. In the case with the lowest coupling, illustrated in Figure 5.14, the frequency of the oscillations and damping are of similar behavior for the three models, indicating that the dynamics of the first harmonic frequency components are well represented. In the case with the highest coupling, however, as shown in Figure 5.15, in addition to the deviation of the current amplitudes, some odd performance regarding the dynamic behavior emerges as well. When the step back to the linearization point of the small-signal model is applied at t = 2.8 ms, it can be seen that there is a fundamentally different behavior of the circuit model compared to state-space models. The current amplitude of the circuit model decreases, whereas an increase can be observed for the state-space models. It can also be seen that the linearized model in this operating point is more sensitive to perturbations. When the first input step is applied at t = 2 ms, taking the system away from the linearization point, the small-signal model is not accurately following the nonlinear model. The system dynamics are, however, preserved.

These issues may arise due to the increasing harmonic distortion of the current waveforms when the magnetic coupling is high, combined with operating conditions far from resonance. Furthermore, nonlinearities of the system may be more exposed to these off-resonant conditions, making the system more sensitive to perturbations and changes.

5.3 Chapter summary

Comprehensive time-domain simulations are provided to determine the validity of the derived state-space models, emphasizing realistic operating conditions, as well as the intended range of operation under the proposed frequency control strategy. The models have been verified to accurately capture the envelopes of the fundamental frequency currents of the IPT-system in any sensible operating point. Some harmonic distortion is observed in the case with high coupling factor and strongly off-resonant operation, reducing the accuracy of the first harmonic approximation. The current dynamics are, however, captured with reasonable accuracy in almost any case. Furthermore, simulations comparing CVL and CRL modeling have demonstrated that the latter approach results in a much more damped response.

Chapter 6

Stability and Sensitivity Analysis

Eigenvalues and eigenvectors of the state matrix $\boldsymbol{A}$ in the linearized model can be utilized to investigate various stability and sensitivity properties describing the small-signal behavior of the system. This chapter presents several eigenvalue-based analyses such as eigenvalue trajectories in order to, e.g., assess the impact of varying operating conditions of the system, and to provide understanding in how the system dynamics change when maintaining constant power transfer under variable coupling conditions by changing the operating frequency. Furthermore, participation factors and parametric sensitivities are inspected to determine the system's sensitivity traits. Subsequently, controllability and observability Gramians are analyzed to ascertain important control properties. Some results an discussion regarding sensitivity analysis in resonant operation provided in this chapter are also presented in the specialization project.

The nominal parameters used in the analysis of the system are expressed in Table 3.1 and the eigenvalues of the $\boldsymbol{A}$-matrix configured with the nominal parameters are reported in Table 6.1.

Table 6.1: NOMINAL EIGENVALUES

	$eig(\boldsymbol{A})$
$\lambda_{1,2}$	$-2.2594 \cdot 10^4 \pm i1.1264 \cdot 10^6$
$\lambda_{3,4}$	$-1.5567 \cdot 10^4 \pm i1.0233 \cdot 10^6$
$\lambda_{5,6}$	$-2.9017 \cdot 10^3 \pm i5.3558 \cdot 10^4$
$\lambda_{7,8}$	$-3.5600 \cdot 10^4 \pm i4.2457 \cdot 10^4$

As can be noticed, mode 3, i.e., $\lambda_{5,6}$ has markedly lower real part than the others. It can, therefore, be expected that this particular mode will dominate the system dynamics.

6.1 Parametric sensitivity

As previously stated, parametric sensitivity analysis is a tool for investigating how the changeable parameters of a system affect the eigenvalues of the state matrix $\boldsymbol{A}$, and can be found according to the formula:

$$s_{i,k} = \frac{d\lambda_i}{d\rho_k} = \frac{\boldsymbol{r}_i^H \dfrac{\partial \boldsymbol{A}}{\partial \rho_k} \boldsymbol{l}_i}{\boldsymbol{r}_i^H \boldsymbol{l}_i} \tag{6.1}$$

In the following tables, parametric sensitivities to all eigenvalues of every parameter of the system is shown, in addition to sensitivities to the steady-state currents.

Table 6.2: SENSITIVITY TO PARAMETERS 1-4

$eig(\boldsymbol{A})$	R_1	R_2	L_1	L_2
$\lambda_{1,2}$	$-4072 \pm i152$	$-6477 \pm i2815$	$-4.2e7 \pm i2.8e7$	$2.2e8 \mp i1.4e8$
$\lambda_{3,4}$	$-1413 \pm i330$	$-6286 \mp i1822$	$-5.2e7 \mp i9.5e6$	$2.5e8 \pm 3.6e7$
$\lambda_{5,6}$	$-1107 \pm i652$	$-6134 \mp i187$	$9.5e6 \mp i8.8e6$	$-2.5e7 \pm 3.4e7$
$\lambda_{7,8}$	$-4465 \pm i195$	$-6772 \mp i6148$	$-1.1e8 \pm i1.0e8$	$5.1e8 \mp i4.5e8$

Table 6.3: SENSITIVITY TO PARAMETERS 5-7

$eig(\boldsymbol{A})$	C_1	C_2	k
$\lambda_{1,2}$	$2.1e16 \pm i5.2e16$	$-2.6e14 \mp i6.5e14$	$-1.0e5 \pm i5.5e4$
$\lambda_{3,4}$	$-2.1e16 \mp i6.5e16$	$2.6e14 \mp i8.4e14$	$-9.1e4 \mp i1.8e4$
$\lambda_{5,6}$	$-3.5e16 \pm i1.1e15$	$-4.2e14 \pm i3.0e14$	$1.5e4 \mp i6201$
$\lambda_{7,8}$	$3.4e16 \pm i1.6e16$	$4.2e14 \mp i1.7e14$	$-2.2e5 \pm i1.8e5$

Table 6.4: SENSITIVITY TO PARAMETERS 8-10

$eig(\boldsymbol{A})$	$V_{1,0}$	$V_{dc,out,0}$	ω_0
$\lambda_{1,2}$	$47.37 \mp i26.26$	$-97.52 \pm i54.06$	$-0.032 \pm i1.020$
$\lambda_{3,4}$	$49.07 \pm i9.420$	$-101.0 \mp i19.40$	$-0.034 \pm i0.995$
$\lambda_{5,6}$	$-6.676 \pm i4.827$	$13.74 \mp i9.937$	$-0.507 \pm i0.084$
$\lambda_{7,8}$	$105.9 \mp i91.82$	$-218.0 \pm i189.0$	$0.439 \mp i0.043$

Table 6.5: SENSITIVITY TO STEADY-STATE-SOLUTIONS

$eig(\boldsymbol{A})$	$i_{2,d,0}$	$i_{2,q,0}$
$\lambda_{1,2}$	$11.18 \pm i0.094$	$-429.9 \pm i238.3$
$\lambda_{3,4}$	$-12.72 \pm i0.113$	$-445.4 \mp i85.50$
$\lambda_{5,6}$	$8.669 \pm i247.6$	$60.59 \mp i43.81$
$\lambda_{7,8}$	$-7.130 \mp i320.7$	$-961.0 \pm i833.4$

For the above calculations, only resonant operation is considered. Indeed, parametric sensitivity to the eigenvalues can theoretically be found at any operating point. However, the complexity of the symbolic steady-state solutions of the dq-current components skyrockets when considering off-resonant operation, thus increasing the computational demand.

As can be observed from the presented tables, a small change in particularly the capacitor values significantly affects the eigenvalues, whereas a small change in the operating frequency have relatively low impact. This may seem to contradict the conclusion drawn from the simulations in Figure 5.2. However, the step change considered in the presented simulations is comparatively high, as the changes considered in the parametric sensitivity tables are infinitesimal.

6.2 Participation factors

As earlier described, the participation factor is a tool for analyzing the level of interaction between the states and the modes of a system. According to Table 6.1, the eigenvalues of the $\boldsymbol{A}$-matrix are all complex conjugate pairs. In order to take care of this issue, the first method has been adjusted to include the absolute value of the eigenvector entries. Four different participation factors have been investigated in the following:

$$p_{ki} = |l_k^i r_k^i| \tag{6.2}$$

Method II:

$$p_{ki} = \frac{(\Re\{l_k^i\})^2}{\Re\{\boldsymbol{l}^i\}(\Re\{\boldsymbol{l}^i\})^T} \tag{6.3}$$

Method III:

$$p_{ki} = \frac{|l_k^i|^2}{\sum_{j=1}^{n} |l_j^i|} \tag{6.4}$$

Method IV:

$$p_{ki} = 2\Re\{l_k^i r_k^i\}) \tag{6.5}$$

The respective results are shown in Table 6.6, 6.7, 6.8 and 6.9.

Table 6.6: PARTICIPATION FACTORS METHOD I

State	Mode 1	Mode 2	Mode 3	Mode 4
$i_{1,d}$	0.1323	0.1308	0.2660	0.0170
$i_{1,q}$	0.1334	0.1319	0.0202	0.3449
$i_{2,d}$	0.1322	0.1332	0.0217	0.3526
$i_{2,q}$	0.1321	0.1336	0.2595	0.0107
$v_{C1,d}$	0.1325	0.1310	0.0173	0.3441
$v_{C1,q}$	0.1332	0.1316	0.2633	0.0138
$v_{C2,d}$	0.1318	0.1332	0.2741	0.0282
$v_{C2,q}$	0.1323	0.1337	0.0195	0.3457

The critical mode of the system according to Table 6.1 is labeled as Mode 3. It can be observed that the states which participates most in the dominating mode according to this method are $i_{1,d}$, $i_{2,q}$, $v_{C1,q}$ and $v_{C2,d}$. The reason may be that $i_{1,d}$ and $i_{2,q}$ are the states that determine the steady-state power flow of the system, and that $v_{C1,q}$ and $v_{C2,d}$ are connected to $i_{1,d}$ and $i_{2,q}$ through the general capacitor voltage formula $v_c(s) = \frac{-j\omega}{C} i_c(s)$. That is, the voltage across the capacitor is phase shifted by 90 degrees compared to the capacitor current and it is therefore a connection between the q-axis capacitor voltage and d-axis current in both coils.

Mode 4 of this table is the pole-pair with the lowest real part, and it can be seen that the set of states which participates most in this mode is the complement of the set of states that participates most in the critical mode. These states have the least effect on the overall model response and system dynamics and their contribution to the dynamics will quickly vanish. Mode 1 and 2 are the most oscillating modes, i.e., the eigenvalue pairs with highest imaginary part in terms of absolute value, and all the states participate almost equally in these, which are probably describing high-frequency inductor-capacitor-oscillations.

Table 6.7: PARTICIPATION FACTORS METHOD II

State	Mode 1	Mode 2	Mode 3	Mode 4
$i_{1,d}$	0.6480	0.6899	0.9544	0.0356
$i_{1,q}$	0.1675	0.1202	0.1202	0.9596
$i_{2,d}$	0.1838	0.1893	0.0100	$1.3252 \cdot 10^{-4}$
$i_{2,q}$	$6.7051 \cdot 10^{-5}$	$1.7255 \cdot 10^{-5}$	$1.5038 \cdot 10^{-5}$	0.0045
$v_{C1,d}$	$1.8746 \cdot 10^{-5}$	$1.3158 \cdot 10^{-5}$	$4.0442 \cdot 10^{-6}$	$1.0868 \cdot 10^{-4}$
$v_{C1,q}$	$9.3431 \cdot 10^{-5}$	$6.3781 \cdot 10^{-5}$	$1.0673 \cdot 10^{-4}$	$4.1201 \cdot 10^{-6}$
$v_{C2,d}$	$2.9534 \cdot 10^{-7}$	$2.7875 \cdot 10^{-8}$	$8.5123 \cdot 10^{-8}$	$9.0091 \cdot 10^{-7}$
$v_{C2,q}$	$4.7722 \cdot 10^{-4}$	$3.4115 \cdot 10^{-4}$	$6.0590 \cdot 10^{-6}$	$8.6470 \cdot 10^{-8}$

Table 6.8: PARTICIPATION FACTORS METHOD III

State	Mode 1	Mode 2	Mode 3	Mode 4
$i_{1,d}$	0.4055	0.4033	0.7813	0.0272
$i_{1,q}$	0.4068	0.4041	0.0316	0.7804
$i_{2,d}$	0.0942	0.0963	0.0144	0.1906
$i_{2,q}$	0.0929	0.0958	0.1722	0.0013
$v_{C1,d}$	$5.5935 \cdot 10^{-5}$	$3.8426 \cdot 10^{-5}$	$3.4773 \cdot 10^{-6}$	$9.1180 \cdot 10^{-5}$
$v_{C1,q}$	$5.6409 \cdot 10^{-5}$	$3.8704 \cdot 10^{-5}$	$8.7375 \cdot 10^{-5}$	$1.3561 \cdot 10^{-6}$
$v_{C2,d}$	$2.3766 \cdot 10^{-4}$	$1.6955 \cdot 10^{-4}$	$3.9006 \cdot 10^{-4}$	$2.1957 \cdot 10^{-5}$
$v_{C2,q}$	$2.3918 \cdot 10^{-4}$	$1.7068 \cdot 10^{-4}$	$1.7983 \cdot 10^{-5}$	$3.9207 \cdot 10^{-4}$

These two above methods seem to emphasize that the states describing the voltages across the capacitors are the integral of the corresponding currents, i.e., they do not provide any additional information of the system.

Table 6.9: PARTICIPATION FACTORS METHOD IV

State	Mode 1	Mode 2	Mode 3	Mode 4
$i_{1,d}$	0.240	0.2508	0.5316	0.0017
$i_{1,q}$	0.2458	0.2544	0.0296	0.5460
$i_{2,d}$	0.2558	0.2469	0.0339	0.5630
$i_{2,q}$	0.2543	0.2455	0.5188	0.0047
$v_{C1,d}$	0.2502	0.2474	0.0347	0.5328
$v_{C1,q}$	0.2515	0.2485	0.5266	0.0213
$v_{C2,d}$	0.2488	0.2514	0.5481	0.0437
$v_{C2,q}$	0.2498	0.2525	0.0390	0.5353

This fourth method gives the same information as the first method, and the same conclusion can be drawn.

For the presented tables above, only resonant operation is considered. The participation factors can, however, easily be found in any operating point of the system.

6.3 Eigenvalue trajectories in resonant operation

Eigenvalue trajectories can be found by plotting the eigenvalues of the system while varying one or more parameters. A stable system has all the eigenvalues located in the left-hand plane. Eigenvalues located closest to the imaginary axis are the slowest modes of the system; those eigenvalues dominate the others and will have a substantial impact on the system dynamics. Poorly damped oscillations could also be identified, since eigenvalues with low damping ratio, i.e., eigenvalues close to the imaginary axis with a high imaginary part, will inflict such behavior on the system. Any eigenvalues located in the right-half plane would cause instability. Thus, important information regarding stability properties and the dynamic response of the system could be identified by examining the trajectory of the eigenvalues while varying dynamic parameters of the model.

6.3.1 Variable load conditions

As the load may change during operation, it is of interest to determine how this will impact the system dynamics. In the following, CVL and CRL is compared.

The eigenvalue trajectories when the load voltage is varied in the range $0.5V_{2,nom} \leq V_2 \leq 2V_{2,nom}$ and all other parameters are kept constant are shown in Figure 6.1.

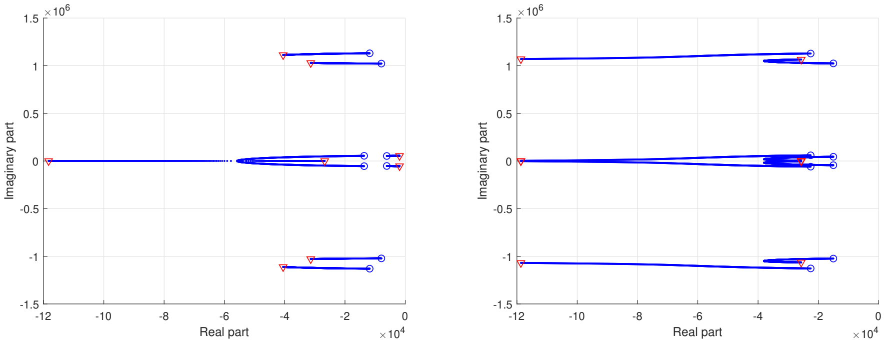

(a) Model with CVL.

(b) Model with CRL.

Figure 6.1: Eigenvalue trajectories when the load voltage is varied. Points marked with a blue circle corresponds to $V_2 = 0.5V_{2,nom}$, whereas points marked with a red triangle corresponds to $V_2 = 2V_{2,nom}$.

As can be seen, a system with CVL has a dominating mode with notably slower dynamics than the system with CRL. Moreover, the rightmost pole-pair in the case with CVL is approaching the imaginary axis as the load voltage is increased, making the system slower, whereas the opposite happens with CRL. At the same time, an increasing real part of the most oscillating modes can be observed in both cases, thus reducing their impact on the system dynamics. The observed trajectories agree with simulation results obtained in Section 5.1.1, as the simulations show that the oscillating dynamics are attenuated faster in the case with low load conditions compared to the case with high load conditions.

6.3.2 Variable coupling conditions

Similarly, the magnetic coupling may also change during operation of the system, and it is therefore of interest to observe how this will impact the dynamic behavior of the system as well.

The eigenvalue trajectories when the coupling factor is varied in the range $0.5k_{nom} \leq k \leq 3k_{nom}$ and all other parameters are kept constant are shown in Figure 6.2.

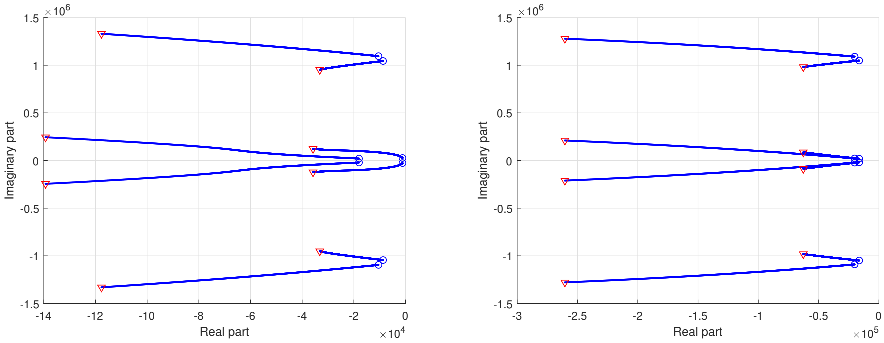

(a) Model with CVL. **(b)** Model with CRL.

Figure 6.2: Eigenvalue trajectories when the coupling coefficient is varied. Points marked with a blue circle corresponds to $k = 0.5k_{nom}$, whereas points marked with a red triangle corresponds to $k = 3k_{nom}$.

As for the above case, the dominating pole-pair with CVL is much closer to the imaginary axis than with CRL, imposing a significant difference in the dynamics of the two systems. The real part of every eigenvalue increases when the coupling factor rises, thus making both systems significantly faster and more damped. This also coincides with the simulation result obtained in Section 5.1.2, since the simulation confirms that the system dynamics indeed are significantly faster and more damped in the case with high coupling factor compared to the case with low coupling factor.

6.3.3 Varying the steady-state solutions

Due to CVL-conditions, which makes the overall system significantly more nonlinear, the steady-state values of $i_{2,d}$ and $i_{2,q}$ appear in the $\boldsymbol{A}$-matrix, in contrast to the CRL-case. Thus, it could be of interest to observe how a change in these steady-state values affects the dynamics of the small-signal model in order to assess the degree of nonlinearity of the system, to some extent

The eigenvalue trajectories when the steady-state value of $i_{2,d,0}$ is varied in the range of $0 < i_{2,d,0} < 60$ A are illustrated in Figure 6.3a and the trajectories when the steady-state value of $i_{2,q,0}$ is varied in the range of $15 < i_{2,q,0} < 55$ A are illustrated in Figure 6.3b. All other parameters are kept constant, and the linearized model is obtained with the nominal parameters reported in Table 3.1.

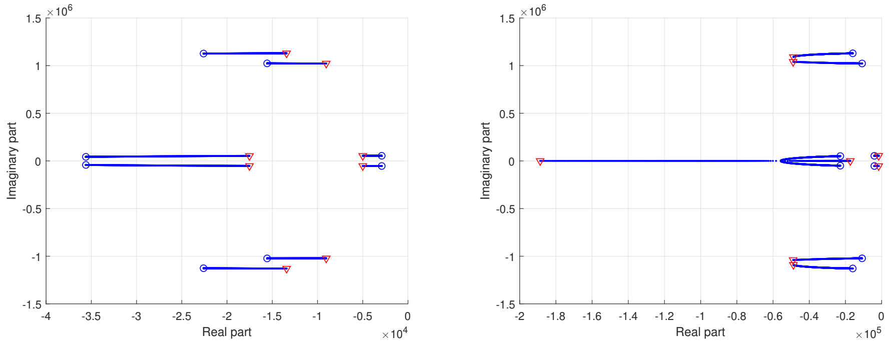

(a) Varying $i_{2,d,0}$.

(b) Varying $i_{2,q,0}$.

Figure 6.3: Eigenvalue trajectories when the steady-state solutions $i_{2,d,0}$ and $i_{2,q,0}$ are varied. Points marked with a blue circle corresponds to the lowest steady-state current, whereas points marked with a red triangle corresponds to the highest steady-state current.

The ranges are not chosen arbitrarily. As derived in Section 4.2, the steady-state solution of $i_{2,d,0}$ equals zero when operating in resonance. It is, however, not zero in off-resonant operation, and, depending on the resonant frequencies of the coils and whether the excitation frequency is sub- or super-resonant, usually varies between -60 and 60 for the operation strategy intended. The impact on the eigenvalues is however symmetric; varying the d-axis steady-state current from 0 to 60 A or from 0 to -60 A gives the same result. As can be seen from Figure 6.3a, a change in the steady-state current shifts the eigenvalues along the real axis. The direction depends upon the direction of the change in the current, but it can be observed that the most dominant poles move in the opposite direction as the others. In any case, a change in the steady-state d-axis current can cause the system to become slower or faster, an effect that would not be apparent in a CRL-modeled system.

The range is not chosen arbitrarily for $i_{2,q,0}$ either. The q-axis steady-state current usually varies between 15 and 55 A and is never observed to be positive in any intended operating condition. Since all parameters are kept constant, and the resonant steady-state solutions are considered (i.e., $i_{2,d,0} = 0$ A), it can be seen that the eigenvalue trajectories are quite similar to the ones observed when varying the load voltage. This behavior is no surprise when considering the entries of the resonant $\boldsymbol{A}$-matrix where $i_{2,q,0}$ shows up, as the q-axis steady-state value only appears multiplied with the load voltage. In any case, a change in the steady-state q-axis current could also have an impact on the system dynamics.

6.4 Eigenvalue trajectories with unbalancing and detuning

As outlined in Chapter 3, the introduction of unbalancing and detuning are necessary in order to modify the steady-state characteristics to obtain a system suitable for power control with varying magnetic coupling by regulating the operating frequency. Eigenvalue trajectories when changing the unbalancing and detuning factor can reveal how the dynamics of the system is affected. Figure 6.4 shows the impact of unbalancing and detuning, respectively, on the eigenvalues of the system.

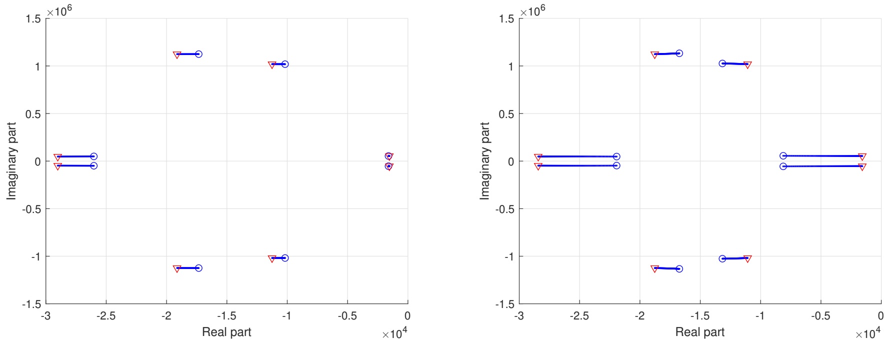

(a) Unbalancing, $0.90 \leq x_u \leq 1.00$.

(b) Detuning, $0.97 \leq x_c \leq 1.03$.

Figure 6.4: Eigenvalue trajectory with unbalancing and detuning. Points marked with a blue circle corresponds to the lowest value, whereas points marked with a red triangle corresponds to the highest value.

The eigenvalue trajectories in Figure 6.4a is drawn in the range $0.90 \leq x_u \leq 1.00$ and with a detuning factor of $x_c = 1.03$. All other parameters are kept constant and equal to the ones reported in Table 3.1. As can be seen, the most dominating mode do not noticeably move, and the dominating dynamics of the system can be expected to remain constant over the whole range of x_u.

The trajectories illustrated in Figure 6.4b are drawn in the range $0.97 \leq x_u \leq 1.03$ and with an unbalance factor of $x_u = 0.98$. All other parameters are kept constant. It can be seen that the real part of the dominating mode increases, making the systems slower as the detuning factor is increased.

6.5 Eigenvalue trajectories in off-resonant operation

The developed nonlinear model is linearizable at any operating point as long as the operating condition of the system is feasible, i.e., as long as the system is operating in continuous conduction mode. It is, therefore, possible to evaluate how the small-signal dynamics change under varying coupling conditions with frequency control to maintain constant power transfer.

The impact on the eigenvalues of the $\boldsymbol{A}$-matrix when the frequency is changed according to Figure 3.9a and Figure 3.12a, respectively, for keeping constant power transfer under variable coupling conditions is shown in Figure 6.5.

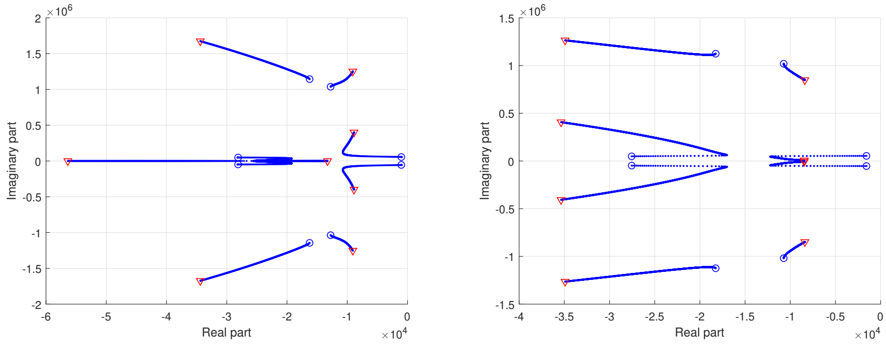

(a) Super-resonant frequency range. **(b)** Sub-resonant frequency range.

Figure 6.5: Eigenvalue trajectory under variable coupling conditions in the range $k_{nom} \leq k \leq 3k_{nom}$ with off-resonant frequency control for maintaining constant output power. Points marked with a blue circle corresponds to $k = k_{nom}$, whereas points marked with a red triangle corresponds to $k = 3k_{nom}$.

As seen from Figure 6.5a, with super-resonant operation, initially a dominant mode occurs with relatively long settling time. As the coupling factor and correspondingly the operating frequency increases, the real part of the dominating mode decreases and the system gets faster. However, only until a point where the movement of the dominating poles changes, making the system slightly slower and less damped for increased coupling factor beyond this point. Some deviation and odd behavior regarding time-domain simulations with high super-resonant operating frequency have been observed in Chapter 5, and the obtained trajectories may not completely represent the actual system dynamics.

For the case with sub-resonant operation, illustrated in Figure 6.5b, it can be observed that initially there exists a dominating pole-pair with a significantly higher real part than the rest. The real part of this mode is, however, quickly decreasing, making the system faster, before a fundamental change suddenly happens. Two of the modes change direction in an apparently extreme but continuous manner at approximately the operating point with coupling factor $k = 1.04k_{nom}$ and operating frequency $\omega = 0.98\omega_0$. Increasing coupling conditions after this point makes the overall system to some extent slower again, but more damped, since the imaginary part of the critical modes is decreasing. Still, the observed behavior seems odd, so in order to confirm the validity of these results, time-domain simulations are again performed, emphasizing points before the sudden change occurs.

Figure 6.6 illustrates the same eigenvalue trajectories as before, but this time with two operating points marked with yellow and green circles. Four of the green circles, however, are almost entirely covered by yellow circles, as these corresponding eigenvalues are less sensitive to perturbations compared to the four others in this operating region.

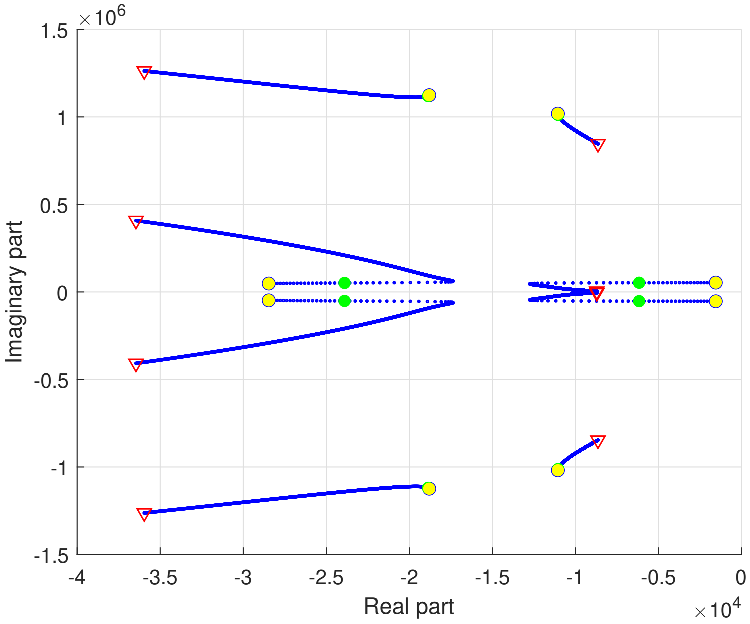

Figure 6.6: Eigenvalue trajectory under variable coupling condition in the range $k_{nom} \leq k \leq 3k_{nom}$ with sub-resonant frequency control for maintaining constant power. Simulation points marked with yellow and green circles.

Figure 6.7 shows the dynamic response to a step in the input voltage in the operating point corresponding to the yellow circles in Figure 6.6, whereas Figure 6.8 shows the model response in the operating point marked with green circles. For the presented simulations, steady-state operation is obtained at the linearization point, before a step change of $V_1 = 1.1V_{1,nom}$ is applied after t = 5 ms.

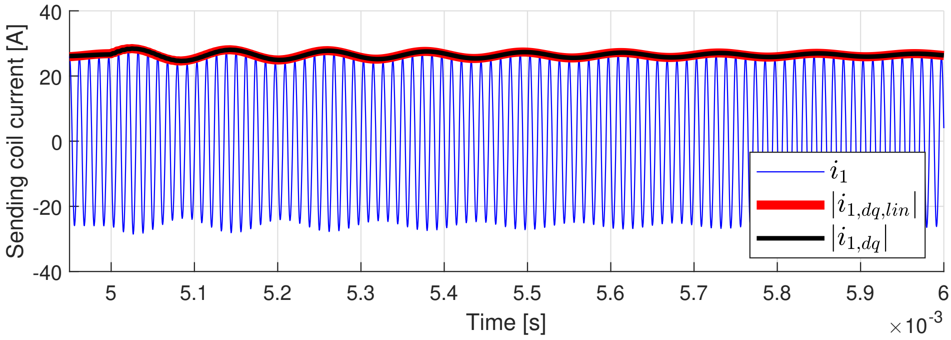

(a) Comparison of the sending side current for the three simulated models.

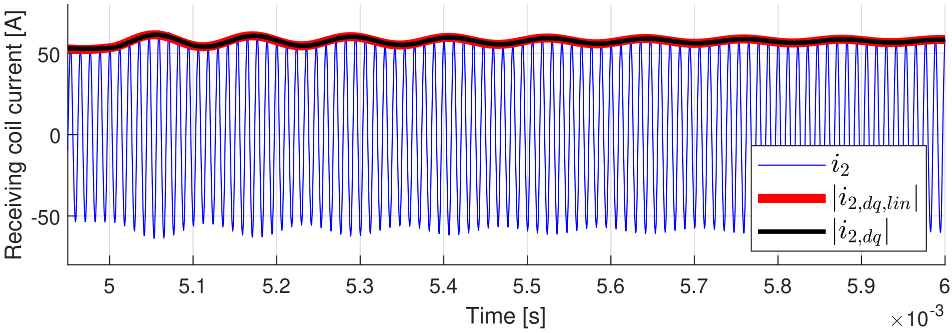

(b) Comparison of the receiving side current for the three simulated models.

Figure 6.7: Model verification by simulation of the circuit, the linearized dq-model and the nonlinear dq-model in the point $\omega = \omega_0$, coupling factor $k = k_{nom}$, unbalance factor $x_u = 0.98$, detuning factor $x_c = 1.03$.

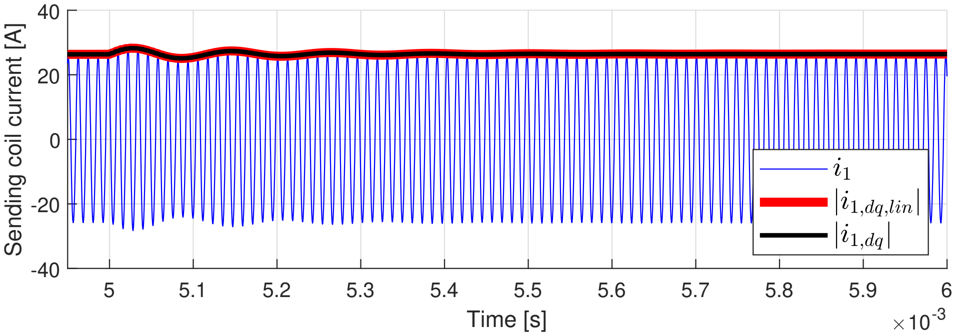

(a) Comparison of the sending side current for the three simulated models.

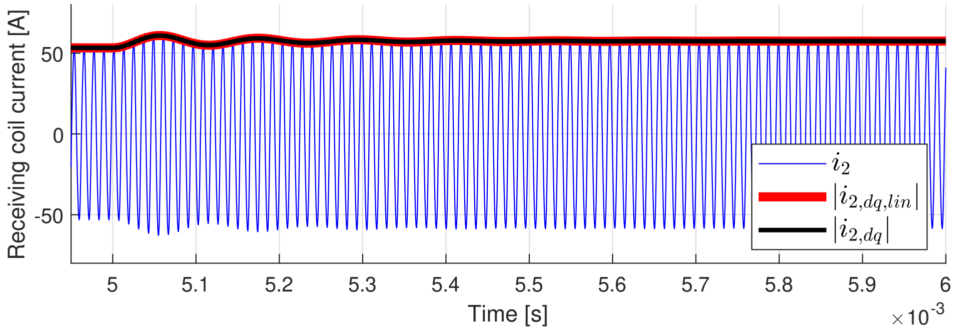

(b) Comparison of the receiving side current for the three simulated models.

Figure 6.8: Model verification by simulation of the circuit, the linearized dq-model and the non-linear dq-model in the point $\omega = 0.988\omega_0$, coupling factor $k = 1.02k_{nom}$, unbalance factor $x_u = 0.98$, detuning factor $x_c = 1.03$.

The above simulations show that the state-space models exhibit the same dynamics as the circuit model, accurately capturing the current envelope. Furthermore, a significantly faster attenuation of the oscillations can be observed when simulating in the operating point marked with green circles compared to the case with yellow circles. These dynamics are expected as the critical mode is much further away from the imaginary axis for the operating point indicated by green circles, according to the observed trajectories. This validation means that the eigenvalue trajectories obtained in Figure 6.5b must be correct.

Simulations in operating points after the sudden change occurs are presented and validated in Chapter 5.

6.6 Controllability Gramian in resonant operation

As outlined in Chapter 2, there are several ways of measuring and interpreting the degree of controllability by analyzing the controllability Gramian:

1) $tr(\boldsymbol{W}_c)$, the average controllability in all directions.

2) $V(\mathcal{E}_{min})$, the set of states that can be reached with a unit or less of input energy.

3) $\lambda_{min}(\boldsymbol{W}_c)$, corresponds to the least controllable direction.

4) $eigenvectors$, the state-space directions.

5) $rank(\boldsymbol{W}_c)$, the controllable subspace.

The state-space model in Equation 4.48 is described by eight state variables and four input variables. However, it is possible to have several different input configurations, e.g., one where the input voltages on both sending and receiving side are controlled, one where only the input voltage on the sending side is controlled and one where only the input voltage on the receiving side is controlled. Moreover, by assuming resonant operation and thereby a constant operating frequency ω, this input variable could in that particular case be treated as a constant parameter. Also, by considering the synchronization of the dq-reference frame, $v_{1,q} = 0$ in steady-state and this input variable could, therefore, be neglected. These assumptions and modifications result in several different variants of the $\boldsymbol{B}$-matrix in the linearized model. When an input variable is disregarded from the input vector $\boldsymbol{u}$, the corresponding column of the input matrix $\boldsymbol{B}$ is eliminated. The resulting input vector and matrix are, however, not shown here for brevity.

6.6.1 Considering all input variables

In this section, both q-axis sending side voltage and operating frequency are treated as input signals. The controllability measures, in this case, are as follows:

1) Input voltages on both the sending and receiving side

$$\lambda_{min}(\boldsymbol{W}_c) = 251.4753 \tag{6.6a}$$

$$tr(\boldsymbol{W}_c) = 8.3450 \cdot 10^7 \tag{6.6b}$$

$$V(\mathcal{E}_{min}) = 1.3813 \cdot 10^3 \tag{6.6c}$$

2) Input voltage on only the sending side

$$\lambda_{min}(\boldsymbol{W}_c) = 134.2109 \tag{6.7a}$$

$$tr(\boldsymbol{W}_c) = 1.4012 \cdot 10^7 \tag{6.7b}$$

$$V(\mathcal{E}_{min}) = 703.3867 \tag{6.7c}$$

3) Input voltage on only the receiving side

$$\lambda_{min}(\boldsymbol{W}_c) = 75.5097 \tag{6.8a}$$

$$tr(\boldsymbol{W}_c) = 6.9438 \cdot 10^7 \tag{6.8b}$$

$$V(\mathcal{E}_{min}) = 1.0148 \cdot 10^3 \tag{6.8c}$$

6.6.2 Disregarding the q-axis input voltage

Now, $v_{1,q}$ are considered to be zero, thus removed from the input vector $\boldsymbol{u}$, and the corresponding column in the $\boldsymbol{B}$-matrix is eliminated. The controllability measures, in this case, reads:

1) Input voltages on both the sending and receiving side

$$\lambda_{min}(\boldsymbol{W}_c) = 79.9368 \tag{6.9a}$$

$$tr(\boldsymbol{W}_c) = 7.9773 \cdot 10^7 \tag{6.9b}$$

$$V(\mathcal{E}_{min}) = 1.1068 \cdot 10^3 \tag{6.9c}$$

2) Input voltage on only the sending side

$$\lambda_{min}(\boldsymbol{W}_c) = 2.2953 \tag{6.10a}$$

$$tr(\boldsymbol{W}_c) = 1.0335 \cdot 10^7 \tag{6.10b}$$

$$V(\mathcal{E}_{min}) = 374.6536 \tag{6.10c}$$

3) Input voltage on only the receiving side

This configuration gives the same results as obtained in the corresponding case where the q-axis voltage component is considered. The results are repeated, regardless:

$$\lambda_{min}(\boldsymbol{W}_c) = 75.5097 \tag{6.11a}$$

$$tr(\boldsymbol{W}_c) = 6.9438 \cdot 10^7 \tag{6.11b}$$

$$V(\mathcal{E}_{min}) = 1.0148 \cdot 10^3 \tag{6.11c}$$

The eigenvectors corresponding to the smallest eigenvalue in these cases are reported below, ordered by rows.

$$\boldsymbol{\xi}_{1,1} = \begin{bmatrix} -0.2017 \\ 0.8452 \\ -0.4943 \\ 0.0028 \\ 0.0072 \\ 2.2857 \cdot 10^{-4} \\ -0.0059 \\ 0.0224 \end{bmatrix} \quad \boldsymbol{\xi}_{2,1} = \begin{bmatrix} 0.3180 \\ -0.8488 \\ 0.4155 \\ -0.0723 \\ -0.0046 \\ 0.0012 \\ 0.0081 \\ -0.0214 \end{bmatrix} \quad \boldsymbol{\xi}_{3,1} = \begin{bmatrix} 0.2075 \\ -0.9716 \\ 0.0963 \\ -0.0589 \\ -0.0094 \\ 0.0018 \\ 2.0853 \cdot 10^{-4} \\ -0..0044 \end{bmatrix} \tag{6.12}$$

$$\boldsymbol{\xi}_{1,2} = \begin{bmatrix} -0.1596 \\ 0.9214 \\ -0.3519 \\ 0.0362 \\ 0.0094 \\ 8.3344 \cdot 10^{-4} \\ -0.0033 \\ 0.0165 \end{bmatrix} \quad \boldsymbol{\xi}_{2,2} = \begin{bmatrix} -0.1708 \\ 0.9234 \\ -0.3416 \\ 0.0332 \\ 0.0100 \\ 0.0011 \\ -0.0031 \\ 0.0153 \end{bmatrix} \quad \boldsymbol{\xi}_{3,2} = \begin{bmatrix} 0.1547 \\ -0.8998 \\ 0.4062 \\ -0.0301 \\ -0.0092 \\ -6.4202 \cdot 10^{-4} \\ 0.0040 \\ -0.0190 \end{bmatrix} \tag{6.13}$$

6.6.3 Assuming constant operating frequency

Six different cases arise with this assumption, as well. In the following, the calculations are made with the same configurations as above, i.e., with input voltages on both sides, only on the sending side and only on the receiving side, both considering and disregarding $v_{1,q}$. The only difference from above is the elimination of ω and corresponding column in the $\boldsymbol{B}$-matrix. The case with only having control of the receiving side will be equal for both, but the results are nonetheless repeated.

1) Considering the q-axis input voltage

1) Input on both sides:

$$\lambda_{min}(\boldsymbol{W}_c) = 251.4676 \tag{6.14a}$$

$$tr(\boldsymbol{W}_c) = 8.3450 \cdot 10^7 \tag{6.14b}$$

$$V(\mathcal{E}_{min}) = 1.1813 \cdot 10^3 \tag{6.14c}$$

2) Input on only the sending side:

$$\lambda_{min}(\boldsymbol{W}_c) = 134.2043 \tag{6.15a}$$

$$tr(\boldsymbol{W}_c) = 1.4012 \cdot 10^7 \tag{6.15b}$$

$$V(\mathcal{E}_{min}) = 703.3792 \tag{6.15c}$$

3) Input on only the receiving side:

$$\lambda_{min}(\boldsymbol{W}_c) = 73.4969 \tag{6.16a}$$

$$tr(\boldsymbol{W}_c) = 6.9438 \cdot 10^7 \tag{6.16b}$$

$$V(\mathcal{E}_{min}) = 1.0147 \cdot 10^3 \tag{6.16c}$$

2) Neglecting the q-axis input voltage

1) Input on both sides:

$$\lambda_{min}(\boldsymbol{W}_c) = 79.9300 \tag{6.17a}$$

$$tr(\boldsymbol{W}_c) = 7.9773 \cdot 10^7 \tag{6.17b}$$

$$V(\mathcal{E}_{min}) = 1.1067 \cdot 10^3 \tag{6.17c}$$

2) Input on only the sending side:

$$\lambda_{min}(\boldsymbol{W}_c) = 2.2915 \tag{6.18a}$$

$$tr(\boldsymbol{W}_c) = 1.0335 \cdot 10^7 \tag{6.18b}$$

$$V(\mathcal{E}_{min}) = 374.5748 \tag{6.18c}$$

3) Input on only the receiving side:

$$\lambda_{min}(\boldsymbol{W}_c) = 73.4969 \tag{6.19a}$$

$$tr(\boldsymbol{W}_c) = 6.9438 \cdot 10^7 \tag{6.19b}$$

$$V(\mathcal{E}_{min}) = 1.0147 \cdot 10^3 \tag{6.19c}$$

.

The eigenvectors corresponding to the smallest eigenvalue in all six configurations are, sorted by rows, respectively:

$$\boldsymbol{\xi}_{1,1} = \begin{bmatrix} -0.2017 \\ 0.8452 \\ -0.4943 \\ -0.0028 \\ 0.0072 \\ 2.2853 \cdot 10^{-4} \\ -0.0059 \\ 0.0224 \end{bmatrix} \quad \boldsymbol{\xi}_{2,1} = \begin{bmatrix} 0.3180 \\ -0.8488 \\ 0.4156 \\ -0.0732 \\ -0.0046 \\ 0.0012 \\ 0.0081 \\ -0.0214 \end{bmatrix} \quad \boldsymbol{\xi}_{3,1} = \begin{bmatrix} 0.2008 \\ -0.8406 \\ 0.5024 \\ 0.0042 \\ -0.0069 \\ -1.1477 \cdot 10^{-4} \\ 0.0059 \\ -0.0225 \end{bmatrix} \tag{6.20}$$

$$\boldsymbol{\xi}_{1,2} = \begin{bmatrix} 0.2055 \\ -0.9565 \\ 0.2023 \\ -0.0413 \\ -0.0094 \\ -0.0016 \\ 0.0017 \\ -0.0094 \end{bmatrix} \quad \boldsymbol{\xi}_{2,2} = \begin{bmatrix} -0.2130 \\ 0.9146 \\ -0.3430 \\ 0.0122 \\ 0.0099 \\ 0.0015 \\ -0.0036 \\ 0.0153 \end{bmatrix} \quad \boldsymbol{\xi}_{3,2} = \begin{bmatrix} 0.2075 \\ -0.9717 \\ 0.0960 \\ -0.0590 \\ -0.0094 \\ -0.0018 \\ 2.0424 \cdot 10^{-4} \\ -0.0044 \end{bmatrix} \tag{6.21}$$

In every case presented above, the controllable subspace is full, i.e. $rank(\boldsymbol{W}_c) = n$.

6.6.4 Summary of controllability Gramian measures

Table 6.10: SUMMARY OF CONTROLLABILITY GRAMIAN MEASURES

Base input	Possibilities	$\lambda_{min}(\boldsymbol{W}_c)$	$tr(\boldsymbol{W}_c)$	$V(\mathcal{E}_{min})$
Considering ω and $v_{1,q}$	1) Both	251.4753	$8.3450 \cdot 10^7$	$1.3813 \cdot 10^3$
	2) Sending	134.2109	$1.4012 \cdot 10^7$	703.3867
	3) Receiving	75.5097	$6.9438 \cdot 10^7$	$1.0148 \cdot 10^3$
Neglecting $v_{1,q}$	1) Both	79.9368	$7.9773 \cdot 10^7$	$1.0168 \cdot 10^3$
	2) Sending	2.2953	$1.0335 \cdot 10^7$	374.6536
	3) Receiving	75.5097	$6.9438 \cdot 10^7$	$1.0148 \cdot 10^3$
Neglecting ω, considering $v_{1,q}$	1) Both	251.4676	$8.3450 \cdot 10^7$	$1.1813 \cdot 10^3$
	2) Sending	134.2043	$1.4012 \cdot 10^7$	703.3792
	3) Receiving	73.4969	$6.9438 \cdot 10^7$	$1.0147 \cdot 10^3$
Neglecting ω and $v_{1,q}$	1) Both	79.9300	$7.9773 \cdot 10^7$	$1.1067 \cdot 10^3$
	2) Sending	2.2915	$1.0335 \cdot 10^7$	374.5748
	3) Receiving	73.4969	$6.9438 \cdot 10^7$	$1.0147 \cdot 10^3$

As seen from Table 6.10, highest controllability is achieved when having the possibility of controlling the voltages on both sides in every case. However, an interesting result arises in the case where both ω and $v_{1,q}$ are considered. It can be observed that the smallest eigenvalue is obtained when eliminating the control on the sending side, which means that it gets harder to control the system in a particular direction in the state-space. The average controllability, the trace of the Gramian, is however higher for the very same case, meaning that it is on average easier to control the whole system around in the state-space.

In the case where $v_{1,q}$ is neglected, a severe drop in controllability is obtained. It can also be observed that eliminating the possibility of actuating on the receiving side significantly decreases the controllability. The smallest eigenvalue is reduced by a factor of approximately 35, and both trace and ellipsoid-volume are subject to a notable decrease. However, reviving the possibility of actuating on the receiving side and at the same time eliminating the input control on the sending side significantly increase all controllability measures compared to the case with an input signal only on the sending side. Compared to the case with the possibility of controlling the voltage on both sides, it can be seen that the controllability measures are not reduced by very much, meaning that having control on the receiving side is the main contributor to overall controllability in this particular case.

When the operating frequency ω is treated as a constant parameter and thereby eliminated, it could be seen, by comparing the obtained measures with the corresponding results where ω is considered, that there is only a minor difference. The average controllability, i.e., the trace of the Gramian, in every case seems identical with the analogous results where the small-signal frequency is considered as an input. This result is, however, due to the use of a precision of five significant figures. Using a precision of six significant figures or more, a slightly higher average controllability in the cases with ω as an input variable is visible. These differences could more easily be seen by investigating the trace of the inverse Gramian, which relates to the average energy needed to steer the system around in the state-space, as this measure appears more sensitive to perturbations. The following only displays the trace of the inverse Gramian for the case without $v_{1,q}$. The same conclusion can, however, be drawn for the case with the q-axis voltage as well:

1) Input on both sides with and without ω_0, respectively:

$$tr(\boldsymbol{W}_{c,1}^{-1}) = 0.0169 \tag{6.22a}$$

$$tr(\boldsymbol{W}_{c,2}^{-1}) = 0.0170 \tag{6.22b}$$

2) Input on sending side with and without ω_0, respectively:

$$tr(\boldsymbol{W}_{c,1}^{-1}) = 0.4554 \tag{6.23a}$$

$$tr(\boldsymbol{W}_{c,2}^{-1}) = 0.4561 \tag{6.23b}$$

3) Input on receiving side with and without ω_0, respectively:

$$tr(\boldsymbol{W}_{c,1}^{-1}) = 0.0200 \tag{6.24a}$$

$$tr(\boldsymbol{W}_{c,2}^{-1}) = 0.0201 \tag{6.24b}$$

From this, it is evident that slightly more energy is needed to move the system around in the state-space without ω as an input variable. However, the differences are minor and show that the frequency input variable does not contribute a lot to overall controllability in resonant operation.

By examining the vectors defining the least controllable directions, the eigenvectors, in the above sections, it can be noted that the absolute values of the entries, in general, do not differ much. However, some eigenvectors point in the opposite direction compared to the others. i.e., every entry has changed sign. This result is no surprise since the energy ellipsoid defining the surface of how far in any direction it is possible to steer the system is symmetric about all axes. Thus, the opposite direction of the eigenvectors will always be just as little controllable as the direction of the eigenvector itself. Since the eigenvectors are quite similar, it means that the least controllable direction does not change much for the different cases.

6.7 Controllability Gramian in off-resonant operation

All the above results regarding controllability are only obtained assuming operation in resonance. Observing how the controllability Gramian behave when the frequency is changed in response to variable coupling could provide valuable information regarding control strategies. In the following, only the full input matrix $\boldsymbol{B}$ is considered.

6.7.1 Sub-resonant frequency range

Figure 6.9 shows the minimum eigenvalue of the controllability Gramian as the operating frequency is changed in response to variable coupling conditions to maintain constant output power.

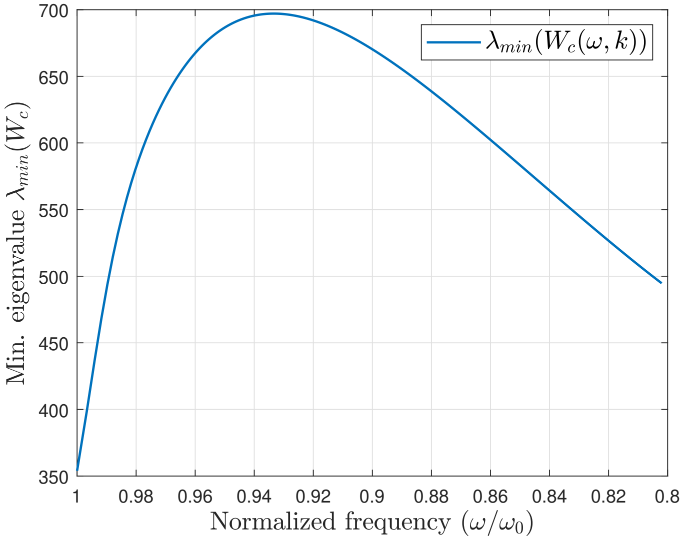

Figure 6.9: Minimum eigenvalue of the controllability Gramian under variable coupling condition in the range $k_{nom} \leq k \leq 3k_{nom}$ with sub-resonant frequency control for maintaining constant output power.

As can be seen, the least controllable direction initially gets easier to control as the operating frequency is reduced, with a local maximum at approximately $\omega = 0.93\omega_0$. Beyond this point, the controllability is decreasing, however, not below the initial measure obtained at a nominal coupling.

Figure 6.10 shows the average controllability and the ellipsoid volume defining the boundary of the reachable states as a function of the coupling factor and operating frequency.

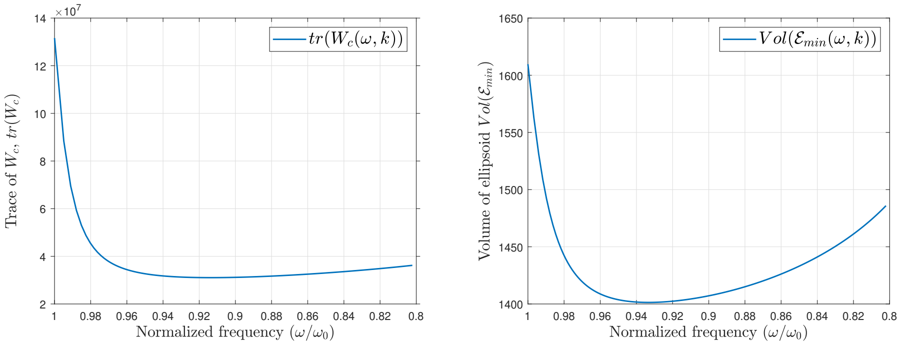

(a) Trace of Gramian.

(b) Volume of ellipsoid.

Figure 6.10: Trace and volume of ellipsoid of the controllability Gramian under variable coupling condition in the range $k_{nom} \leq k \leq 3k_{nom}$ with sub-resonant frequency control for maintaining constant output power.

It can be seen that both the average controllability and the ellipsoid volume is highest at nominal conditions and quickly decreases as the frequency is reduced. A slight increase can be observed beyond the local minima at approximately the same point as the local maxima in Figure 6.9.

6.7.2 Super-resonant frequency range

Similar to above, Figure 6.11 and Figure 6.12 shows the minimum eigenvalue, trace and ellipsoid volume of the controllability Gramian, this time while considering super-resonant operation.

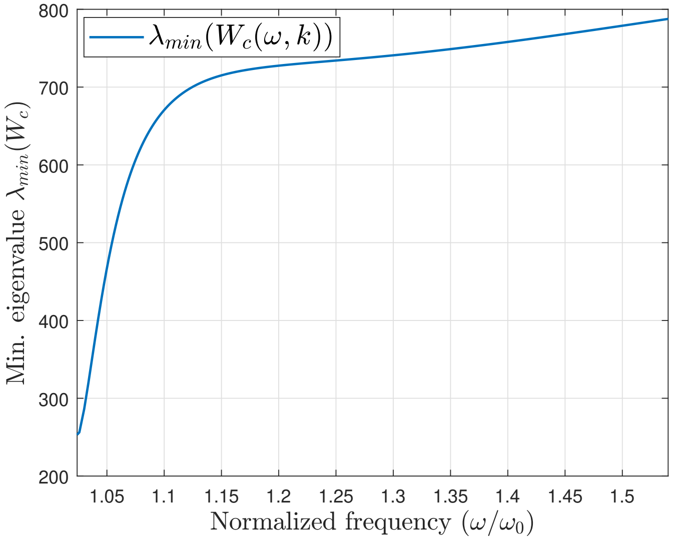

Figure 6.11: Minimum eigenvalue of the controllability Gramian under variable coupling condition in the range $k_{nom} \leq k \leq 3k_{nom}$ with super-resonant frequency control for maintaining constant output power.

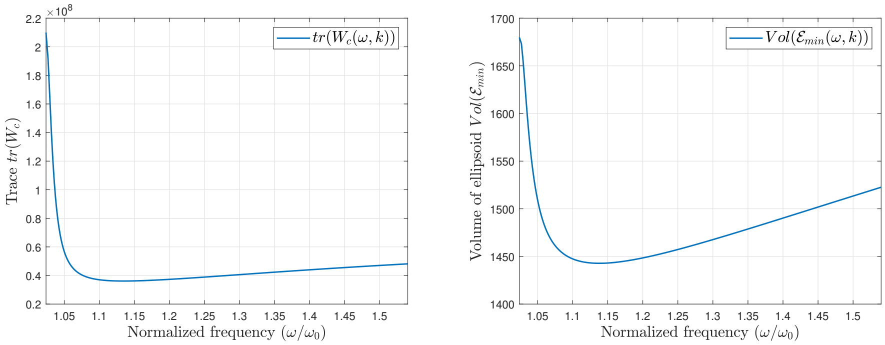

(a) Trace of Gramian.

(b) Volume of ellipsoid.

Figure 6.12: Trace and volume of ellipsoid of the controllability Gramian under variable coupling condition in the range $k_{nom} \leq k \leq 3k_{nom}$ with super-resonant frequency control for maintaining constant output power.

The curves are quite similar to the ones obtained with sub-resonant operation. However, a monotonous increase in controllability with increasing frequency can be seen in Figure 6.11, in addition to a slightly higher value for all three measures.

6.8 Observability Gramian in resonant operation

Similar as for the controllability, there are several ways of measuring and to interpret the level of observability as well, by analyzing the observability Gramian. Depending on the complexity, cost, and safety, different output configurations are possible, i.e., which states to measure. In the following, six different output configurations are investigated. The different output matrices $\boldsymbol{C}$ of the linearized model are not shown, as it will simply have a one on the diagonal corresponding to the measured states. Moreover, the eigenvectors corresponding to the smallest eigenvalues are also omitted in the following.

1) Measuring all currents

A possible output configuration is to measure all currents flowing in the system, which gives the following observability numbers:

$$\lambda_{min}(\boldsymbol{W}_o) = 3.3694 \cdot 10^{-9} \tag{6.25a}$$

$$tr(\boldsymbol{W}_o) = 2.3262 \cdot 10^{-4} \tag{6.25b}$$

$$V(\mathcal{E}_{min}) = 0.0031 \tag{6.25c}$$

2) Measuring the sending side currents

It is also interesting to evaluate the case when having measurement only on the sending side currents:

$$\lambda_{min}(\boldsymbol{W}_o) = 4.8756 \cdot 10^{-10} \tag{6.26a}$$

$$tr(\boldsymbol{W}_o) = 4.9114 \cdot 10^{-5} \tag{6.26b}$$

$$V(\mathcal{E}_{min}) = 0.0013 \tag{6.26c}$$

3) Measuring the receiving side currents

Measuring only the receiving side currents:

$$\lambda_{min}(\boldsymbol{W}_o) = 2.3243 \cdot 10^{-9} \tag{6.27a}$$

$$tr(\boldsymbol{W}_o) = 1.8350 \cdot 10^{-4} \tag{6.27b}$$

$$V(\mathcal{E}_{min}) = 0.0027 \tag{6.27c}$$

4) Measuring the sending side states

Measuring all sending side currents and voltages:

$$\lambda_{min}(\boldsymbol{W}_o) = 4.0861 \cdot 10^{-6} \tag{6.28a}$$

$$tr(\boldsymbol{W}_o) = 0.4332 \tag{6.28b}$$

$$V(\mathcal{E}_{min}) = 0.1209 \tag{6.28c}$$

5) Measuring the receiving side states

Measuring all receiving side currents and voltages:

$$\lambda_{min}(\boldsymbol{W}_o) = 1.0995 \cdot 10^{-6} \tag{6.29a}$$

$$tr(\boldsymbol{W}_o) = 0.0913 \tag{6.29b}$$

$$V(\mathcal{E}_{min}) = 0.0589 \tag{6.29c}$$

6) Measuring every states

Measuring all currents and voltages in the system:

$$\lambda_{min}(\boldsymbol{W}_o) = 6.3140 \cdot 10^{-6} \tag{6.30a}$$

$$tr(\boldsymbol{W}_o) = 0.5245 \tag{6.30b}$$

$$V(\mathcal{E}_{min}) = 0.1376 \tag{6.30c}$$

6.8.1 Summary of observability Gramian measures

A summary of the obtained observability numbers is reported in Table 6.11.

Table 6.11: SUMMARY OF OBSERVABILITY GRAMIAN MEASURES

Measurement	$\lambda_{min}(\boldsymbol{W}_o)$	$tr(\boldsymbol{W}_o)$	$V(\mathcal{E}_{min})$
Currents	$3.3694 \cdot 10^{-9}$	$2.3262 \cdot 10^{-4}$	0.0031
Sen. currents	$4.8756 \cdot 10^{-10}$	$4.9114 \cdot 10^{-5}$	0.0013
Rec. currents	$2.3243 \cdot 10^{-9}$	$1.8350 \cdot 10^{-4}$	0.0027
Sending side	$4.0861 \cdot 10^{-6}$	0.4332	0.1209
Receiving side	$1.0995 \cdot 10^{-6}$	0.0913	0.0589
Every state	$6.3140 \cdot 10^{-6}$	0.5245	0.1376

Not surprisingly, measuring all state variables results in highest overall observability, whereas having measurements only on the sending currents result in the worst observability measures. It can also be noted that observing all sending side states results in better overall observability than observing the receiving side states, whereas measuring the receiving side currents gives better observability than measuring the sending side currents.

In the specialization project, numerous resonant analysis of the controllability and observability Gramians were performed with varying load- and coupling conditions. These results are not included here.

6.9 Observability Gramian in off-resonant operation

Similar to the controllability measures, all the above results regarding observability are only obtained assuming operation in resonance. Therefore, off-resonant Gramian analysis is provided here as well. In the following, only measurements of all currents are considered.

6.9.1 Sub-resonant frequency range

Figure 6.13 shows the minimum eigenvalue of the observability Gramian along the constant power frequency trajectory and Figure 6.14 shows the average controllability and the ellipsoid volume.

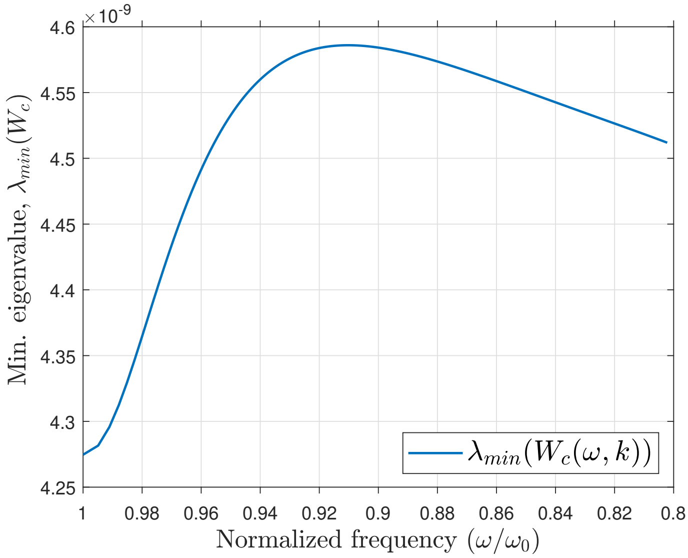

Figure 6.13: Minimum eigenvalue of the observability Gramian under variable coupling condition in the range $k_{nom} \leq k \leq 3k_{nom}$ with sub-resonant frequency control for maintaining constant output power.

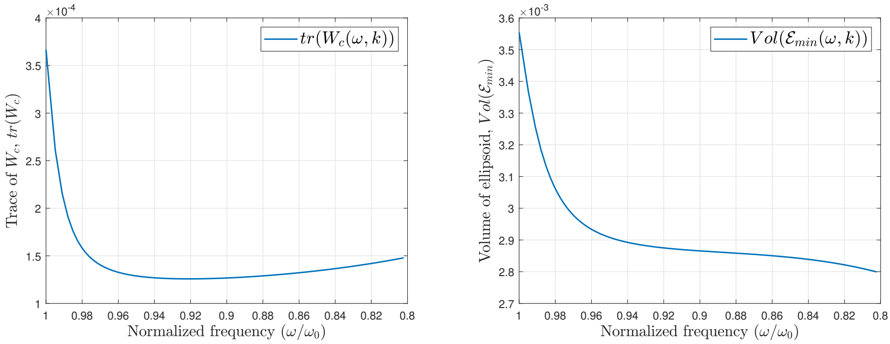

(a) Trace of Gramian.

(b) Volume of ellipsoid.

Figure 6.14: Trace and volume of ellipsoid of the observability Gramian under variable coupling condition in the range $k_{nom} \leq k \leq 3k_{nom}$ with sub-resonant frequency control for maintaining constant output power.

As can be seen, the least observable direction gets easier to observe with reduced operating frequency, whereas the opposite happens to the average controllability and the set of states reachable with one unit or less of input energy.

6.9.2 Super-resonant frequency range

Similar to above, Figure 6.15 and Figure 6.16 shows the minimum eigenvalue, trace and ellipsoid volume of the observability Gramian, this time while considering super-resonant operation.

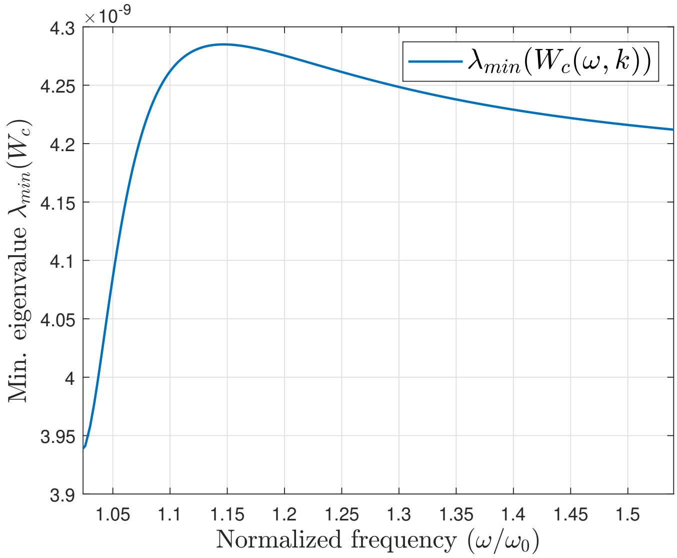

Figure 6.15: Minimum eigenvalue of the observability Gramian under variable coupling condition in the range $k_{nom} \leq k \leq 3k_{nom}$ with super-resonant frequency control for maintaining constant output power.

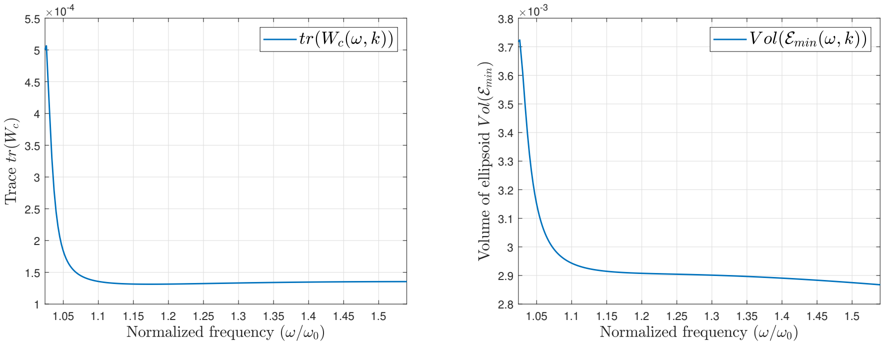

(a) Trace of Gramian.

(b) Volume of ellipsoid.

Figure 6.16: Trace and volume of ellipsoid of the observability Gramian under variable coupling condition in the range $k_{nom} \leq k \leq 3k_{nom}$ with super-resonant frequency control for maintaining constant output power.

Quite similar curves as for the sub-resonant case can be seen here as well, albeit with a slightly higher trace and ellipsoid volume. The minimum eigenvalue, however, is marginally lower.

6.10 Chapter summary

Small-signal stability and sensitivity analysis in a wide range of operating conditions have been investigated in this chapter, revealing how the system dynamics change under proposed control strategies and variable load and coupling conditions. The analysis has discovered that there exists a pole-pair that significantly dominates the system dynamics in the case for resonant operation and which states that participate the most in these modes. Two dominating pole-pairs have been observed in the case with an off-resonant operation and with medium to high coupling conditions. Eigenvalue-based comparison between the two load modeling approaches CRL and CVL has uncovered that the dominating modes of the former are significantly more damped, indicating that such load modeling is deceiving when examining the system dynamics. Moreover, controllability and observability Gramians are analyzed, providing insight into how the control properties change with different input-output configurations and how they change over the range intended for frequency control.

Chapter 7

Frequency Domain Analysis and Power Control

In this chapter, a model order reduction procedure is presented, along with the resulting reduced-order approximation. The obtained reduced-order model is implemented in MATLAB/Simulink/Simscape environment and validated through time-domain simulations. Furthermore, small-signal frequency characteristics are used to design control loops. A simple PI-controller is utilized for providing the necessary input frequency to keep constant output power under variable coupling conditions, and simulations are performed in order to assess the closed-loop performance.

7.1 Model order reduction

Lower-order systems are well recognized and easy to understand in terms of characteristics such as settling time, damping, time constants, and oscillations. Higher-order systems are more complex and harder to manipulate and work with relative to lower-order models regarding, e.g., analysis and design of controllers. Therefore, model order reduction could prove very useful when dealing with higher-order systems. Techniques such as dominant pole approximation and discarding states that do not influence the dynamic behavior of the system could be applied in order to obtain such reduction. It is, however, important that the reduced-order model conserves the dynamic properties and characteristics of the original model that is important for the application of the system. Thus, verification of the behavior of the reduced-order model in, e.g., frequency- and time-domain is crucial

A technique for obtaining a lower-order model that preserves the dynamics of interest is the balanced truncation model reduction strategy. There are two methods of the balanced truncation realization: The matched-dc-gain method and the direction-deletion method. The matched dc-gain strategy discards states that have the least effect on the system behavior and alters the remaining states to enforce a dc-gain match between the approximated lower-order and the original full-order model. This technique ensures an accurate steady-state response in the time-domain, at the expense of accurate transient behavior. The direction-deletion strategy discards states with low energy contributions without altering the remaining states and tends to provide a more exact match in fast transients, at the expense of steady-state behavior[33].

7.1.1 Bode frequency response

The linearized model consists of four input signals and potential of eight output signals, i.e., there exists up to thirty-two input-output transfer functions. In the following, the preferred output signal would be the receiving side power. Thus, the input-output pair mainly contributing to power transfer under the proposed voltage control strategy in resonant operation could be investigated.

The power at the receiving side can be expressed in dq-components as:

$$\begin{aligned} P_{out} &= v_{2,d} \cdot i_{2,d} + v_{2,q} \cdot i_{2,q} \\ &= \frac{i_{2,d}^2}{\sqrt{i_{2,d}^2 + i_{2,q}^2}} \cdot \frac{4}{\pi} \cdot V_{dc,out} + \frac{i_{2,q}^2}{\sqrt{i_{2,d}^2 + i_{2,q}^2}} \cdot \frac{4}{\pi} \cdot V_{dc,out} \end{aligned} \tag{7.1}$$

As earlier outlined, the linearized output equation can be written:

$$\Delta \boldsymbol{y} = \boldsymbol{C}(\boldsymbol{x}^p, \boldsymbol{u}^p) \cdot \Delta \boldsymbol{x} + \boldsymbol{D}(\boldsymbol{x}^p, \boldsymbol{u}^p) \cdot \Delta \boldsymbol{u} \tag{7.2}$$

where the matrices are defined as follows:

$$\boldsymbol{C}(\boldsymbol{x}^p, \boldsymbol{u}^p) = \left.\frac{\partial g_i}{\partial \boldsymbol{x}}\right|_{\boldsymbol{x}^p, \boldsymbol{u}^p} \qquad \boldsymbol{D}(\boldsymbol{x}^p, \boldsymbol{u}^p) = \left.\frac{\partial g_i}{\partial \boldsymbol{u}}\right|_{\boldsymbol{x}^p, \boldsymbol{u}^p} \tag{7.3}$$

Thus, with $y = P_{out}$, there are no feedforward term in the output equation and the $\boldsymbol{D}$-matrix is zero. The only two non-zero entries of the output matrix $\boldsymbol{C}$ can be found as:

$$\begin{aligned} C_{1,3} &= \left.\frac{\partial y}{\partial i_{2,d}}\right|_{\substack{\boldsymbol{x}=\boldsymbol{x}^p \\ \boldsymbol{u}=\boldsymbol{u}^p}} = \frac{i_{2,d,0}}{\sqrt{i_{2,d,0}^2 + i_{2,q,0}^2}} \cdot \frac{4}{\pi} \cdot V_{dc,out,0} \\ C_{1,4} &= \left.\frac{\partial y}{\partial i_{2,q}}\right|_{\substack{\boldsymbol{x}=\boldsymbol{x}^p \\ \boldsymbol{u}=\boldsymbol{u}^p}} = \frac{i_{2,q,0}}{\sqrt{i_{2,d,0}^2 + i_{2,q,0}^2}} \cdot \frac{4}{\pi} \cdot V_{dc,out,0} \end{aligned} \tag{7.4}$$

and the output matrix in this case is therefore the vector:

$$\boldsymbol{C} = \begin{bmatrix} 0 & 0 & C_{1,3} & C_{1,4} & 0 & 0 & 0 & 0 \end{bmatrix} \tag{7.5}$$

Where $C_{1,3}$ and $C_{1,4}$ are the results from Equation 7.4. The frequency and step response of the eight-order transfer function from $v_{1,d}$ to $y = P_{out}$ is displayed in Figure 7.1;

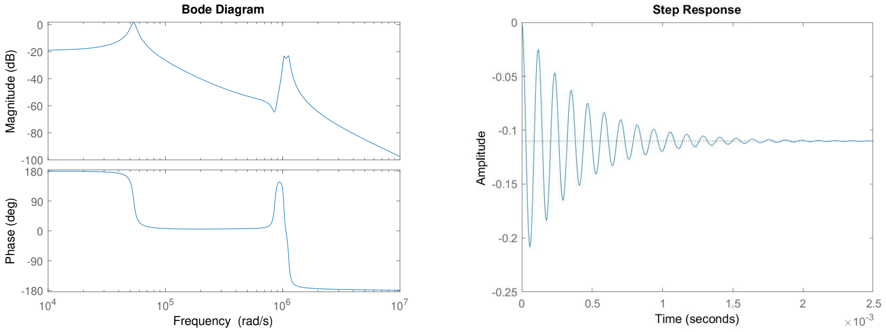

Figure 7.1: Frequency and step response for transfer function from $v_{1.d}$ to P_{out}.

Since the system is oscillating due to complex poles, a first-order approximation is impossible. However, a fourth-order or even a second-order approximation could provide consistent results.

When utilizing methods for model order reduction, it is crucial to verify that the lower-order approximation does not present inaccuracies at important frequencies for the desired application. Therefore, frequency and time-domain responses are presented. In the following, only the matched dc-gain method is examined.

Figure 7.2 shows the frequency response of the original system compared to both a fourth-and second-order approximation.

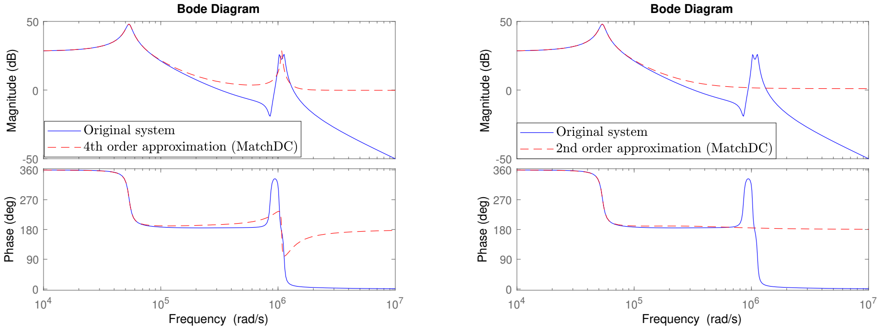

Figure 7.2: Frequency response of the original and reduced-order models.

It can be seen that the fourth-order transfer function gives a reasonable approximation around both resonance peaks in addition to a perfect match at lower frequencies. The second-order approximation, however, does not capture the dynamics of the original system at high frequencies but provides a good match at lower frequencies. Thus, in order to verify the reduced models, step-responses are presented in the following.

Figure 7.3 illustrates the dynamic behavior of the models to a step in the sending side voltage. Clearly, at these frequencies, both reduced-order models capture the response of the original system to an input step seemingly equally good.

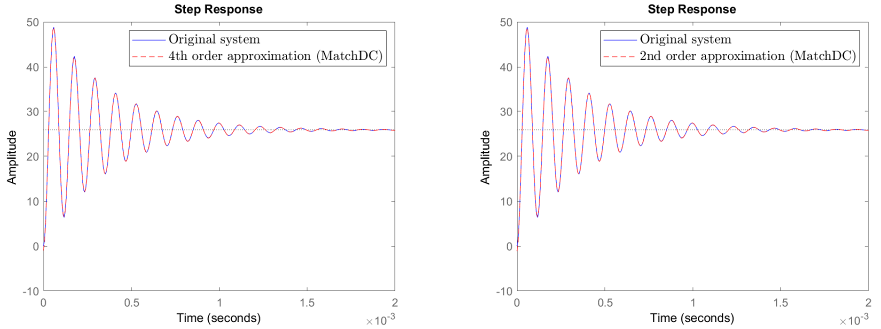

Figure 7.3: Step response of the original and reduced-order models.

For the second-order approximation, the poles are found as:

$$eig(h_{2nd}(s)) = -2728 \pm i53840 \tag{7.6}$$

The most dominant pole-pair, i.e., the poles with the lowest real part in terms of absolute value, of the original model is found in Table 6.1 as $-2902 \pm i53558$. Comparing the poles of the second-order system to the dominant pole-pair of the original eight-order system reveals that they are almost the same, meaning that this pole-pair significantly dominates the response of the original model and that it does not exist any zeros nearby that reduces the influence of these poles. Therefore, the most influencing dynamics can be well represented by a second-order model.

In the presented reduction strategy, only one channel of the multiple-input multiple-output system was emphasized. For multivariable systems, the Bode frequency response does not provide all necessary information as there are interactions between the input-output pairs. Furthermore, the input and output signals are vectors, meaning they do have directions associated with them, and the gain of such system depends on the direction of the input signals. Singular value decomposition is a generalization of the Bode frequency response and is applicable for multivariable systems as well. The maximum gain as the direction of the input signal is varied is the maximum singular value of the system, whereas the minimum gain is the minimum singular value. For single-input single-output systems, however, the singular value frequency response equals the Bode magnitude plot[34].

7.1.2 Singular value frequency response

For this purpose, the power at both sides of the link is considered. The power at the sending side can be describes in dq-components as:

$$P_{in} = v_{1,d} \cdot i_{1,d} + v_{1,q} \cdot i_{1,q} \tag{7.7}$$

The only non-zero element can be found as:

$$C_{1,1} = \left.\frac{\partial P_{in}}{\partial i_{1,d}}\right|_{\substack{\boldsymbol{x}=\boldsymbol{x}^p \\ \boldsymbol{u}=\boldsymbol{u}^p}} = v_{1,d,0} = V_{1,0} \tag{7.8}$$

Thus, with $\boldsymbol{y} = [P_{in} \quad P_{out}]^T$, the augumented output matrix becomes:

$$\boldsymbol{C} = \begin{bmatrix} V_{1,0} & 0 & 0 & 0 & 0 & 0 & 0 & 0 \\ 0 & 0 & \frac{4 \cdot i_{2,d,0} \cdot V_{dc,out,0}}{\pi \sqrt{i_{2,d,0}^2 + i_{2,q,0}^2}} & \frac{4 \cdot i_{2,q,0} \cdot V_{dc,out,0}}{\pi \sqrt{i_{2,d,0}^2 + i_{2,q,0}^2}} & 0 & 0 & 0 & 0 \end{bmatrix} \tag{7.9}$$

Figure 7.4 and Figure 7.5 shows the corresponding singular value frequency plot of the original eight-order system compared to a fourth- and second-order approximation. Both the matched dc-gain and direction-deletion method are examined and compared, labeled ”MatchDC” and ”Truncate,” respectively.

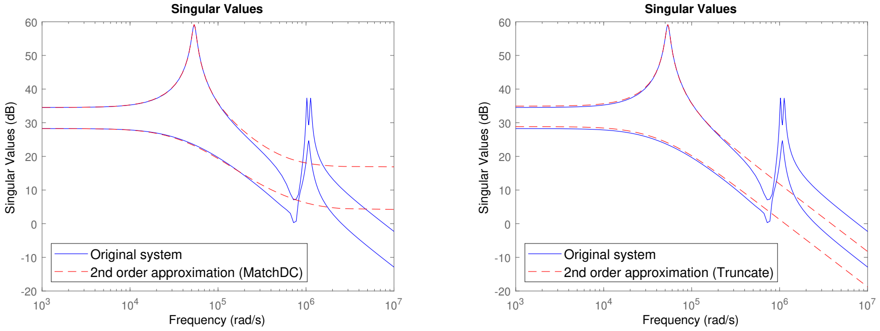

Figure 7.4: Singular value frequency response, 2nd order approximation.

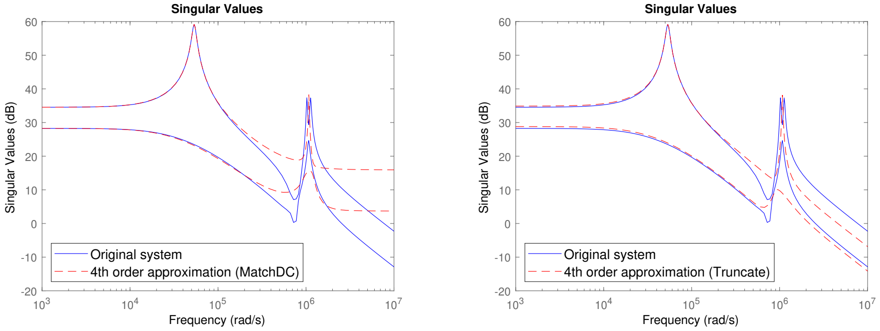

Figure 7.5: Singular value frequency response, 4th order approximation.

As expected, it can be seen that the direction-deletion method provides a better match at high frequencies compared to the matched dc-gain method, but a slight deviation in the steady-state gain can be observed. Moreover, similar as with the Bode frequency response, the fourth-order methods provides a better match around the second resonance peak compared to the second-order approximations.

To further demonstrate the accuracy of the lower-order approximations, time-domain responses are examined. In the following, only the results obtained with the direction-deletion method are considered. Figure 7.6 illustrates the behavior of the receiving side power to a step in the sending side voltage and operating frequency, respectively, comparing both the lower-order models to the full-order original system.

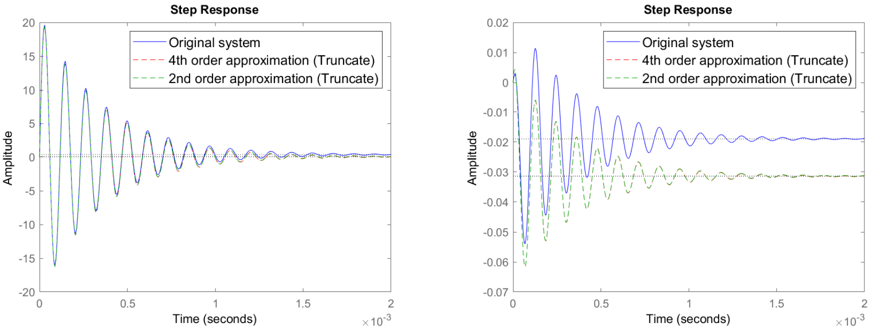

Figure 7.6: Step response from inputs $v_{1,d}$ and ω to $y = P_{out}$, respectively.

It can be seen that both of the reduced-order models quite accurately captures the dynamics of the original system. However, a slight steady-state error occur, as expected with the direction-deletion method. To further extend the validity of the lower-order-approximation, the second-order model is implemented in the Simulink environment.

In state-space representation, the second-order model reads:

$$\begin{aligned} \dot{\boldsymbol{x}}(t) &= \boldsymbol{A}\boldsymbol{x}(t) + \boldsymbol{B}\boldsymbol{u}(t) \\ \boldsymbol{y}(t) &= \boldsymbol{C}\boldsymbol{x}(t) + \boldsymbol{D}\boldsymbol{u}(t) \end{aligned} \tag{7.10}$$

where the $\boldsymbol{A}$- and $\boldsymbol{B}$-matrices are reduced to simply:

$$\boldsymbol{A} = \begin{pmatrix} 14000 & 60950 \\ -51790 & -19750 \end{pmatrix} \quad \boldsymbol{B} = \begin{pmatrix} 753.3 & -215.7 & 0.1033 & 1072 \\ -562.4 & 34.3 & -1.349 & 1456 \end{pmatrix} \tag{7.11}$$

The output matrices for the approximated model reads:

$$\boldsymbol{C} = \begin{pmatrix} 1017 & -640.6 \\ -1206 & -1757 \end{pmatrix} \quad \boldsymbol{D} = \begin{pmatrix} 0 \end{pmatrix} \tag{7.12}$$

Figure 7.7 compares the dynamic response of the models, similar to the simulations in

Chapter 5. However, the original eight-order small-signal model is swapped with the second-order model obtained above.

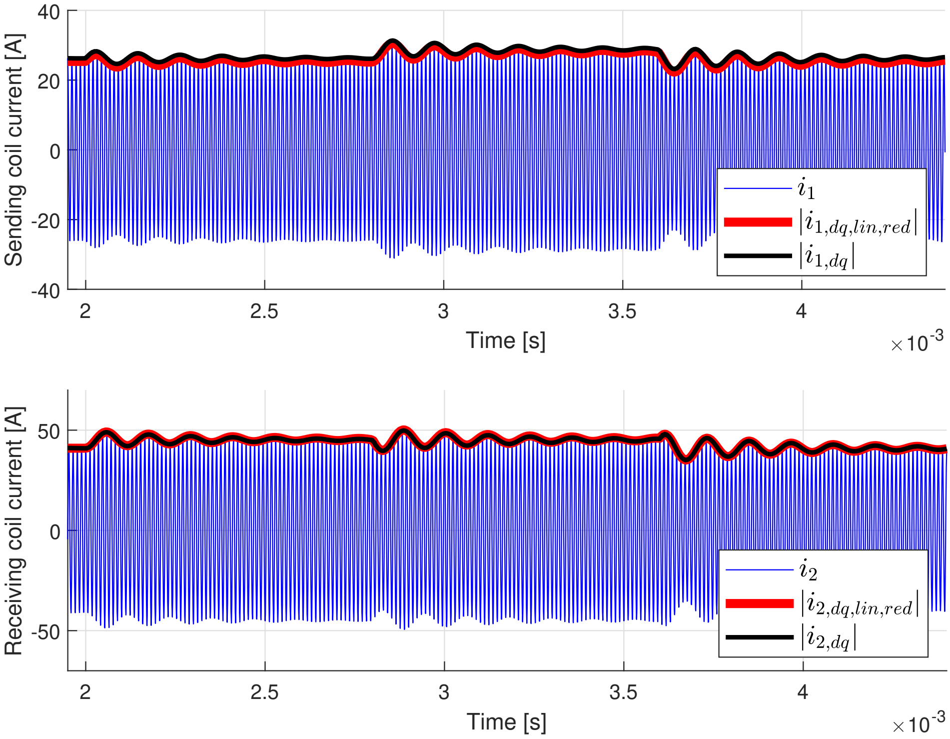

Figure 7.7: Verification of the reduced-order approximated model by simulation of the circuit, the reduced-order model and the nonlinear dq-model in resonant operation.

In order to acquire the current dynamics, both the sending and receiving side output power is divided by the respective voltages. The simulation sequence is identical to the one outlined in Section 5.1. As can be seen, the reduced model does not exhibit any noticeable deviation from the slowly-varying oscillations of the nonlinear dq-model apart from a slight steady-state-error, thus seemingly capturing the envelope of the current amplitudes almost equally good as the full-order linear model obtained in Section 4.3. This behavior is expected since the system is dominated by one eigenvalue-pair in resonant operation, as explained in Chapter 6. However, potential high-frequency oscillations on top of the oscillations observed in Figure 7.7 cannot be captured by a second-order approximated method. In any case, these above steps show that there exist suitable reduced-order models preserving essential dynamics of the full-order model.

7.2 Power control

The small-signal model can be used to analyze frequency domain characteristics along the constant power frequency trajectory obtained in the stationary analysis in Chapter 3. From these frequency responses, it is possible to investigate and utilize the internal stability margins of the input-output pairs of interest to design suitable control loops.

7.2.1 Sub-resonant operation

Figure 7.8 shows the frequency response for three different coupling factors of the transfer function from the small-signal frequency input ω to P_{in} and P_{out}, respectively, considering sub-resonant operation.

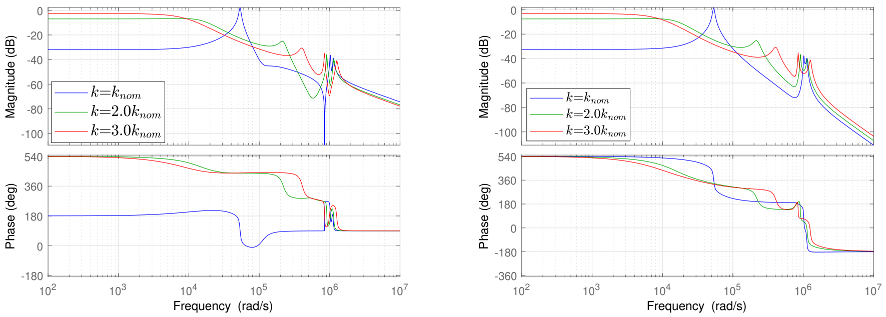

Figure 7.8: Frequency response from ω to $y = P_{in}$ and $y = P_{out}$, respectively.

A simple PI-controller can provide the necessary operating frequency in response to variable coupling conditions to control the power transfer according to the trajectory obtained in the stationary analysis in Chapter 3.

In order to directly control the power transferred to the load, it would be necessary to use the output power P_{out} as the feedback signal of the control loop. Thus, a wireless feedback path would be required to avoid communication wires across the air gap of the IPT-system. However, closing the feedback loop around only the sending side would be advantageous, as the whole control system could be realized in the transmitter with no communication across the link.

The open loop transfer functions from the reference signal to respectively the input and output power can be expressed as:

$$
\begin{aligned}
\frac{P_{in}}{P_{ref}}(s) &= h_r(s)h_{p1}(s)h_f(s) = K_p\frac{1+T_is}{T_is}h_{p1}(s)\frac{1}{1+T_fs}\\
\frac{P_{out}}{P_{ref}}(s) &= h_r(s)h_{p2}(s)h_f(s) = K_p\frac{1+T_is}{T_is}h_{p2}(s)\frac{1}{1+T_fs}
\end{aligned}
\tag{7.13}
$$

In these equations, $h_{p1}(s)$ and $h_{p2}(s)$ are the plant transfer functions from the input frequency ω to P_{in} and P_{out}, respectively. The transfer function $h_r(s)$ is the PI-controller and $h_f(s)$ is a low-pass filter for providing the average value of the output power. The time-constant of the filter is chosen as $T_f = 100/2\pi f_0$.

In order to achieve robust closed-loop performance over the whole variation range $k_{nom} \leq k \leq 3k_{nom}$, the general frequency characteristics in Figure 7.8 are utilized to design the PI-controller parameters such that no overshoot or oscillations occur at operating conditions where the system dynamics are fast, as a damped response is desired over the whole intended operating range. Considering this restriction, the controller parameters are tuned for the worst-case scenario to $K_p = -0.65057$ and $T_i = 1/2846$.

The frequency response of the transfer functions in Equation 7.13 for three different coupling conditions along the constant power frequency trajectory is shown in Figure 7.9 with the corresponding phase- and gain margins indicated by circles. It has been established through time-domain simulations and stability analysis that the dynamics over the analyzed range of sub-resonant frequency control are slowest at the lowest coupling. Thus, the design for damped response at high coupling factor conditions implies a relatively slow response at a low coupling factor.

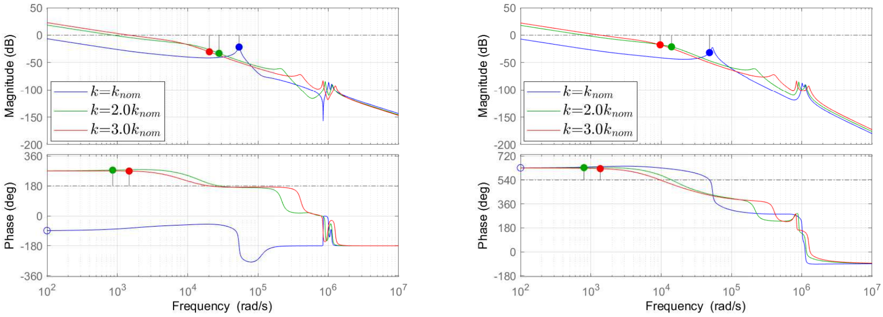

Figure 7.9: Frequency response from P_{ref} to $y = P_{in}$ and $y = P_{out}$, respectively.

For the receiving side frequency response, it can be noted that the gain margin is not limited by the resonance peak, as the blue circle is indicated slightly beneath the peak, making this particular condition having the largest gain margin. This is in contrast to the frequency response of the sending side, where a sufficient increase in the controller gain would first lead to instability for the case with low coupling factor.

The intended closed-loop block scheme is shown in Figure 7.10.

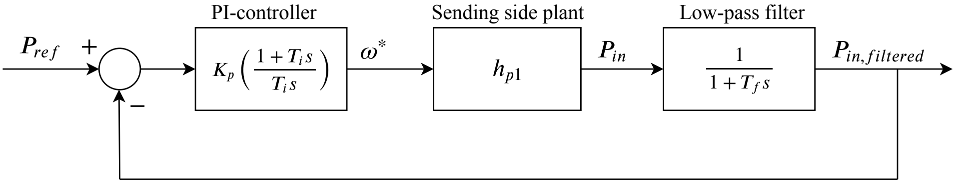

Figure 7.10: Block diagram of sending side power feedback control.

To illustrate the performance when using only sending side power feedback for the control, a sequence of steps is applied in the coupling factor, as shown in Figure 7.11a, and Figure 7.11b shows the resulting output power. The operating frequency resulting as output from the PI-controller is shown in Figure 7.12. As can be seen, the response is much faster in the case of a high coupling coefficient, which is expected when considering the eigenvalue trajectories obtained in Figure 6.5b and the frequency characteristics in Figure 7.9. By comparing the steady-state frequency trajectory obtained in Figure 3.9a with the closed-loop controller output in Figure 7.12, it can be confirmed that the operation with closed-loop power control follows the sub-resonant frequency trajectory for maintaining 1 pu power obtained from the steady-state analysis. It can also be seen that there is no significant difference in the dynamics of the input and output power, only a deviation due to practical losses – the efficiency of the system – is observed.

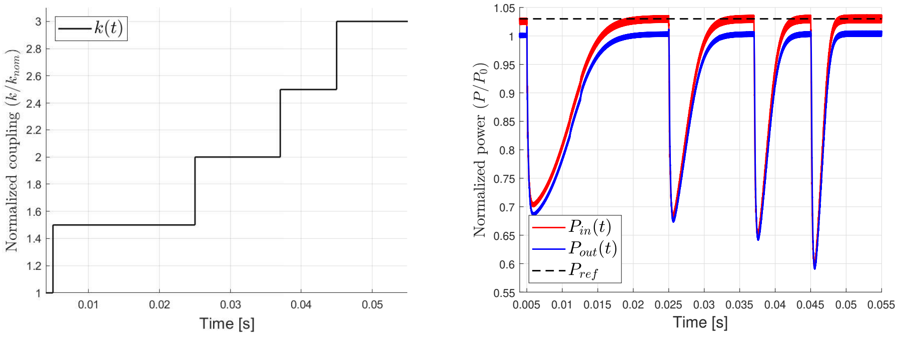

(a) **(b)**

Figure 7.11: Closed-loop response to steps in the coupling factor with sub-resonant control based solely on sending side feedback. Power normalized to $P_0 = P(k_{nom}, \omega_0, x_u = 0.98, x_c = 1.03)$.

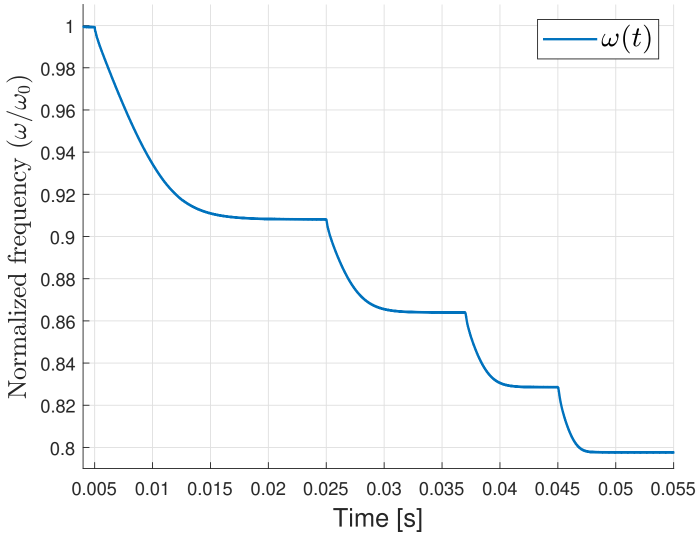

Figure 7.12: Closed-loop controller response to steps in the coupling factor.

An additional demonstration of the closed-loop control performance is shown in Figure 7.13. In this case, the system is initially operating at the secondary side resonance frequency according to the red curve in Figure 3.8a with $k = 3k_{knom}$ and a correspondingly low power reference of 0.32 pu. A step in the sending side power reference to 0.66 pu is applied at t = 5 ms, and a second step in the power reference is applied at t = 32 ms, bringing the system to the operating point corresponding to nominal power transfer indicated by the red circle in Figure 3.8a. The operating frequency resulting from the PI-controller is shown in Figure 7.13b, clearly illustrating how the response is stable and well damped over the entire operating region, but much faster when approaching operation at rated power at a high coupling factor.

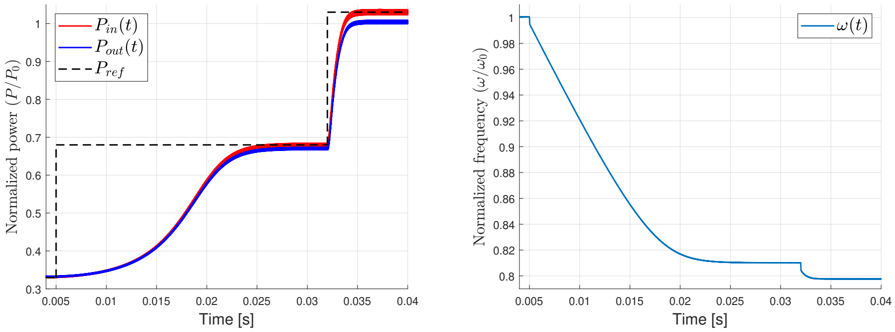

(a) **(b)**

Figure 7.13: Closed-loop response to steps in the power reference with control based solely on sending side feedback. Power normalized to $P_0 = P(k_{nom}, \omega_0, x_u = 0.98, x_c = 1.03)$.

From the small-signal analysis and the above closed-loop responses, it is seen that the nonlinear system exhibits very different dynamics over the variation range $k_{nom} \leq k \leq 3k_{nom}$, i.e., the dynamics are markedly changing from one operating condition to another. A PI-controller with a single set of controller parameters was implemented above, and the closed-loop response revealed significant slower dynamics at conditions with low coupling compared to high. Therefore, a gain-scheduled controller could provide better results, which is a controller that adapts to any number of operating conditions chosen. With this controller scheme, the gain and integral time of the PI-controller are changed based on the values of a scheduling variable[35]. In order to implement a proper gain-scheduled PI-controller, the nonlinear model is linearized at five operating points corresponding to 1 pu power transfer, namely at every step change of the coupling factor k illustrated in Figure 7.11a. The PI-controller is then tuned for all five steady-state operating points of the plant, thus providing different controller parameters, and the coupling factor is used as the scheduling variable. For this purpose, a parallel PI-controller i utilized, of which the transfer function reads:

$$h_r(s) = K_p + \frac{1}{T_i s} \tag{7.14}$$

The controller parameters for each value of the scheduled variable k is reported in Table 7.1.

Table 7.1: GAIN-SCHEDULED CONTROLLER PARAMTERS

k	K_p	T_i
$1.0k_{nom}$	0	$-\frac{1}{142000}$
$1.5k_{nom}$	-6.41	$-\frac{1}{38800}$
$2.0k_{nom}$	-2.82	$-\frac{1}{14000}$
$2.5k_{nom}$	-1.84	$-\frac{1}{7620}$
$3.0k_{nom}$	-1.57	$-\frac{1}{5080}$

Figure 7.14 illustrates the closed-loop response with the gain-scheduled controller.

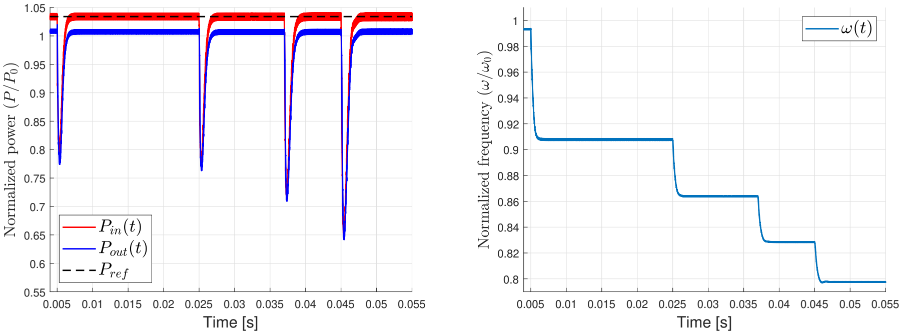

Figure 7.14: Response to steps in the power reference with gain-scheduled control based solely on sending side feedback. Power normalized to $P_0 = P(k_{nom}, \omega_0, x_u = 0.98, x_c = 1.03)$.

Indeed, a significantly faster closed-loop response can be observed, especially for the case with low coupling conditions. The closed-loop dynamics are still damped and stable over the entire operating region.

7.2.2 Super-resonant operation

As illustrated and explained in Chapter 3, super-resonant frequency control could also provide a constant output power under variable coupling conditions. Figure 7.15 shows the frequency response of the transfer function from the small-signal frequency input ω to P_{in} and P_{out}, respectively, considering super-resonant operation.

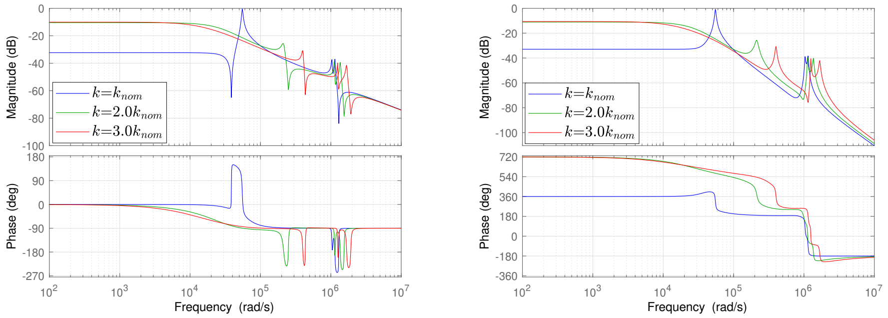

Figure 7.15: Frequency response from ω to $y = P_{in}$ and P_{out}, respectively.

The open loop transfer functions from the reference signal to the input and output power can be described in the same way as for the case with sub-resonant frequency control. For this situation, the controller parameters are selected as $K_p = 2.759$ and $T_i = 1/5126$. The frequency response for three different coupling conditions is shown in Figure 7.16, with the corresponding gain- and phase margins marked with circles.

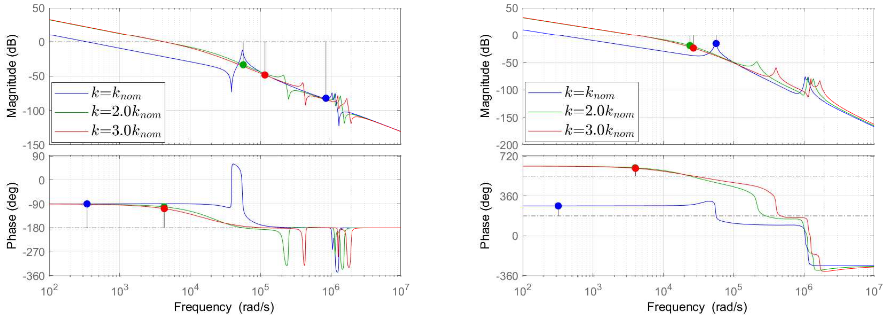

Figure 7.16: Frequency response from P_{ref} to $y = P_{in}$ and $y = P_{out}$, respectively.

Notice how the gain margin in the case with lowest coupling for the sending side is indicated at a significant higher frequency than the first resonance peak due to the positive phase contribution at the frequencies around that particular peak.

Furthermore, similar as above, utilizing sending side power feedback for the control gives the closed-loop performance illustrated in Figure 7.17. The sequence of steps in the coupling factor is identical as in Figure 7.11a.

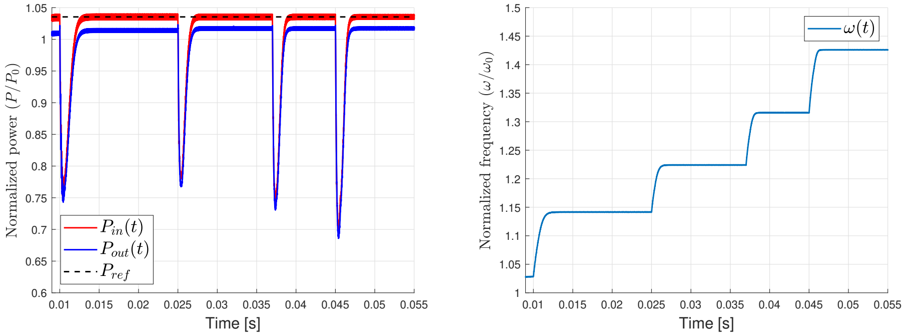

Figure 7.17: Closed-loop response to steps in the coupling factor with super-resonant control based solely on sending side feedback. Power normalized to $P_0 = P(k_{nom}, \omega_0, x_u = 0.95, x_c = 0.97)$.

As can be observed, the output of the controller for maintaining constant output power accurately follows the steady-state frequency trajectory obtained in Figure 3.12a. It can also be seen that a more fast response over the whole variation range $k_{nom} \leq k \leq 3k_{nom}$ is achieved with super-resonant frequency control.

7.3 Chapter summary

This chapter has explained a strategy for obtaining a reduced-order model based on balanced truncation realization, and the resulting model has been validated through time-domain simulations. The lower-order approximated model is observed to accurately capture the dominating modes of the full-order model, albeit exhibiting some slight steady-state deviation. Subsequently, frequency domain characteristics have been exploited in order to design a robust PI-controller for ensuring a damped closed-loop response over the whole intended operating range. Time-domain simulations with a closed feedback path have confirmed that the operating frequency provided by the PI-controller quite accurately follows the constant power frequency trajectory obtained in the stationary analysis. Furthermore, closing the feedback path around the sending side, thus indirectly controlling the output power, has revealed no significant change in the closed-loop performance.

Chapter 8

Closing Remarks

8.1 Conclusion

This work has provided a thorough investigation of an SS-compensated IPT-system with CVL, intended for both resonant and off-resonant operation. A nonlinear state-space representation of the IPT-system has been derived, expressed in dq-axis variables in an SRF. Furthermore, a general small-signal state-space model is presented, valid in the full range of expected operating conditions. Through the model derivation and linearization procedure, it is seen that the complexity of the equations describing the system dynamics and the steady-state solutions vastly increases in off-resonant conditions compared to resonant.

Phasor modeling has been utilized to find the necessary operating frequency in order to keep the output power constant under variable coupling conditions, and small-signal stability properties have been investigated along this frequency curve to assess the impact on the system dynamics. These analyses have shown that the system is significantly slower with low coupling factor compared to high. Furthermore, some odd behavior of the eigenvalue trajectories is observed during the intended sub-resonant power control strategy, thus causing notable variation in the system dynamics along the constant power frequency trajectory.

Numerous time-domain simulations have confirmed the validity of the presented state-space models, which are verified to accurately capture the envelopes of the fundamental frequency currents in the IPT-system in several different operating points. Simulations with high coupling factor in off-resonant frequency range have revealed that the state-space models exhibit some slight deviations due to the waveform distortions occurring at these conditions, thus decreasing the accuracy of the small-signal analysis performed in the vicinity of these operating points. Especially operation in super-resonant frequency range far from resonance has shown a relatively large deviation.

Input-output frequency characteristics have proven valuable in order to obtain a reduced-order approximated model capturing important dynamics of the full-order model. A small steady-state error is obtained as the reduction method used for this realization ensures good transient match at the expense of steady-state behavior. Additionally, small-signal frequency responses are utilized to design a simple PI-controller to provide the operating frequency necessary for maintaining constant output power under variable coupling conditions, and the controller response is analogous to the results achieved in the steady-state analysis. Time-domain simulations have shown that relying solely on sending side power feedback does not noticeably alter the output power dynamics, thus eliminating the need for communication across the air gap of the sending and receiving side of the IPT-system.

8.2 Future work

There are several paths of future work to pursue leading from this. As a general linearized multiple-input multiple-output state-space-representation has been presented, valid in any feasible operating point, extensive study of multivariable control design and performance issues can be investigated. Frequency responses such as singular value decomposition can be assessed to gain insight into the directional of the system, as well as frequency domain performance and robustness, i.e., how effective feedback control is. If the control scheme design designed in this work is to be used in practical systems, experimental tests and verification in real-time should be performed, with power measurements from actual sensors. Moreover, the control scheme includes a low-pass filter, making the feedback control slow. Other options of providing a dc-value of the power should be investigated, which could increase the closed-loop performance. In a practical IPT-system, further requirements for the control strategy arise from e.g., parameter uncertainties and disturbances, which would also need to be considered. The main future goal would be to design and implement a dual frequency/voltage control scheme and experimentally test and verify the results.

Bibliography

[1] G. A. Covic and J. T. Boys. ”Inductive power transfer”. *Proceedings of the IEEE*, 101(6):1276–1289, June 2013.

[2] G. A. Covic and J. T. Boys. ”Modern trends in inductive power transfer for transportation applications”. *IEEE Journal of Emerging and Selected Topics in Power Electronics*, 1(1):28–41, March 2013.

[3] K. Hata, T. Imura, and Y. Hori. ”Dynamic wireless power transfer system for electric vehicles to simplify ground facilities - power control and efficiency maximization on the secondary side”. In *2016 IEEE Applied Power Electronics Conference and Exposition (APEC)*, pages 1731–1736, March 2016.

[4] M. Longo, D. Zaninelli, F. Viola, P. Romano, and R. Miceli. ”How is the spread of the electric vehicles?”. In *2015 IEEE 1st International Forum on Research and Technologies for Society and Industry Leveraging a better tomorrow (RTSI)*, pages 439–445, Sep. 2015.

[5] G. Guidi, J. A. Suul, F. Jenset, and I. Sorfonn. ”Wireless charging for ships: high-power inductive charging for battery electric and plug-in hybrid vessels”. *IEEE Electrification Magazine*, 5(3):22–32, Sep. 2017.

[6] W. C. Brown. ”The history of wireless power transmission”. *Solar Energy*, 56:3–21, 12 1996.

[7] S. Y. Choi, B. W. Gu, S. Y. Jeong, and C. T. Rim. ”Advances in wireless power transfer systems for roadway-powered electric vehicles”. *IEEE Journal of Emerging and Selected Topics in Power Electronics*, 3(1):18–36, March 2015.

[8] J. C. Schuder. ”Powering an artificial heart: birth of the inductively coupled-radio frequency system in 1960”. *Artificial organs*, 26:909–15, 12 2002.

[9] A. Banerji, T. Datta, G. Bandyopadhyay, S. K. Biswas, A. Banerji, and A. Banerji. ”Wireless transfer of power: status and challenges”. In *2016 International Conference on Intelligent Control Power and Instrumentation (ICICPI)*, pages 251–257, Oct 2016.

[10] A. W. Green and J. T. Boys. ”10 kHz inductively coupled power transfer-concept and control”. In *1994 Fifth International Conference on Power Electronics and Variable-Speed Drives*, pages 694–699, Oct 1994.

[11] W. Zhang and C. C. Mi. ”Compensation topologies of high-power wireless power transfer systems”. *IEEE Transactions on Vehicular Technology*, 65(6):4768–4778, June 2016.

[12] C. C. Mi, G. Buja, S. Y. Choi, and C. T. Rim. ”Modern advances in wireless power transfer systems for roadway powered electric vehicles”. *IEEE Transactions on Industrial Electronics*, 63(10):6533–6545, Oct 2016.

[13] K. Aditya and S. S. Williamson. ”Comparative study of series-series and series-parallel compensation topologies for electric vehicle charging”. In *2014 IEEE 23rd International Symposium on Industrial Electronics (ISIE)*, pages 426–430, June 2014.

[14] Chwei-Sen Wang, O. H. Stielau, and G. A. Covic. ”Design considerations for a contactless electric vehicle battery charger”. *IEEE Transactions on Industrial Electronics*, 52(5):1308–1314, Oct 2005.

[15] G. Guidi and J. A. Suul. ”Minimizing converter requirements of inductive power transfer systems with constant voltage load and variable coupling conditions”. *IEEE Transactions on Industrial Electronics*, 63(11):6835–6844, Nov 2016.

[16] R. Bosshard, J. W. Kolar, J. Mühlethaler, I. Stevanović, B. Wunsch, and F. Canales. ”Modeling and η-α-pareto optimization of inductive power transfer coils for electric vehicles”. *IEEE Journal of Emerging and Selected Topics in Power Electronics*, 3(1):50–64, March 2015.

[17] A. Foote and O. C. Onar. ”A review of high-power wireless power transfer”. In *2017 IEEE Transportation Electrification Conference and Expo (ITEC)*, pages 234–240, June 2017.

[18] G. Guidi and J. A. Suul. ”Modelling techniques for designing high-performance on-road dynamic charging systems for electric vehicles”. In *Proceedings of the 31st*

International Electric Vehicle Symposium and Exhibition & International Electric Vehicle Technology Conference, page 7, 09 2018.

[19] R. C. Fernandes and A. A. de Oliveira. ”Theoretical bifurcation boundaries for wireless power transfer converters”. In *2015 IEEE 13th Brazilian Power Electronics Conference and 1st Southern Power Electronics Conference (COBEP/SPEC)*, pages 1–4, Nov 2015.

[20] C. S. Wang, G. A. Covic, and O. H. Stielau. ”Power transfer capability and bifurcation phenomena of loosely coupled inductive power transfer systems”. *IEEE Transactions on Industrial Electronics*, 51(1):148–157, Feb 2004.

[21] J. A. Suul and G. B. Diaz. ”Reduction and linearization of MMC models for interaction and system stability studies”, 2015.

[22] F. Garofalo, L. Iannelli, and F. Vasca. ”Participation factors and their connections to residues and relative gain array”. *IFAC Proceedings Volumes*, 35(1):125 – 130, 2002.

[23] W. A. Hashlamoun, M. A. Hassouneh, and E. H. Abed. ”New results on modal participation factors: revealing a previously unknown dichotomy”. *IEEE Transactions on Automatic Control*, 54(7):1439–1449, July 2009.

[24] C. T. Chen. ”Linear system theory and design”. *International Journal of Robust and Nonlinear Control*, 10:1360–1362, 01 2000.

[25] T. H. Summers, F. L. Cortesi, and J. Lygeros. ”On submodularity and controllability in complex dynamical networks”. *IEEE Transactions on Control of Network Systems*, 3(1):91–101, March 2016.

[26] S. R. Sanders, J. M. Noworolski, X. Z. Liu, and G. C. Verghese. ”Generalized averaging method for power conversion circuits”. *IEEE Transactions on Power Electronics*, 6(2):251–259, April 1991.

[27] Z. U. Zahid, Z. M. Dalala, C. Zheng, R. Chen, W. E. Faraci, J. J. Lai, G. Lisi, and D. Anderson. ”Modeling and control of series–series compensated inductive power transfer system”. *IEEE Journal of Emerging and Selected Topics in Power Electronics*, 3(1):111–123, March 2015.

[28] D. Gunji, T. Imura, and H. Fujimoto. ”Envelope model of load voltage on series-series compensated wireless power transfer via magnetic resonance coupling”. In *2015 IEEE PELS Workshop on Emerging Technologies: Wireless Power (2015 WoW)*, pages 1–6, June 2015.

[29] K. Song, C. Zhu, K. Koh, D. Kobayashi, T. Imura, and Y. Hori. ”Modeling and

design of dynamic wireless power transfer system for EV applications". In *IECON 2015 - 41st Annual Conference of the IEEE Industrial Electronics Society*, pages 005229–005234, Nov 2015.

[30] R. Tavakoli and Z. Pantic. "Analysis, Design, and Demonstration of a 25-kW Dynamic Wireless Charging System for Roadway Electric Vehicles". *IEEE Journal of Emerging and Selected Topics in Power Electronics*, 6(3):1378–1393, Sep. 2018.

[31] M. K. Das, A. M. Kulkarni, and P. B. Darji. "Comparison of DQ and dynamic phasor based frequency scanning analysis of grid-connected power electronic systems". In *2016 Power Systems Computation Conference (PSCC)*, pages 1–7, June 2016.

[32] B. Crowhurst, E. F. El-Saadany, L. E. Chaar, and L. A. Lamont. "Single-phase grid-tie inverter control using DQ transform for active and reactive load power compensation". In *2010 IEEE International Conference on Power and Energy*, pages 489–494, Nov 2010.

[33] P. J. Patil and M. D. Patil. "Model order reduction of high order LTI system using balanced truncation Approximation". In *2011 International Conference on Process Automation, Control and Computing*, pages 1–6, July 2011.

[34] S. Skogestad and I. Postlethwaite. *Multivariable Feedback Control: Analysis and Design*, volume 2. 01 2005.

[35] K. Vance and J. Thorp. "Gain scheduling applications in small signal stability of power systems". In *2013 IEEE Power Energy Society General Meeting*, pages 1–5, July 2013.

Appendix A

Matlab Code

Overview of the most important MATLAB files used in this report is presented in Table A.1. The table includes a short description of the files, and the dependency column state which scripts the particular MATLAB file uses. Indeed, numerous other scripts were written and used in this work but are not reported here.

Table A.1: OVERVIEW OF MATLAB-FILES

Filename	Description	Dependency
steadyState	Initialize CVL nonlinear model for fsolve	None
getSteadyState	Returns CVL steady-state by fsolve	steadyState
getStateSpace	Returns CVL state-space by fsolve	getSteadyState
steadyState_Req	Initialize CRL nonlinear model for fsolve	None
getSteadyState_Req	Returns CRL steady-state by fsolve	steadyState_Req
getStateSpace_Req	Returns CRL state-space by fsolve	getSteadyState_Req
solveForOmega	Initialize power equation for fsolve	None
getOmega_constP_subres	Returns sub-res. omega for const. power	solveForOmega
getOmega_constP_supres	Returns sup-res. omega for const. power	solveForOmega
getPower	Returns the output power with CVL	None
getPower_Req	Returns the output power with CRL	None
getPower_Vdc	Returns the output power with varying load	None
IPTCharacteristics_subres	Finds sub-res. IPT-characteristics for three different coupling conditions	getPower, getSteadyState
IPTCharacteristics_supres	Finds sup-res. IPT-characteristics for three different coupling conditions	getPower, getSteadyState
IPTCharacteristics_xu	Finds IPT-characteristics for three different unbalance factors	getPower, getSteadyState
IPTCharacteristics_xc	Finds IPT-characteristics for three different detuning factors	getPower, getSteadyState
IPTCharacteristics_nom	Finds nominal IPT-characteristics for four different coupling factors	getPower
IPTCharacteristics_Vdc	Finds IPT-characteristics for four different load voltages	getPower_Vdc
sweepEig_constP_subres	Finds sub-res. eigenvalue-, frequency-, impedance-, current-, and Gramian trajectories	getPower, getStateSpace getOmega_constP_subres
sweepEig_constP_supres	Finds sup-res. eigenvalue-, frequency-, impedance-, current-, and Gramian trajectories	getPower, getStateSpace getOmega_constP_supres
freqResp_subres	Finds sub-res. frequency respons for three different coupling factors	getPower, getStateSpace getOmega_constP_subres
freqResp_supres	Finds sup-res. frequency respons for three different coupling factors	getPower, getStateSpace getOmega_constP_supres
getSymSteadyState	Returns symbolic CVL steady-state	None
getSymStateSpace	Returns symbolic CVL state-space	getSymSteadyState
getSymSteadyState_Req	Returns symbolic CRL steady-state	None
getSymStateSpace_Req	Returns symbolic CRL state-space	getSymSteadyState_Req
getEigen	Returns eigenvectors of $\boldsymbol{A}$-matrix	getStateSpace
parametricSensitivity	Finds parametric sensitivity to eigenvalues	getSymStateSpace, getEigen
parametricSensitivity_SS	Finds parametric sensitivity to ss-currents	getSymStateSpace, getEigen
participationFactor	Finds participation factors	getStateSpace
modelReduction	Finds lower-order models	getStateSpace
sweepEig (1-6)	Finds eigenvalue trajectories	getSymStateSpace
sweepSSCurrent (1-2)	Finds current trajectories	getSymStateSpace
simulation	Simulates the models and plots the currents	getPower, getStateSpace

Appendix **B**

Maple Code

Overview of the most important Maple files used in this report is presented in Table B.1. The table includes a short description of the files. Several other scripts were written and used in this work but are not reported here.

Table B.1: OVERVIEW OF MAPLE-FILES

Filename	Description
coilCurrents_Res_CVL	Finds the steady-state coil currents assuming resonance and CVL
coilCurrents_Res_CRL	Finds the steady-state coil currents assuming resonance and CRL
coilCurrents_General_CVL	Finds the general steady-state coil currents and R_{eq}
coilCurrentsDQ_Res_CVL	Finds the steady-state dq coil currents assuming resonance and CVL
coilCurrentsDQ_Res_CRL	Finds the steady-state dq coil currents assuming resonance and CRL
coilCurrentsDQ_General_CVL	Finds the general steady-state dq coil currents
equivalentImpedance_CRL	Finds the equivalent sending side impedance

Appendix C

Simulink Diagrams

This appendix displays some of the most important Simulink diagrams developed in this work. Figure C.1 shows the simulation model for the overall IPT-system displayed in Figure 2.3, and Figure C.2 shows the contents of the subsystem. The detached sine wave scheme is utilized when simulating steps in the operating frequency. Configuration parameters such as solver type and max step size have been carefully chosen in order to make this model work properly. Simscape-blocks are colored cyan, subsystem-blocks are colored blue, to workspace-blocks are colored magenta, step-blocks are colored yellow and all other normal Simulink-blocks are white. Indeed, this model is augmented with power feedback and low-pass filtering for the case with power control, but the resulting model is not displayed here.

C.1 Circuit model

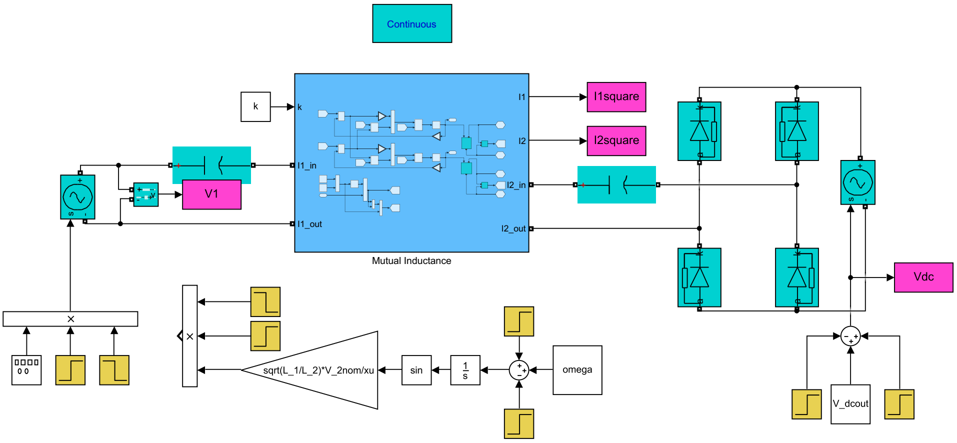

Figure C.1: Circuit model.

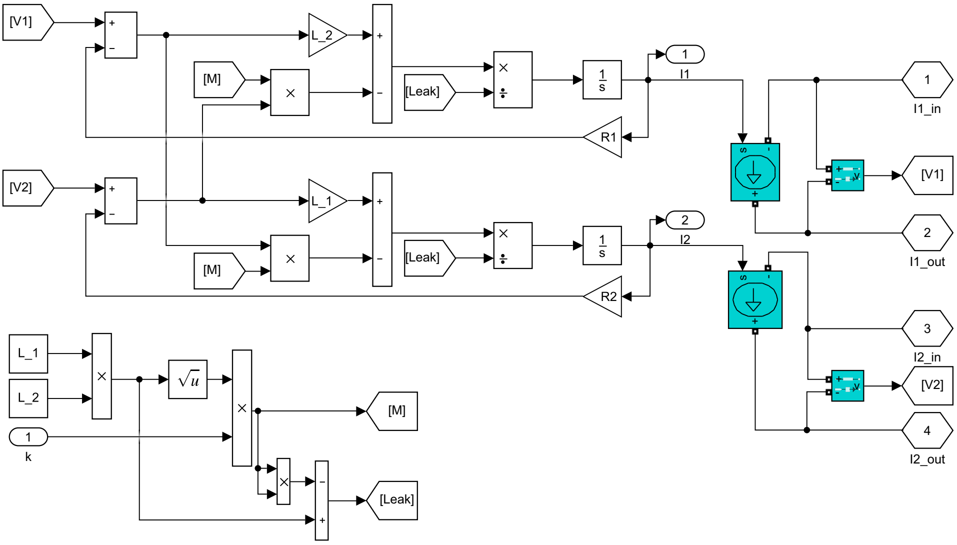

Figure C.2: Subsystem of the circuit model.

C.2 Nonlinear state-space model

The Simulink diagram of the nonlinear dq-model is shown in Figure C.3, along with its subsystems in Figure C.4.

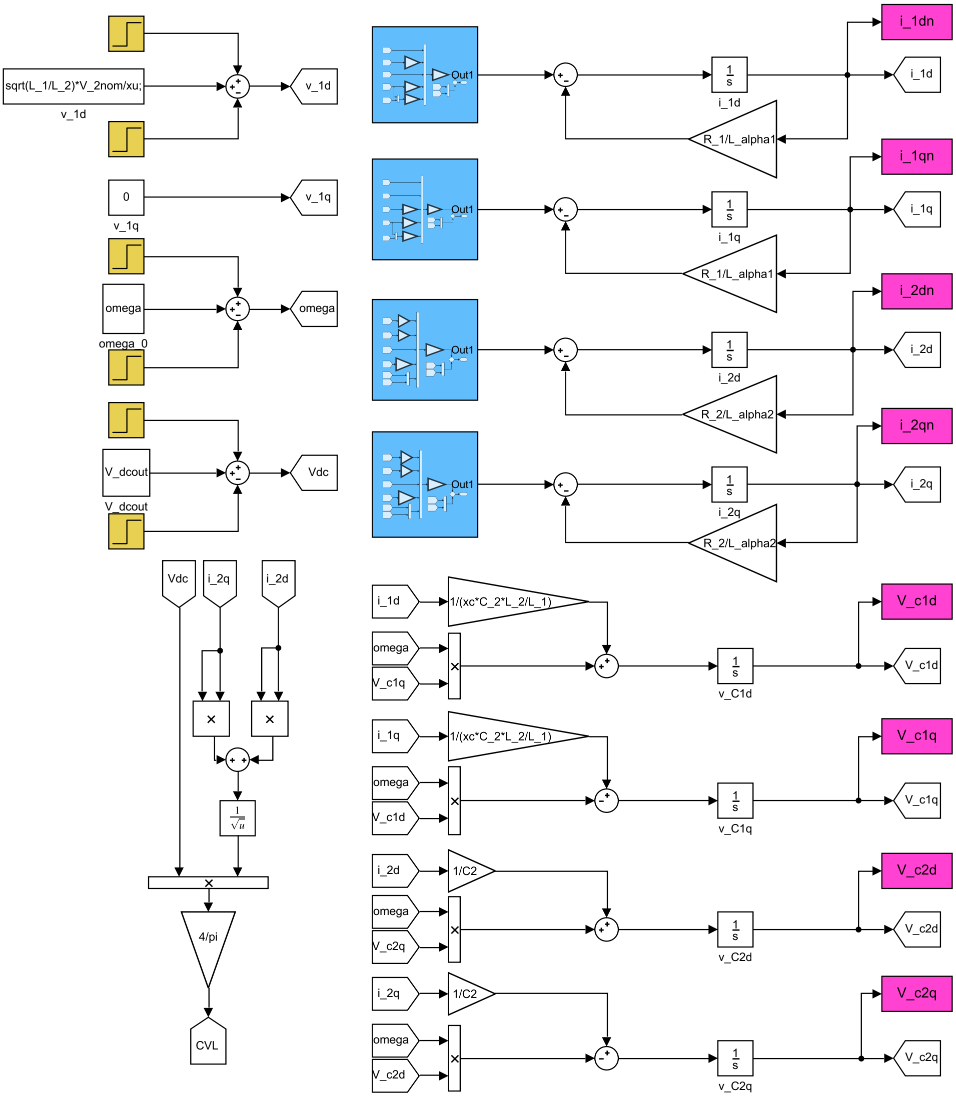

Figure C.3: Nonlinear dq-model.

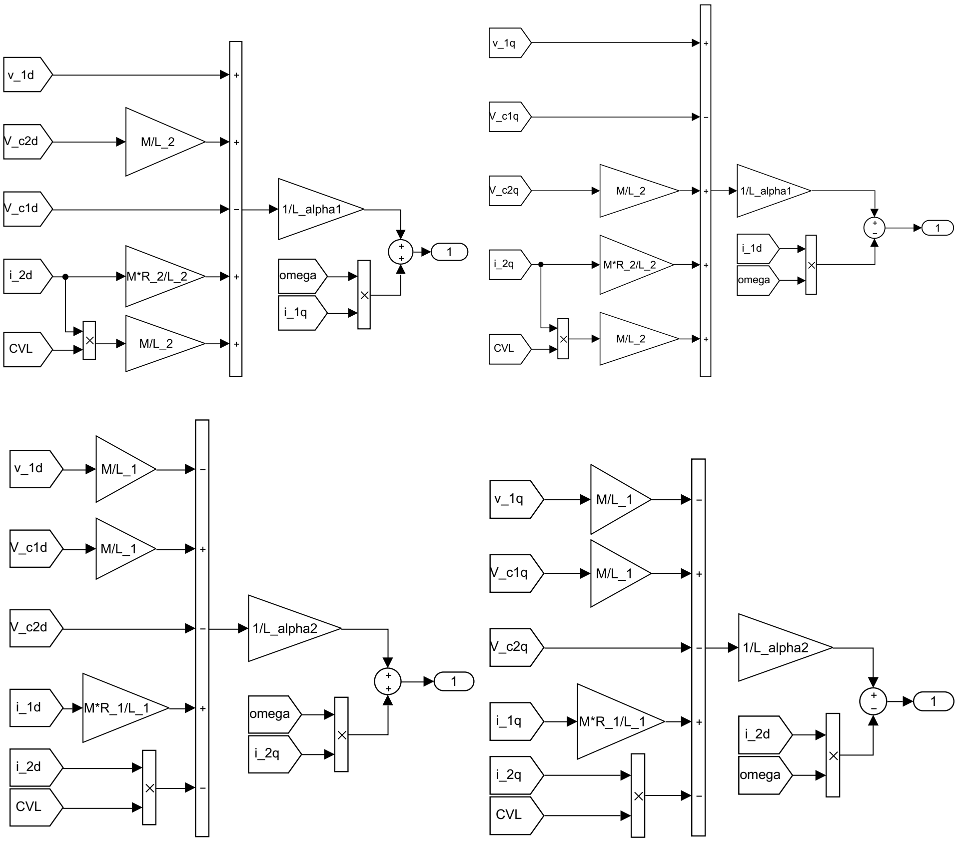

Figure C.4: Subsystem of the nonlinear dq-model.

Figure C.5 shows another implementation of the nonlinear dq-model, this time with a MATLAB-function block. This was done in an early stage in order to validate the model obtained in Figure C.3. Both models exhibits the exact same dynamic behaviour.

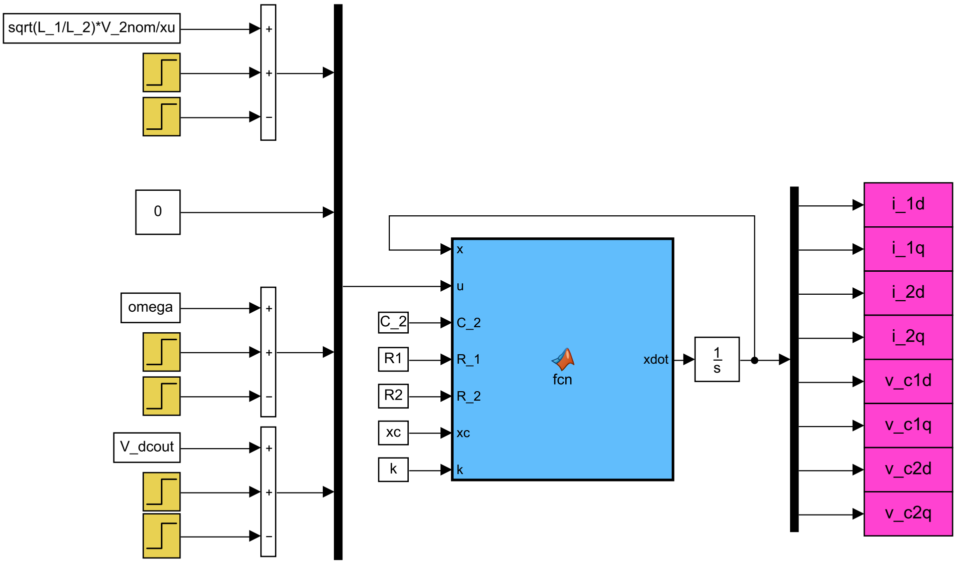

Figure C.5: Nonlinear *dq*-model implemented with MATLAB-function block.

C.3 Small-signal state-space model

Figure C.6 shows the small-signal simulation model.

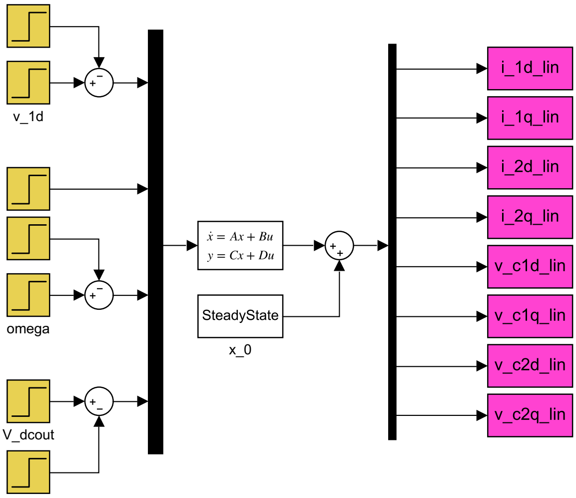

Figure C.6: Small-signal model.

Appendix D

General Expressions

This appendix presents the general complicated expression for the steady-state coil currents $\hat{I}_1$ and $\hat{I}_2$ and the equvalent resistance R_{eq} in the CVL IPT-system.

```
> about(Req)
V2*((-omega^8*V2^2*C1^4*(C2*L2*omega^2-1)^2*L1^4+2*V2^2*C1^3*
omega^6*(C2*L2*omega^2-1)*(C1*C2*M^2*omega^4+2*C2*L2*omega^2-2)*
L1^3-C1^2*omega^4*(C1^2*C2^2*M^4*omega^8*V2^2-C1*omega^4*
(omega^4*C1*C2^2*L2^2*V1^2-6*(C2*V2^2+1/3*C1*V1^2)*C2*omega^2*
L2+6*C2*V2^2+C1*V1^2*(C2^2*R2^2*omega^2+1))*M^2+2*V2^2*(C2*L2*
omega^2-1)^2*(C1^2*R1^2*omega^2+3))*L1^2-2*(omega^8*C1^2*C2*(C1*
C2*L2*V1^2*omega^2-C1*V1^2-C2*V2^2)*M^4-C1*omega^4*(-omega^4*C1*
C2^2*L2^2*V1^2+C2*(C2*(C1^2*R1^2*omega^2+3)*V2^2+2*C1*V1^2)*
omega^2*L2+(-C1^2*R1^2*omega^2-3)*C2*V2^2-C1*V1^2*(C2^2*R2^2*
omega^2+1))*M^2-2*V2^2*(C2*L2*omega^2-1)^2*(C1^2*R1^2*omega^2+1)
)*C1*omega^2*L1+C1^4*C2^2*M^6*V1^2*omega^12+2*C2*C1^2*omega^8*
(omega^2*C1*C2*L2*V1^2-1/2*C2*V2^2+C1*V1^2*(C1*C2*R1*R2*omega^2
-1))*M^4+(omega^4*C1*C2^2*L2^2*V1^2-2*omega^2*C2*(C1*V1^2+C2*
V2^2)*L2+2*C2*V2^2+C1*V1^2*(C2^2*R2^2*omega^2+1))*(C1^2*R1^2*
omega^2+1)*C1*omega^4*M^2-V2^2*(C2*L2*omega^2-1)^2*(C1^2*R1^2*
omega^2+1)^2)^(1/2)+(C1^2*(L1^2*R2+M^2*R1)*omega^4+C1*R2*(C1*
R1^2-2*L1)*omega^2+R2)*V2*C2*omega)/C2/((-C1^2*L1^2*V2^2+C1^2*
M^2*V1^2)*omega^4-V2^2*C1*(C1*R1^2-2*L1)*omega^2-V2^2)/omega:
  nothing known about this object
```

```
> about(I1)
((-omega^8*V2^2*C1^4*(C2*L2*omega^2-1)^2*L1^4+2*V2^2*C1^3*
omega^6*(C2*L2*omega^2-1)*(C1*C2*M^2*omega^4+2*C2*L2*omega^2-2)*
L1^3-C1^2*omega^4*(C1^2*C2^2*M^4*omega^8*V2^2-C1*omega^4*
(omega^4*C1*C2^2*L2^2*V1^2-6*(C2*V2^2+1/3*C1*V1^2)*C2*omega^2*
L2+6*C2*V2^2+C1*V1^2*(C2^2*R2^2*omega^2+1))*M^2+2*V2^2*(C2*L2*
omega^2-1)^2*(C1^2*R1^2*omega^2+3))*L1^2-2*(omega^8*C1^2*C2*(C1*
C2*L2*V1^2*omega^2-C1*V1^2-C2*V2^2)*M^4-C1*omega^4*(-omega^4*C1*
C2^2*L2^2*V1^2+C2*(C2*(C1^2*R1^2*omega^2+3)*V2^2+2*C1*V1^2)*
omega^2*L2+(-C1^2*R1^2*omega^2-3)*C2*V2^2-C1*V1^2*(C2^2*R2^2*
omega^2+1))*M^2-2*V2^2*(C2*L2*omega^2-1)^2*(C1^2*R1^2*omega^2+1)
)*C1*omega^2*L1+C1^4*C2^2*M^6*V1^2*omega^12+2*C2*C1^2*omega^8*
(omega^2*C1*C2*L2*V1^2-1/2*C2*V2^2+C1*V1^2*(C1*C2*R1*R2*omega^2
-1))*M^4+(omega^4*C1*C2^2*L2^2*V1^2-2*omega^2*C2*(C1*V1^2+C2*
V2^2)*L2+2*C2*V2^2+C1*V1^2*(C2^2*R2^2*omega^2+1))*(C1^2*R1^2*
omega^2+1)*C1*omega^4*M^2-V2^2*(C2*L2*omega^2-1)^2*(C1^2*R1^2*
omega^2+1)^2)^(1/2)*V2+(I*C2*L2*M^2*V1^2-I*C2*L1^2*L2*V2^2)*
C1^2*omega^6+M^2*C1^2*C2*(R1*V2^2+R2*V1^2)*omega^5-I*C1*(((C2*
L2*R1^2-L1^2)*V2^2+M^2*V1^2)*C1-2*V2^2*C2*L1*L2)*omega^4+I*V2^2*
(C1^2*R1^2-2*C1*L1-C2*L2)*omega^2+I*V2^2)*C1*omega*V1/(V2*(I*
omega^2*C1*L1+C1*R1*omega-I)*(-omega^8*V2^2*C1^4*(C2*L2*omega^2
-1)^2*L1^4+2*V2^2*C1^3*omega^6*(C2*L2*omega^2-1)*(C1*C2*M^2*
omega^4+2*C2*L2*omega^2-2)*L1^3-C1^2*omega^4*(C1^2*C2^2*M^4*
omega^8*V2^2-C1*omega^4*(omega^4*C1*C2^2*L2^2*V1^2-6*(C2*
V2^2+1/3*C1*V1^2)*C2*omega^2*L2+6*C2*V2^2+C1*V1^2*(C2^2*R2^2*
omega^2+1))*M^2+2*V2^2*(C2*L2*omega^2-1)^2*(C1^2*R1^2*omega^2+3)
)*L1^2-2*(omega^8*C1^2*C2*(C1*C2*L2*V1^2*omega^2-C1*V1^2-C2*
V2^2)*M^4-C1*omega^4*(-omega^4*C1*C2^2*L2^2*V1^2+C2*(C2*(C1^2*
R1^2*omega^2+3)*V2^2+2*C1*V1^2)*omega^2*L2+(-C1^2*R1^2*omega^2
-3)*C2*V2^2-C1*V1^2*(C2^2*R2^2*omega^2+1))*M^2-2*V2^2*(C2*L2*
omega^2-1)^2*(C1^2*R1^2*omega^2+1))*C1*omega^2*L1+C1^4*C2^2*M^6*
V1^2*omega^12+2*C2*C1^2*omega^8*(omega^2*C1*C2*L2*V1^2-1/2*C2*
V2^2+C1*V1^2*(C1*C2*R1*R2*omega^2-1))*M^4+(omega^4*C1*C2^2*L2^2*
V1^2-2*omega^2*C2*(C1*V1^2+C2*V2^2)*L2+2*C2*V2^2+C1*V1^2*(C2^2*
R2^2*omega^2+1))*(C1^2*R1^2*omega^2+1)*C1*omega^4*M^2-V2^2*(C2*
```

```
L2*omega^2-1)^2*(C1^2*R1^2*omega^2+1)^2)^(1/2)+C1^3*C2*(-L1*V2+
M*V1)*(L1*V2+M*V1)*(-L1*L2+M^2)*omega^8+I*C2*C1^3*(L1*R1*(-L1*
L2+M^2)*V2^2+M^2*V1^2*(L1*R2+L2*R1))*omega^7+2*((1/2*L1*(C2*L2*
R1^2-L1^2)*V2^2+1/2*M^2*V1^2*(C2*R1*R2+L1))*C1+C2*((L1*M^2-3/2*
L1^2*L2)*V2^2+1/2*M^2*L2*V1^2))*C1^2*omega^6-I*C1^2*(((C2*L2*
R1^2-L1^2)*V2^2+M^2*V1^2)*R1*C1+(R1*(-2*L1*L2+M^2)*V2^2+M^2*R2*
V1^2)*C2)*omega^5-(V2^2*L1*R1^2*C1^2+((C2*L2*R1^2-3*L1^2)*V2^2+
M^2*V1^2)*C1+V2^2*C2*(-3*L1*L2+M^2))*C1*omega^4+I*V2^2*C1*(C1^2*
R1^2-2*C1*L1-C2*L2)*R1*omega^3+V2^2*(C1^2*R1^2-3*C1*L1-C2*L2)*
omega^2+I*C1*R1*V2^2*omega+V2^2):
  nothing known about this object
```

```
> about(I2)
I*C2*(C1^2*(-L1^2*V2^2+M^2*V1^2)*omega^4-V2^2*C1*(C1*R1^2-2*L1)*
omega^2-V2^2)*M*C1*omega^3*V1/(V2*(I*omega^2*C1*L1+C1*R1*omega-
I)*(-omega^8*V2^2*C1^4*(C2*L2*omega^2-1)^2*L1^4+2*V2^2*C1^3*
omega^6*(C2*L2*omega^2-1)*(C1*C2*M^2*omega^4+2*C2*L2*omega^2-2)*
L1^3-C1^2*omega^4*(C1^2*C2^2*M^4*omega^8*V2^2-C1*omega^4*
(omega^4*C1*C2^2*L2^2*V1^2-6*(C2*V2^2+1/3*C1*V1^2)*C2*omega^2*
L2+6*C2*V2^2+C1*V1^2*(C2^2*R2^2*omega^2+1))*M^2+2*V2^2*(C2*L2*
omega^2-1)^2*(C1^2*R1^2*omega^2+3))*L1^2-2*(omega^8*C1^2*C2*(C1*
C2*L2*V1^2*omega^2-C1*V1^2-C2*V2^2)*M^4-C1*omega^4*(-omega^4*C1*
C2^2*L2^2*V1^2+C2*(C2*(C1^2*R1^2*omega^2+3)*V2^2+2*C1*V1^2)*
omega^2*L2+(-C1^2*R1^2*omega^2-3)*C2*V2^2-C1*V1^2*(C2^2*R2^2*
omega^2+1))*M^2-2*V2^2*(C2*L2*omega^2-1)^2*(C1^2*R1^2*omega^2+1)
)*C1*omega^2*L1+C1^4*C2^2*M^6*V1^2*omega^12+2*C2*C1^2*omega^8*
(omega^2*C1*C2*L2*V1^2-1/2*C2*V2^2+C1*V1^2*(C1*C2*R1*R2*omega^2
-1))*M^4+(omega^4*C1*C2^2*L2^2*V1^2-2*omega^2*C2*(C1*V1^2+C2*
V2^2)*L2+2*C2*V2^2+C1*V1^2*(C2^2*R2^2*omega^2+1))*(C1^2*R1^2*
omega^2+1)*C1*omega^4*M^2-V2^2*(C2*L2*omega^2-1)^2*(C1^2*R1^2*
omega^2+1)^2)^(1/2)+C1^3*C2*(-L1*V2+M*V1)*(L1*V2+M*V1)*(-L1*L2+
M^2)*omega^8+I*C2*C1^3*(L1*R1*(-L1*L2+M^2)*V2^2+M^2*V1^2*(L1*R2+
L2*R1))*omega^7+2*((1/2*L1*(C2*L2*R1^2-L1^2)*V2^2+1/2*M^2*V1^2*
(C2*R1*R2+L1))*C1+C2*((L1*M^2-3/2*L1^2*L2)*V2^2+1/2*M^2*L2*V1^2)
)*C1^2*omega^6-I*C1^2*(((C2*L2*R1^2-L1^2)*V2^2+M^2*V1^2)*R1*C1+
(R1*(-2*L1*L2+M^2)*V2^2+M^2*R2*V1^2)*C2)*omega^5-(V2^2*L1*R1^2*
C1^2+((C2*L2*R1^2-3*L1^2)*V2^2+M^2*V1^2)*C1+V2^2*C2*(-3*L1*L2+
M^2))*C1*omega^4+I*V2^2*C1*(C1^2*R1^2-2*C1*L1-C2*L2)*R1*omega^3+
V2^2*(C1^2*R1^2-3*C1*L1-C2*L2)*omega^2+I*C1*R1*V2^2*omega+V2^2):
  nothing known about this object
>
```

Appendix E

Conference Paper

This appendix presents the paper submitted to the 20th IEEE Workshop on Control and Modeling of Power Electronics, IEEE COMPEL 2019, held in Toronto, Canada from June 17th to June 20th, 2019.

Small-Signal State-Space Analysis of Inductive Battery Charging System in Off-Resonant Operation

Ernst Torsgård[1]
[1] Dept. Engineering Cybernetics
NTNU
Trondheim, Norway
ernstt@stud.ntnu.no

Giuseppe Guidi[2]
[2] SINTEF Energy Research
Trondheim, Norway
Giuseppe.Guidi@sintef.no

Jon Are Suul[1,2]
[1] Dept. Engineering Cybernetics
NTNU
Trondheim, Norway
jon.are.suul@ntnu.no

***Abstract*—This paper analyses the small-signal dynamics of a series-series compensated inductive charging system with a passive diode rectifier interfaced directly to a battery on the receiving side. The analyzed system is designed for utilizing the constant voltage load (CVL) characteristics of the battery to enable power flow control at constant input/output voltages by changing the frequency in response to variations in coupling conditions. A linearizable state-space model, including the nonlinear CVL characteristics, is presented and utilized to evaluate the small-signal dynamics of the studied system. Eigenvalue trajectories and frequency characteristics are presented to show how the small-signal dynamics vary with the coupling conditions and how this will influence controller tuning requirements. Time-domain simulations are presented to verify the validity of the small-signal modelling and to demonstrate the performance of sub-resonant frequency control by a simple PI-controller regulating the power flow in response to variations in the coupling conditions.**

***Index Terms*—Eigenvalue Analysis, Inductive Power Transfer, Nonlinear Time-Invariant State-Space Model, Off-Resonant Operation of Inductive Charging System, Small-Signal Analysis**

I. INTRODUCTION

Inductive power transfer (IPT) technology is currently being widely studied for wireless battery charging of electric vehicles (EVs) [1], [2], [3]. The functionality and operating frequency of such systems are currently being standardized for resonant operation within a narrow frequency band [4]. However, IPT system designs and control strategies relying on variable frequency control have also been proposed [5], and can still be relevant for applications that are not standardized for operation in a narrow frequency range. In addition to specially engineered or customized systems, variable frequency control can, for instance, be relevant for subsea charging systems, [6] or marine transport applications [7], [8].

Most proposed strategies for frequency control of resonant IPT systems are based on increasing the operating frequency when the magnetic coupling is reduced [5]. The system must then be designed so that the power flow at a constant input voltage amplitude is decreased when the frequency is increased beyond the resonance frequency. Thus, such systems are typically designed to operate at resonance with maximum sending side voltage at the highest expected coupling. Frequency control, or dual voltage-frequency control, in the super-resonant region can then be applied for regulating the power flow at lower coupling [5].

A different approach for design and control of series-series (SS) compensated IPT systems intended for off-resonant operation was introduced in [7], [9], [10]. By this approach, the system should be designed for resonant operation with rated input voltage at the minimum coupling condition. The design approach takes advantage of the constant voltage load (CVL) characteristics resulting from a diode rectifier directly interfaced to a battery for enhancing the off-resonant power transfer capability. Thus, the system is operated in the bifurcated region when the magnetic coupling is above the minimum value where the system is designed for rated power flow. This design approach can enable off-resonant control for regulating the power flow over a wide range of coupling conditions with constant input and output voltages, ensuring minimized current rating requirements for the system components [10]. As discussed in [9], [10] designs for power control by sub-resonant operation should be preferred, since this can ensure slightly inductive operation and minimized switching losses for the sending side converter. However, the design approach and the analysis presented in [10] were only based on the steady-state frequency characteristics of the system.

This paper presents a linearizable state-space model of an SS compensated IPT system designed according to the approach from [9], [10], for analyzing the small-signal dynamics and the controller tuning for variable frequency operation. The presented model includes the nonlinearity due to the CVL characteristics of battery charging and allows for accurate assessment of the small-signal dynamics at off-resonant operation over a defined range of variations in the operating conditions. The accuracy of the presented model is verified by time-domain simulations. Furthermore, the eigenvalues and frequency-domain characteristics of the small-signal model are evaluated along the trajectory corresponding to a constant rated power transfer over the full range of expected coupling conditions. The results are utilized to design a simple PI-

The work of SINTEF Energy Research in this paper was supported by the Internal Strategic Institute Project ”Innovative Power Transfer Transfer Technology for Electric Transportation (IPT-ElTra) financed by the national Basic Funding Scheme of Norway.

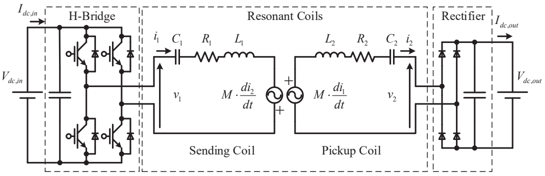

Fig. 1. Series-series compensated IPT system with constant voltage load

controller for regulating the power transfer for battery charging in response to variations in operating conditions.

II. DESIGN OF SS COMPENSATED IPT SYSTEMS FOR OFF-RESONANT OPERATION WITH CVL

The studied configuration is an SS compensated IPT system, as shown in Fig. 1, with an H-bridge converter on the sending side and a diode rectifier interfaced directly to a battery on the receiving side, as represented by a voltage source.

A. Dynamic model with time-periodic variables

The state equations for the configuration in Fig. 1 can be expressed directly from the circuit diagram as:

$$\begin{cases} v_1 = v_{C1} + R_1 i_1 + L_1 \dfrac{di_1}{dt} - M\dfrac{di_2}{dt} \\ v_2 = M\dfrac{di_1}{dt} - L_2\dfrac{di_2}{dt} - R_2 i_2 - v_{C2} \\ \dfrac{dv_{C_1}}{dt} = \dfrac{1}{C_1} i_1 \\ \dfrac{dv_{C_2}}{dt} = \dfrac{1}{C_2} i_2 \end{cases} \tag{1}$$

Assuming sinusoidal currents and introducing a first harmonic approximation of the voltage v_2 at the terminals of the diode rectifier, the CVL characteristics can be modelled by:

$$v_2 = \frac{i_2}{I_2} \cdot \frac{4}{\pi} \cdot V_{dc,out} \tag{2}$$

In this equation I_2 represents the amplitude of i_2. Thus, the amplitude of the first harmonic voltage component at the receiving side is determined by the dc output voltage while the characteristics of the diode rectifier impose that the voltage will be in phase with the receiving side current. As will be shown in the following, the nonlinearity introduced by the constant dc voltage in combination with the diode rectifier significantly influences the frequency characteristics and the small-signal dynamics of the system.

B. Frequency characteristics of CVL IPT systems with impact of unbalancing and detuning

Representing the fundamental frequency currents and voltages in (1) and (2) by phasor variables, it is possible to derive the steady-state frequency characteristics (i.e. with $d/dt = j\omega$) of the power transfer capability of the studied system with CVL characteristics, as explained in [10]. The power transfer capability and phase angle of the equivalent impedance for an ideal lossless case is given by the black curves in Fig. 2.

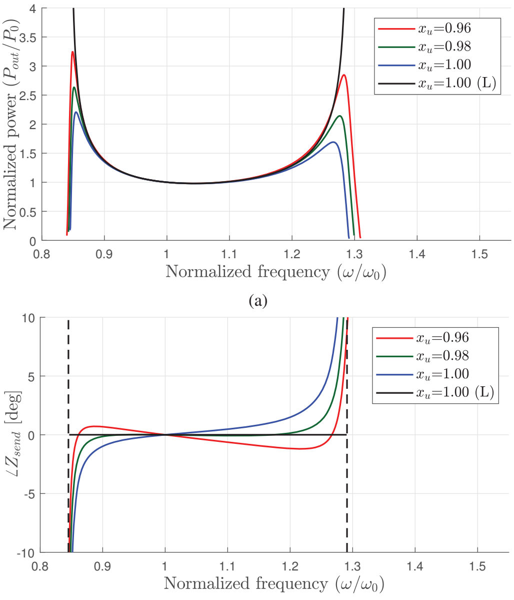

(a)

(b)

Fig. 2. Effect of unbalancing: ”L” denotes a lossless system , coils with coupling factor $k = \frac{M}{\sqrt{L_1 L_2}} = 0.4$, $\omega_0 = \frac{1}{\sqrt{C_1 L_1}} = \frac{1}{\sqrt{C_2 L_2}}$, $Q_1 = 310$ and $Q_2 = 270$. Power is normalized to $P_0 = P(k, x_u, x_c, \omega_0)$.

These curves show that the power transfer capability with CVL characteristics are ideally approaching infinite when reducing or increasing the frequency from the resonance frequency, while the phase angle of the equivalent impedance is zero in the full range of feasible operating conditions. In a practical circuit, the losses will limit the maximum power transfer capability as shown by the blue curve in Fig. 2a. Still, the figure shows how the CVL characteristics will cause two pronounced peaks in the power transfer and Fig. 2b shows that the phase angle of the equivalent impedance will be close to zero in a large share of the frequency range between these two peaks.

In [9] and [10], it is shown how the off-resonant peaks in the power transfer characteristics of a system with CVL characteristics can be enhanced by introducing an unbalance factor x_u defined by:

$$x_u^2 \cdot \frac{L_2}{L_1} = \left(\frac{V_2}{V_1}\right)^2, \quad 0 < x_u \leq 1 \tag{3}$$

The result of reducing x_u is shown by the green and red curves in in Fig. 2. As demonstrated by Fig. 2a, unbalancing of the voltage or inductance ratios can be utilized to enhance the off-resonant peaks in the power transfer capability. The curves in Fig. 2b also show how unbalancing enhances the bifurcation in the phase characteristics.

To further shape the frequency characteristics, a detuning factor x_c, [10], can be introduced as given by (4):

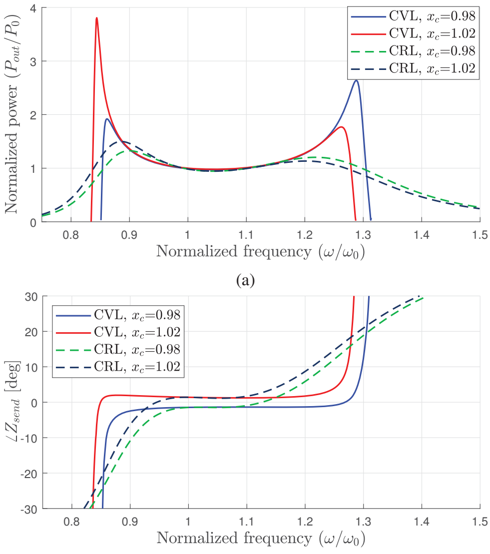

(a)

(b)

Fig. 3. Effect of detuning and comparison between CVL and CRL. Coils with coupling factor $k = 0.4$ as in Fig. 2 and unbalance factor $x_u = 0.98$. Power is normalized to $P_0 = P(k, x_u, x_c, \omega_0)$.

$$x_c = \frac{C_1 \cdot L_1}{C_2 \cdot L_2} \tag{4}$$

As a result of such detuning, the system will no longer have a single defined resonance frequency, i.e. $\omega_0 = \omega_{2,0} = \frac{1}{\sqrt{C_2 L_2}} \neq \frac{1}{\sqrt{C_1 L_1}} = \omega_{1,0}$. By selecting values for x_c above or below 1.0, either the sub- or super-resonant peak in power transfer characteristics, respectively, can be enhanced. Fig. 3 shows how this affects the frequency characteristics of a system with CVL compared to a case with a constant resistive load (CRL). Clearly, a small amount of detuning will more strongly enhance the sub- or super-resonant power peaks in the CVL case than for the CRL case. Furthermore, the effect of detuning on the phase characteristics is shown in Fig. 3b. This figure shows how a detuning factor of $x_c > 1$ ensures a slightly inductive sending side impedance over the whole frequency range of interest, whereas a factor of $x_c < 1$ implies a slightly capacitive impedance. The figure also shows that the CVL leads to an almost constant phase angle close to zero in a much wider frequency range than for the CRL.

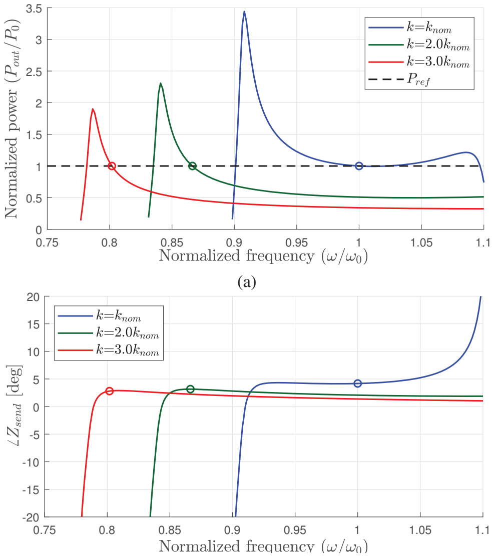

(a)

(b)

Fig. 4. Operation with constant power transfer at variable coupling: operating points marked with a circle. Coils with unbalance factor $x_u = 0.98$, detuning factor $x_c = 1.03$, nominal coupling factor $k_{nom} = 0.2$. Power normalized to $P_0 = P(k_{nom}, x_u, x_c, \omega_0)$.

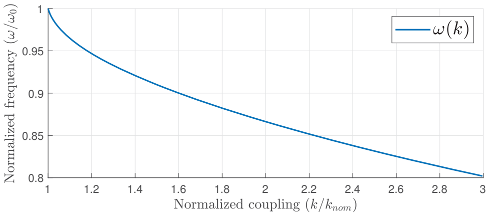

Fig. 5. Required operating frequency as function of coupling factor for maintaining constant power transfer with sub-resonant frequency control.

C. Off-resonant operation for power flow control

The introduction of unbalancing and detuning of the SS IPT system with CVL allows for maintaining high power transfer capability in a wide range of coupling conditions by utilizing off-resonant operation. Thus, the power transfer can be kept constant by regulating the operating frequency in response to changes in the coupling conditions [10]. An example of such operation is illustrated by the frequency characteristics of the IPT system for three different values of k in Fig. 4. As indicated by Fig. 4b, the equivalent sending side impedance will remain slightly inductive over the whole frequency range, which will help to minimize switching losses of the sending side H-bridge converter. Since the operating strategy given by Fig. 4 is obtained with constant input and output voltage and a phase angle of the sending side equivalent impedance close to zero, the current amplitude will also remain almost constant over the full range of expected operating conditions. Thus, contrary to systems operating at the resonance frequency, IPT systems designed and controlled according to the approach from [9], [10] avoids the need for increasing the current rating of components proportionally to the expected variations in the coupling coefficient.

The required variations in the frequency as a function of the coupling conditions are shown in Fig. 5. It can be noticed from Fig. 4a and Fig. 5 that the sensitivity of the power flow to the frequency will change significantly with the coupling conditions. Thus, it will be important to evaluate the small-signal dynamics of the system for designing a suitable control loop to regulate the power flow by changing the frequency.

III. TIME-INVARIANT STATE-SPACE MODELLING OF SS COMPENSATED ITP SYSTEMS WITH CVL

For utilizing state-space modelling techniques to analyze the small-signal characteristics of the studied system, a time-invariant and linearizable model is needed. Such models can be obtained by dq-frame representation or dynamic phasor-based modeling [11]. Such modelling approaches have been studied for various IPT systems, for instance by [12], [13], [14], [15]. However, the following analysis will specifically address the nonlinearity of CVL characteristics and the off-resonant operation according to Fig. 4 and Fig. 5.

A. Nonlinear state-space model

As mentioned, CVL characteristics introduce nonlinearity in the receiving side. Assuming a dq-frame representation of the state variables in a first harmonic approximation, the nonlinearity from (2) can be represented by (5) [16]:

$$v_{2,dq} = \frac{i_{2,dq}}{|i_{2,dq}|} \cdot \frac{4}{\pi} \cdot V_{dc,out} = \frac{i_{2,dq}}{\sqrt{i_{2,d}^2 + i_{2,q}^2}} \cdot \frac{4}{\pi} \cdot V_{dc,out} \tag{5}$$

Thus, a nonlinear model can be derived by dq-frame representation of all state variables from (1), and can be expressed on the general state-space form given by:

$$\dot{\boldsymbol{x}} = \boldsymbol{f}(\boldsymbol{x}, \boldsymbol{u}), \quad \boldsymbol{y} = \boldsymbol{g}(\boldsymbol{x}, \boldsymbol{u}) \tag{6}$$

with the states $\boldsymbol{x}$, input signals $\boldsymbol{u}$ and output $\boldsymbol{y}$ defined by:

$$\begin{aligned} \boldsymbol{x} &= \begin{bmatrix} i_{1,d} & i_{1,q} & i_{2,d} & i_{2,q} & v_{C1,d} & v_{C1,q} & v_{C2,d} & v_{C2,q} \end{bmatrix}^T \\ \boldsymbol{u} &= \begin{bmatrix} v_{1,d} & v_{1,q} & \omega & V_{dc,out} \end{bmatrix}^T \\ \boldsymbol{y} &= \begin{bmatrix} P_{in} \\ P_{out} \end{bmatrix} = \begin{bmatrix} v_{1,d} \cdot i_{1,d} + v_{1,q} \cdot i_{1,q} \\ v_{2,d} \cdot i_{2,d} + v_{2,q} \cdot i_{2,q} \end{bmatrix} \end{aligned} \tag{7}$$

Introducing the leakage factors $L_{\alpha 1} = L_1 - M^2/L_2$ and $L_{\alpha 2} = L_2 - M^2/L_1$, the resulting nonlinear state-space model can be derived as given by (8). This model can be linearized at any equilibrium point corresponding to a feasible operating condition of the system. Accordingly, the small-signal dynamics around the steady-state operating point defined by $\boldsymbol{f(x_0, u_0) = 0}$ can be studied by evaluating the eigenvalues of the $\boldsymbol{A}$-matrix when the system is expressed on the general linearized state-space form according to (9). The $\boldsymbol{A}, \boldsymbol{B}$ and $\boldsymbol{C}$ matrices resulting from linearization of the studied system can be expressed by (10), (11) and (12), respectively. The elements $A_{i,j}$ and $B_{i,j}$ in (10) and (11) are given by (13). For these expressions, dq-subscripts indicate that $i_{2,d,0}$ and $i_{2,q,0}$ should be used in the first and second element, respectively, and the ±-sign indicates a positive and negative value for the corresponding first and second matrix entry.

$$\begin{aligned}
\frac{di_{1,d}}{dt} &= \omega \cdot i_{1,q} - \frac{R_1}{L_{\alpha 1}} \cdot i_{1,d} - \frac{MR_2}{L_{\alpha 1} L_2} \cdot i_{2,d} - \frac{1}{L_{\alpha 1}} \cdot v_{C1,d} \\
&- \frac{M}{L_{\alpha 1} L_2} \cdot v_{C2,d} + \frac{1}{L_{\alpha 1}} \cdot v_{1,d} - \frac{M}{L_{\alpha 1} L_2} \cdot \frac{i_{2,d}}{\sqrt{i_{2,d}^2 + i_{2,q}^2}} \cdot \frac{4}{\pi} \cdot V_{dc,out} \\
\frac{di_{1,q}}{dt} &= -\omega \cdot i_{1,d} - \frac{R_1}{L_{\alpha 1}} \cdot i_{1,q} - \frac{MR_2}{L_{\alpha 1} L_2} \cdot i_{2,q} - \frac{1}{L_{\alpha 1}} \cdot v_{C1,q} \\
&- \frac{M}{L_{\alpha 1} L_2} \cdot v_{C2,q} + \frac{1}{L_{\alpha 1}} \cdot v_{1,q} - \frac{M}{L_{\alpha 1} L_2} \cdot \frac{i_{2,q}}{\sqrt{i_{2,d}^2 + i_{2,q}^2}} \cdot \frac{4}{\pi} \cdot V_{dc,out} \\
\frac{di_{2,d}}{dt} &= \omega \cdot i_{2,q} - \frac{MR_1}{L_{\alpha 2} L_1} \cdot i_{1,d} - \frac{R_2}{L_{\alpha 2}} \cdot i_{2,d} - \frac{M}{L_{\alpha 2} L_1} \cdot v_{C1,d} \\
&- \frac{1}{L_{\alpha 2}} \cdot v_{C2,d} + \frac{M}{L_{\alpha 2} L_1} \cdot v_{1,d} - \frac{1}{L_{\alpha 2}} \cdot \frac{i_{2,d}}{\sqrt{i_{2,d}^2 + i_{2,q}^2}} \cdot \frac{4}{\pi} \cdot V_{dc,out} \\
\frac{di_{2,q}}{dt} &= -\omega \cdot i_{2,d} - \frac{MR_1}{L_{\alpha 2} L_1} \cdot i_{1,q} - \frac{R_2}{L_{\alpha 2}} \cdot i_{2,q} - \frac{M}{L_{\alpha 2} L_1} \cdot v_{C1,q} \\
&- \frac{1}{L_{\alpha 2}} \cdot v_{C2,q} + \frac{M}{L_{\alpha 2} L_1} \cdot v_{1,q} - \frac{1}{L_{\alpha 2}} \cdot \frac{i_{2,q}}{\sqrt{i_{2,d}^2 + i_{2,q}^2}} \cdot \frac{4}{\pi} \cdot V_{dc,out} \\
\frac{dv_{C1,d}}{dt} &= \omega \cdot v_{C1,q} + \frac{1}{C_1} \cdot i_{1,d} \\
\frac{dv_{C1,q}}{dt} &= -\omega \cdot v_{C1,d} + \frac{1}{C_1} \cdot i_{1,q} \\
\frac{dv_{C2,d}}{dt} &= \omega \cdot v_{C2,q} + \frac{1}{C_2} \cdot i_{2,d} \\
\frac{dv_{C2,q}}{dt} &= -\omega \cdot v_{C2,d} + \frac{1}{C_2} \cdot i_{2,q}
\end{aligned} \tag{8}$$

$$\begin{aligned} \Delta \dot{\boldsymbol{x}} &= \boldsymbol{A}(\boldsymbol{x}_0, \boldsymbol{u}_0) \cdot \Delta \boldsymbol{x} + \boldsymbol{B}(\boldsymbol{x}_0, \boldsymbol{u}_0) \cdot \Delta \boldsymbol{u} \\ \Delta \boldsymbol{y} &= \boldsymbol{C}(\boldsymbol{x}_0, \boldsymbol{u}_0) \cdot \Delta \boldsymbol{x} \end{aligned} \tag{9}$$

$$\boldsymbol{A} = \begin{bmatrix}
\frac{-R_1}{L_{\alpha 1}} & \omega_0 & A_{1,3} & A_{1,4} & \frac{-1}{L_{\alpha 1}} & 0 & \frac{-M}{L_{\alpha 1} L_2} & 0 \\
-\omega_0 & \frac{-R_1}{L_{\alpha 1}} & A_{2,3} & A_{2,4} & 0 & \frac{-1}{L_{\alpha 1}} & 0 & \frac{-M}{L_{\alpha 1} L_2} \\
\frac{-MR_1}{L_{\alpha 2} L_1} & 0 & A_{3,3} & A_{3,4} & \frac{-M}{L_{\alpha 2} L_1} & 0 & \frac{-1}{L_{\alpha 2}} & 0 \\
0 & \frac{-MR_1}{L_{\alpha 2} L_1} & A_{4,3} & A_{4,4} & 0 & \frac{-M}{L_{\alpha 2} L_1} & 0 & \frac{-1}{L_{\alpha 2}} \\
\frac{1}{C_1} & 0 & 0 & 0 & 0 & \omega_0 & 0 & 0 \\
0 & \frac{1}{C_1} & 0 & 0 & -\omega_0 & 0 & 0 & 0 \\
0 & 0 & \frac{1}{C_2} & 0 & 0 & 0 & 0 & \omega_0 \\
0 & 0 & 0 & \frac{1}{C_2} & 0 & 0 & -\omega_0 & 0
\end{bmatrix} \tag{10}$$

$$\boldsymbol{B} = \begin{bmatrix}
\frac{1}{L_{\alpha 1}} & 0 & i_{1,q,0} & B_{1,4} \\
0 & \frac{1}{L_{\alpha 1}} & -i_{1,d,0} & B_{2,4} \\
\frac{M}{L_{\alpha 2} L_1} & 0 & i_{2,q,0} & B_{3,4} \\
0 & \frac{M}{L_{\alpha 2} L_1} & -i_{2,d,0} & B_{4,4} \\
0 & 0 & v_{C1,q,0} & 0 \\
0 & 0 & -v_{C1,d,0} & 0 \\
0 & 0 & v_{C2,q,0} & 0 \\
0 & 0 & -v_{C2,d,0} & 0
\end{bmatrix} \tag{11}$$

$$\boldsymbol{C} = \begin{bmatrix}
v_{1,d,0} & v_{1,q,0} & 0 & 0 & 0 & 0 & 0 & 0 \\
0 & 0 & \frac{4 \cdot i_{2,d,0} \cdot V_{dc,out,0}}{\pi \sqrt{i_{2,d,0}^2 + i_{2,q,0}^2}} & \frac{4 \cdot i_{2,q,0} \cdot V_{dc,out,0}}{\pi \sqrt{i_{2,d,0}^2 + i_{2,q,0}^2}} & 0 & 0 & 0 & 0
\end{bmatrix} \tag{12}$$

TABLE I
PARAMETERS OF SIMULATED IPT-SYSTEM

Nominal power, P_0	10 kW
Nominal operating frequency, f_0	85 kHz
Nominal coupling factor, k	0.2
Primary coil	
Nominal voltage, V_1	380 V
Self-inductance, L_1	176 μH
Quality factor, Q_1	310
Secondary coil	
Nominal voltage, V_2	235 V
Self-inductance, L_2	41 μH
Quality factor, Q_2	270

$$
\begin{aligned}
A_{2,4} = A_{1,3} &= -\frac{M}{L_{\alpha1}L_2}\left(R_2 + \frac{4\cdot i^2_{2,dq,0}\cdot V_{dc,out,0}}{\pi(i^2_{2,d,0}+i^2_{2,q,0})^{3/2}}\right)\\
A_{1,4} = A_{2,3} &= -\frac{4MV_{dc,out,0}}{\pi L_{\alpha1}L_2}\frac{i_{2,d,0}\cdot i_{2,q,0}}{(i^2_{2,d,0}+i^2_{2,q,0})^{3/2}}\\
A_{3,3} = A_{4,4} &= -\frac{1}{L_{\alpha2}}\left(R_2 + \frac{4\cdot i^2_{2,dq,0}\cdot V_{dc,out,0}}{\pi(i^2_{2,d,0}+i^2_{2,q,0})^{3/2}}\right)\\
A_{3,4} = A_{4,3} &= \pm\omega_0 - \frac{4V_{dc,out,0}}{\pi L_{\alpha2}}\frac{i_{2,d,0}\cdot i_{2,q,0}}{(i^2_{2,d,0}+i^2_{2,q,0})^{3/2}}\\
B_{1,4} = B_{2,4} &= -\frac{4M}{\pi L_{\alpha1}L_2}\frac{i_{2,dq,0}}{\sqrt{i^2_{2,d,0}+i^2_{2,d,0}}}\\
B_{3,4} = B_{3,4} &= -\frac{4}{\pi L_{\alpha2}}\frac{i_{2,dq,0}}{\sqrt{i^2_{2,d,0}+i^2_{2,q,0}}}
\end{aligned}
\tag{13}
$$

B. Model verification

The validity and accuracy of the nonlinear state-space model defined by (8) and the corresponding linearized model defined by (9)-(13) is validated by time-domain simulations in the MATLAB/Simulink/Simscape environment, using the parameters in Table I. As the validity of a similar model representing a system operated at its resonance frequency is demonstrated in [16], only examples with off-resonant operation are presented in the following. For the simulations shown in Fig. 6, the system is first linearized at steady-state operation in a condition close to the nominal coupling, with slightly sub-resonant frequency for maintaining nominal power transfer. A step change of 10% in the input voltage is applied at t = 2 ms, and after steady-state operation is achieved, a similar step change in the receiving side voltage is applied at t = 2.4 ms. After reaching steady-state operation with these conditions, the system is brought back to the linearization point at t = 2.8 ms. The dynamic responses of the sending and receiving side currents resulting from the circuit model in Fig. 1, the nonlinear state-space model from (8) and the corresponding linearized model, are shown in the same plots for comparison.

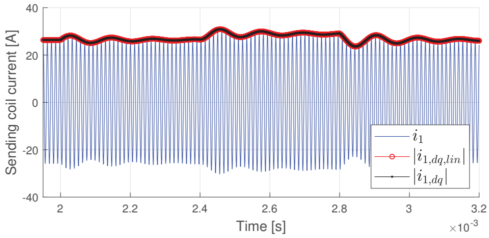

(a) Sending side currents.

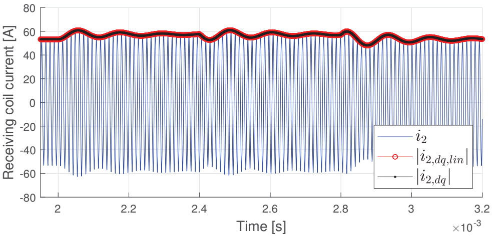

(b) Receiving side currents.

Fig. 6. Comparison of the current dynamics for the simulated models along the constant power trajectory. Simulation point $k = 1.02k_{nom}$, $\omega = 0.988\omega_0$.

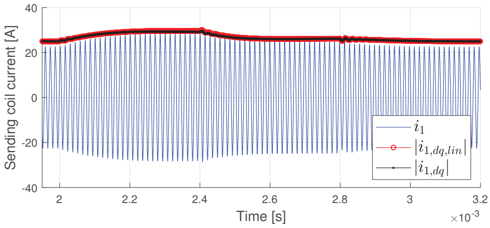

(a) Sending side currents.

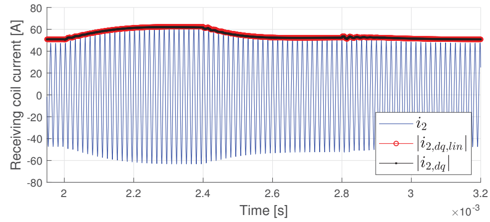

(b) Receiving side currents.

Fig. 7. Comparison of the current dynamics for the simulated models along the constant power trajectory. Simulation point $k = 2.6k_{nom}$, $\omega = 0.827\omega_0$.

The same sequence is repeated for a relatively high coupling coefficient and a correspondingly reduced frequency in Fig. 7. The results show that both the nonlinear and linearized state-space models accurately capture the dynamics of the system along the constant power trajectory illustrated in Fig. 5.

To further document the validity of the presented state-space models, additional time-domain simulations are presented in

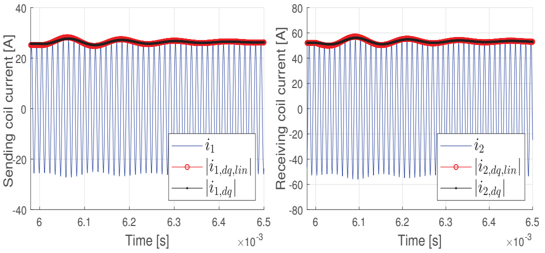

(a) (b)

Fig. 8. Comparison of the current dynamics for the simulated models along the constant power trajectory. Simulation point $k = 1.02k_{nom}$, $\omega = 0.988\omega_0$.

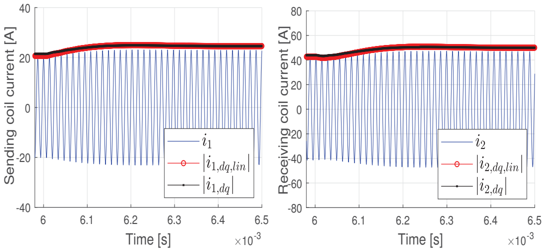

(a) (b)

Fig. 9. Comparison of the current dynamics for the simulated models along the constant power trajectory. Simulation point $k = 2k_{nom}$, $\omega = 0.866\omega_0$.

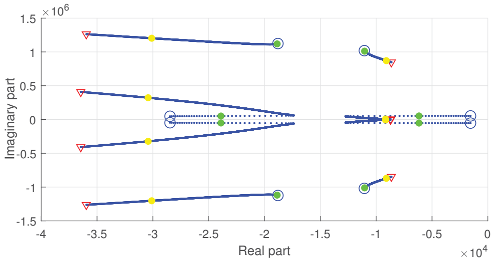

Fig. 10. Eigenvalue trajectory for variation of k in the range $k_{nom} \leq k \leq 3k_{nom}$ with frequency control for maintaining constant power: points market with blue circles correspond to $k = k_{nom}$ and points marked with red triangles corresponds to $k = 3k_{nom}$. Operating points in Fig. 6 and Fig. 7 are marked with green and yellow circles, respectively.

Fig. 8 and Fig. 9, illustrating how the system behaves in response to a step change in the operating frequency. For the simulations presented in Fig. 8, the small-signal model is obtained at the same operating point as in Fig. 6. The system is first at steady-state conditions with an operating frequency of 10 700 rad/s higher than the frequency where the system is linearized, before a step back to the linearization point is applied at t = 6 ms. A similar sequence is repeated in another point along the frequency trajectory in Fig. 5 and the results are shown in Fig. 9, this time with a step change of 5 350 rad/s. From 8a, a slight deviation can be observed, indicating that the accuracy of the small-signal model is sensitive to changes in the operating frequency. However, the oscillation frequency and settling time are virtually identical, demonstrating that the small-signal model provides accurate results as long as it is operated close to the linearization point.

IV. ANALYSIS OF SYSTEM DYNAMICS AND CONTROL

The linearized model from (9)-(13) can be utilized to evaluate the small-signal dynamics of the system and to design suitable control loops for regulating the power transfer.

A. Eigenvalue analysis

The change in the eigenvalues of the $\boldsymbol{A}$-matrix when the coupling conditions are changed in the range of $k_{nom} \leq k \leq 3k_{nom}$ while ensuring constant power transfer by operating on the frequency trajectory from Fig. 5 is shown in Fig. 10. The figure also shows the operating points used for the time-domain simulations in Fig. 6 and Fig. 7, which are marked with green and yellow circles, respectively. As seen from the figure, the system will have a dominant pole-pair with relatively low oscillation frequency and long settling time when operating close to the nominal coupling. The corresponding oscillation mode is clearly seen in the time-domain results in Fig. 6 and Fig. 8. The real part of this dominating pole-pair rapidly decreases when the operating frequency is moved away from the resonance frequency along the trajectory from Fig. 5. However, a sudden change in the movement of these eigenvalues appears around an operating condition with coupling factor $k \approx 1.04k_{nom}$ and operating frequency $\omega \approx 0.98\omega_0$. For an increased coupling coefficient beyond this point, the imaginary part of the dominant eigenvalues decreases while the real part increases when the operating frequency is reduced, making the system more damped but slower. The corresponding differences in system dynamics for close to nominal coupling compared to high coupling conditions are also clearly seen from the simulated responses in Fig. 6 and Fig. 7 or Fig. 8 and Fig. 9, respectively.

B. Power controller design

The small-signal state-space model from (9)-(13) can also be utilized to extract the input-output frequency domain characteristics of the system and to support frequency domain design of control loops. In order to regulate the power transfer in response to variations in the coupling conditions according to the strategy defined by Fig. 4 and Fig. 5, a simple PI-controller can be utilized to change the operating frequency [9]. For explicit regulation of the power provided to the load, it would be necessary to use the received power P_{out} as the feedback signal. However, this would imply the need for feedback across the air gap of the wireless power transfer. Thus, it would be preferable to use only feedback signals from the sending side to regulate the power transfer.

Assuming power control by a PI-controller, the open loop transfer functions for control loops based on feedback from

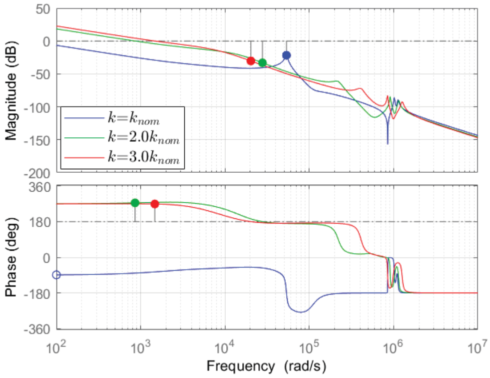

Fig. 11. Frequency response of open loop transfer function from P_{ref} to P_{in} for three different coupling conditions.

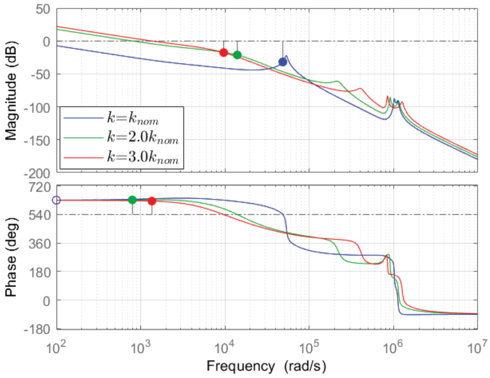

Fig. 12. Frequency response of open loop transfer function from P_{ref} to P_{out} for three different coupling conditions.

either the sending side power P_{in} or the receiving side power P_{out} can be expressed as:

$$\frac{P_{in}}{P_{ref}}(s) = h_r h_{p1} h_f(s) = k_p \frac{1+T_i s}{T_i s} h_{p1}(s) \frac{1}{1+T_f s} \tag{14}$$

$$\frac{P_{out}}{P_{ref}}(s) = h_r h_{p2} h_f(s) = k_p \frac{1+T_i s}{T_i s} h_{p2}(s) \frac{1}{1+T_f s} \tag{15}$$

In these equations, $h_{p1}(s)$ and $h_{p2}(s)$ are the transfer functions from the small-signal frequency input to P_{in} and P_{out}, respectively. Additionally, the open loop transfer functions include the assumed PI-controller $h_r(s)$ and a low-pass filter $h_f(s)$ with time constant $T_f = 100/2\pi f_0$ for extracting the average value of the single-phase power flow. The frequency characteristics of the two open loop transfer functions in (14) and (15) are shown for three different coupling conditions in Fig. 11 and Fig. 12, respectively.

In order to achieve robust closed-loop performance over the whole variation range $k_{nom} \leq k \leq 3k_{nom}$, the general frequency characteristics in Fig. 11 and Fig. 12 are utilized to design the PI-controller parameters such that no overshoot or oscillations occur at operating conditions where the system dynamics are fast. The resulting parameters are selected to be $k_p = -0.65057$ and $T_i = 1/2846$, and the corresponding amplitude- and phase-margins with the different feedback signals are indicated in Fig. 11 and Fig. 12. However, the design for damped response in all coupling conditions implies a relative slow response close to the nominal coupling.

To illustrate the performance when using only sending side power feedback for the control, results from operating the system with the simple control loop in Fig. 13 is shown in Fig. 14. The sequence of ideal steps applied in the coupling factor is shown in Fig. 14a while Fig. 14b shows the resulting

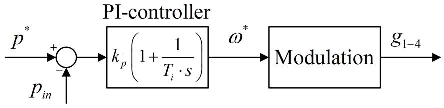

Fig. 13. Power controller for off-resonant operation by sending side feedback.

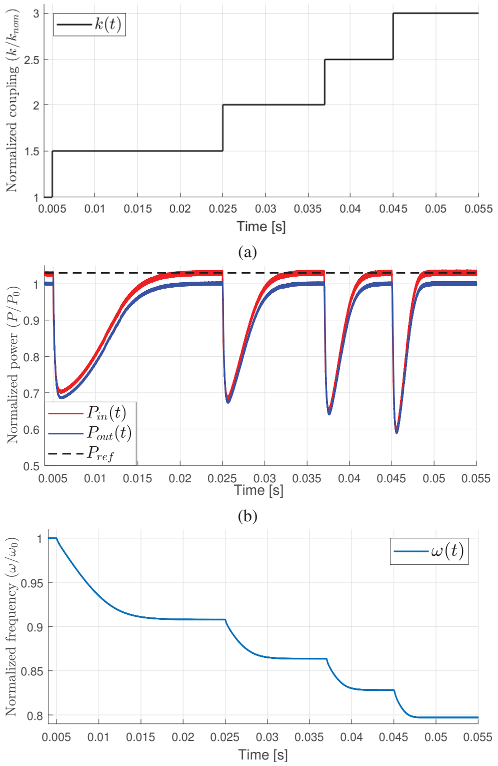

(a)

(b)

(c)

Fig. 14. Closed-loop response to step changes in coupling factor with feedback of sending side power. The sending side power reference is adjusted to compensate for the efficiency of the system.

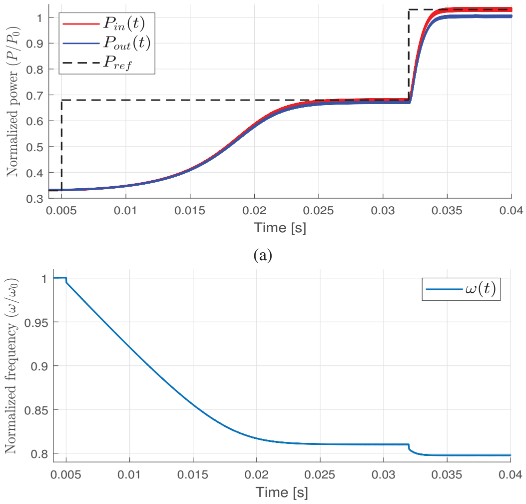

(a)

(b)

Fig. 15. Response to steps in the power reference with control based only on sending side feedback.

output power. As indicated by the figure, the power reference is increased slightly above 1.0 to compensate for the losses in the system. The operating frequency resulting as output from the PI-controller in Fig. 13 is shown in Fig. 14c. As can be seen, the response is much faster in the case of high coupling coefficient, which is expected when considering the frequency trajectory in Fig. 5 and the frequency characteristics in Fig. 12. The results also confirm how the operating frequency resulting from the closed-loop controller corresponds to the trajectory for maintaining nominal power according to 5.

Another example of the closed-loop power control performance is shown in Fig. 15. In this case, the system is initially operating at the secondary side resonance frequency according to the red curve in Fig. 4a with $k = 3k_{knom}$ and a correspondingly low power reference of 0.32 pu. A step in the sending side power reference to 0.66 pu is applied at t = 5 ms, and a second step in the power reference is applied at t = 32 ms, bringing the system to the operating point corresponding to nominal power transfer indicated by the red circle in Fig. 4a. The operating frequency resulting from the PI-controller is shown in Fig. 15b. The results clearly illustrate how the response is stable and well damped over the entire operating region, although much faster when approaching operation at rated power at high coupling.

V. CONCLUSION

This paper has presented a time-invariant state-space model of a Series-Series (SS) compensated Inductive Power Transfer (IPT) system designed for battery charging with minimized component ratings. The evaluated system is intended for power flow control by off-resonant operation during variations in the coupling conditions, which is obtained by utilizing the bifurcated characteristics of the IPT system to allow for frequency control with constant input and output voltages. The presented model accurately represents the influence of the Constant Voltage Load (CVL) characteristics resulting from a receiving side diode rectifier directly interfaced to the battery. The linearized state-space model is utilized to evaluate the small-signal dynamics over the full range of expected operating conditions. This small-signal analysis is also utilized to design a simple but robust PI-controller, which can operate with only sending side feedback for regulating the power flow in response to variations in the coupling conditions.

REFERENCES

[1] C. T. Rim and C. Mi, *Wireless power transfer for electric vehicles and mobile devices*. John Wiley & Sons, 2017.

[2] G. A. Covic and J. T. Boys, “Modern trends in inductive power transfer for transportation applications,” *IEEE Journal of Emerging and Selected topics in power electronics*, vol. 1, no. 1, pp. 28–41, 2013.

[3] S. Li and C. C. Mi, “Wireless power transfer for electric vehicle applications,” *IEEE journal of emerging and selected topics in power electronics*, vol. 3, no. 1, pp. 4–17, 2014.

[4] “Wireless power transfer for light-duty plug-in/electric vehicles and alignment methodology,” SAE Recommended Practice, International J2954 Taskforce, 2019.

[5] R. Bosshard, U. Badstübner, J. W. Kolar, and I. Stevanović, “Comparative evaluation of control methods for inductive power transfer,” in *2012 International Conference on Renewable Energy Research and Applications (ICRERA)*. IEEE, 2012, pp. 1–6.

[6] Z. Yan, Y. Zhang, T. Kan, F. Lu, K. Zhang, B. Song, and C. C. Mi, “Frequency optimization of a loosely coupled underwater wireless power transfer system considering eddy current loss,” *IEEE Transactions on Industrial Electronics*, vol. 66, no. 5, pp. 3468–3476, 2019.

[7] G. Guidi and J. A. Suul, “Minimization of converter ratings for mw-scale inductive charger operated under widely variable coupling conditions,” in *2015 IEEE PELS Workshop on Emerging Technologies: Wireless Power (2015 WoW)*. IEEE, 2015, pp. 1–7.

[8] G. Guidi, J. A. Suul, F. Jenset, and I. Sorfonn, “Wireless charging for ships: high-power inductive charging for battery electric and plug-in hybrid vessels,” *IEEE Electr. Mag.*, vol. 5, no. 3, pp. 22–32, 2017.

[9] G. Guidi, “An apparatus and a method for wireless transmission of power between dc voltage sources,” Norwegian Patent, Jan. 2015.

[10] G. Guidi and J. A. Suul, “Minimizing converter requirements of inductive power transfer systems with constant voltage load and variable coupling conditions,” *IEEE Transactions on Industrial Electronics*, vol. 63, no. 11, pp. 6835–6844, Nov 2016.

[11] S. R. Sanders, J. M. Noworolski, X. Z. Liu, and G. C. Verghese, “”Generalized averaging method for power conversion circuits”,” *IEEE Trans. on Power Electron.*, vol. 6, no. 2, pp. 251–259, April 1991.

[12] Z. U. Zahid, Z. M. Dalala, C. Zheng, R. Chen, W. E. Faraci, J. J. Lai, G. Lisi, and D. Anderson, “Modeling and control of seriesseries compensated inductive power transfer system,” *IEEE J. of Emerg. and Sel. Topics in Power Electron.*, vol. 3, no. 1, pp. 111–123, March 2015.

[13] D. Gunji, T. Imura, and H. Fujimoto, “Envelope model of load voltage on series-series compensated wireless power transfer via magnetic resonance coupling,” in *2015 IEEE PELS Workshop on Emerging Technologies: Wireless Power (2015 WoW)*, June 2015, pp. 1–6.

[14] K. Song, C. Zhu, K. Koh, D. Kobayashi, T. Imura, and Y. Hori, “Modeling and design of dynamic wireless power transfer system for ev applications,” in *IECON 2015 - 41st Annual Conference of the IEEE Industrial Electronics Society*, Nov 2015, pp. 005 229–005 234.

[15] R. Tavakoli and Z. Pantic, “Analysis, design, and demonstration of a 25-kw dynamic wireless charging system for roadway electric vehicles,” *IEEE Journal of Emerging and Selected Topics in Power Electronics*, vol. 6, no. 3, pp. 1378–1393, Sep. 2018.

[16] G. Guidi and J. A. Suul, “”Modelling techniques for designing high-performance on-road dynamic charging systems for electric vehicles”,” in *Proc. 31st Int. Electric Vehicle Symposium and Exhibition & Int Electric Vehicle Technology Conf.*, 09 2018, pp. 1–7.

Ernst Torsgård

NTNU
Norwegian University of
Science and Technology